A&A 645, A29 (2021)
https://doi.org/10.1051/0004-6361/202037652

Astronomy & Astrophysics

Search for radio jets from massive young stellar objects

Association of radio jets with H_2O and CH_3OH masers

Ü. Kavak[1,2,3,4], Á. Sánchez-Monge[1], A. López-Sepulcre[5,6], R. Cesaroni[7], F. F. S. van der Tak[3,4], L. Moscadelli[7], M. T. Beltrán[7], and P. Schilke[1]

[1] I. Physikalisches Institut, Universität zu Köln, Zülpicher Str. 77, 50937 Köln, Germany
e-mail: kavak@astro.rug.nl
[2] Institute of Graduate Studies in Science, Program of Astronomy and Space Sciences, Istanbul University, Istanbul, Turkey
[3] Kapteyn Astronomical Institute, Landleven 12, 9747AD Groningen, The Netherlands
[4] SRON Netherlands Institute for Space Research, Landleven 12, 9747AD Groningen, The Netherlands
[5] Université Grenoble Alpes, CNRS, IPAG, 38000 Grenoble, France
[6] Institut de Radioastronomie Milimétrique (IRAM), 300 rue de la Piscine, 38406 Saint-Martin-d'Hères, France
[7] INAF, Osservatorio Astrofisico di Arcetri, Largo Enrico Fermi 5, 50125 Florence, Italy

Received 4 February 2020 / Accepted 27 November 2020

ABSTRACT

Context. Recent theoretical and observational studies debate the similarities of the formation process of high- (>8 $M_\odot$) and low-mass stars. The formation of low-mass stars is directly associated with the presence of disks and jets. Theoretical models predict that stars with masses up to 140 $M_\odot$ can be formed through disk-mediated accretion in disk-jet systems. According to this scenario, radio jets are expected to be common in high-mass star-forming regions.
Aims. We aim to increase the number of known radio jets in high-mass star-forming regions by searching for radio-jet candidates at radio continuum wavelengths.
Methods. We used the *Karl G. Jansky* Very Large Array (VLA) to observe 18 high-mass star-forming regions in the *C* band (6 cm, ≈1.″0 resolution) and *K* band (1.3 cm, ≈0.″3 resolution). We searched for radio-jet candidates by studying the association of radio continuum sources with shock activity signs (e.g., molecular outflows, extended green objects, and maser emission). Our VLA observations also targeted the 22 GHz H_2O and 6.7 GHz CH_3OH maser lines.
Results. We have identified 146 radio continuum sources, 40 of which are located within the field of view of both images (*C* and *K* band maps). We derived the spectral index, which is consistent with thermal emission (between −0.1 and +2.0) for 73% of these sources. Based on the association with shock-activity signs, we identified 28 radio-jet candidates. Out of these, we identified 7 as the most probable radio jets. The radio luminosity of the radio-jet candidates is correlated with the bolometric luminosity and the outflow momentum rate. About 7–36% of the radio-jet candidates are associated with nonthermal emission. The radio-jet candidates associated with 6.7 GHz CH_3OH maser emission are preferentially thermal winds and jets, while a considerable fraction of radio-jet candidates associated with H_2O masers show nonthermal emission that is likely due to strong shocks.
Conclusions. About 60% of the radio continuum sources detected within the field of view of our VLA images are potential radio jets. The remaining sources could be compact H II regions in their early stages of development, or radio jets for which we currently lack further evidence of shock activity. Our sample of 18 regions is divided into 8 less evolved infrared-dark regions and 10 more evolved infrared-bright regions. We found that ≈71% of the identified radio-jet candidates are located in the more evolved regions. Similarly, 25% of the less evolved regions harbor one of the most probable radio jets, while up to 50% of the more evolved regions contain one of these radio-jet candidates. This suggests that the detection of radio jets in high-mass star-forming regions is more likely in slightly more evolved regions.

Key words. stars: formation – stars: massive – ISM: jets and outflows – radio continuum: ISM – HII regions

1. Introduction

High-mass stars (O- and B-type stars with masses ≥8 $M_\odot$) play a crucial role in the chemical and physical composition of their host galaxies throughout their lifetimes by injecting energy and material on different scales through energetic outflows, intense UV radiation, powerful stellar winds, and supernova explosions. Despite its importance, the formation process of massive stars is still only poorly understood because it is observationally and theoretically challenging (e.g., massive stars form in crowded environments and are located at far distances, see reviews by Tan et al. 2014; Motte et al. 2018). On the other hand, the formation of low-mass stars is better understood and is explained with a model based on accretion through a circumstellar disk and a collimated jet or outflow that removes angular momentum and enables accretion to proceed (e.g., Larson 1969; Andre et al. 2000). Circumstellar disks have indeed been observed around low-mass protostars (e.g., Williams & Cieza 2011; Luhman 2012), while ejection of material has mainly been observed as large-scale collimated jets and outflows (e.g., Bachiller 1996; Bally 2016). For high-mass stars, the role that (accretion) disks and jets/outflows play in their formation remains to be understood, also how their properties vary with the mass of the forming star and the environment. For observations, some studies have concentrated on disks and jets/outflows in selected high-mass star-forming regions (see e.g., Beuther et al. 2002a; Arce et al. 2007;

López-Sepulcre et al. 2009; Bally 2016). The advent of facilities such as the Atacama Large Millimeter/Submillimeter Array (ALMA) or the upgraded *Karl G. Jansky* Very Large Array (VLA) provides the required high spatial resolution and sensitivity to fully resolve the structure of disks and jets/outflows in high-mass star-forming regions. While disks are bright at millimeter wavelengths and constitute perfect targets for ALMA observations (e.g., Sánchez-Monge et al. 2013a, 2014; Beltrán et al. 2014; Johnston et al. 2015; Cesaroni et al. 2017; Maud et al. 2019), jets are found to be bright at the centimeter wavelengths that are observable with the VLA (e.g., Carrasco-González et al. 2010, 2015; Moscadelli et al. 2013, 2016).

Surveys of low-mass star-forming regions with the VLA (e.g., Anglada 1996; Anglada et al. 1998; Beltrán et al. 2001) revealed radio-continuum sources elongated in the direction of the large-scale molecular outflows. These sources are called thermal radio jets because their emission is interpreted as thermal (free–free) emission of ionized, collimated jets at the base of larger-scale optical jets and molecular outflows (e.g., Curiel et al. 1987, 1989; Rodriguez 1995). Because of the high spatial resolution that can be achieved at radio wavelengths with interferometers such as the VLA, thermal radio jets constitute strong evidence of collimated outflows on small scales (∼100 au; Torrelles et al. 1985; Anglada 1996) and permit defining the location of the star that is forming and powering the jet/outflow seen on larger scales. Although the emission of jets at radio wavelengths is mainly thermal, some jets show a contribution from a nonthermal component (e.g., Reid et al. 1995; Carrasco-González et al. 2010; Moscadelli et al. 2013, 2016).

Following the strategy used in the study of low-mass star-forming regions, we aim to search for radio jets associated with high-mass star-forming regions in a large sample of sources. Until recently, only a limited number of regions harboring high-mass stellar objects were known to be associated with radio jets (e.g., HH80/81: Marti et al. 1993; Carrasco-González et al. 2010, CepAHW2: Rodriguez et al. 1994, IRAS 16547−4247: Rodríguez et al. 2008, IRAS 16562−1732: Guzmán et al. 2010, G35.20−0.74 N: Beltrán et al. 2016). In the past years, progress has been made to increase the number of known jets associated with high-mass young stellar objects (e.g., Moscadelli et al. 2016; Rosero et al. 2016; Sanna et al. 2018; Purser et al. 2018). We used the VLA in two different frequency bands to search for radio jets in a sample of 18 high-mass star-forming regions associated with molecular outflow emission.

This paper is structured as follows. In Sect. 2 we present the sample and the details of the observations. The results of the observations of the radio continuum (and maser) emission are presented in Sect. 3. The analysis of the properties of the discovered sources is presented in Sect. 4, while Appendix A describes the properties of each region in more detail. In Sect. 5 we discuss the implications of our results in the context of high-mass star formation, and in Sect. 6 we summarize the most important conclusions.

2. Observations

2.1. Selected sample

We selected 18 high-mass star-forming regions from the samples of López-Sepulcre et al. (2010, 2011) and Sánchez-Monge et al. (2013b) using the following criteria: (i) clump mass >100 $M_\odot$, to exclude regions that mainly form low-mass stars, (ii) distance <4 kpc, to resolve spatial scales <4000 AU when observed with interferometers at a resolution of 1″, (iii) declination >−15°, to be observable from northern telescopes, (iv) association with an HCO^+ bipolar outflow and SiO emission with line widths broader than >20 km s^{-1} (López-Sepulcre et al. 2011; Sánchez-Monge et al. 2013b), and (v) absence of bright centimeter continuum emission, to exclude developed H II regions.

We used the NVSS[1] (Condon et al. 1998), the MAGPIS[2] (Helfand et al. 2006), CORNISH[3] (Hoare et al. 2012; Purcell et al. 2013), and RMS[4] (Urquhart et al. 2008; Lumsden et al. 2013) surveys to eliminate star-forming regions with developed H II regions that would hinder the detection of faint radio jets. Our final sample of 18 high-mass star-forming regions is listed in Table 1.

2.2. VLA observations

We used the VLA of the NRAO[5] to observe the 18 selected regions (see Table 1). The observations were conducted between June and August 2012 (project number 12A-099), when the array was in transition to its current upgraded phase and was known as expanded VLA (EVLA). During the observations, the array was in its B configuration, which provides a maximum baseline of 11 km. We observed the frequency bands *C* (4–8 GHz) and *K* (18–26.5 GHz) with 16 spectral windows of 128 MHz each, covering a total bandwidth of 2048 MHz in each band. Each spectral window has 128 channels, with a channel width of 1 MHz. The time spent per source is ∼20 min and ∼30 min at 6 cm (*C* band) and 1.3 cm (*K* band), respectively. Flux calibration was achieved by observing the quasars 3C286 ($F_{1.3\ \mathrm{cm}}$ = 2.59 mJy, $F_{6\ \mathrm{cm}}$ = 7.47 mJy) and 3C48 ($F_{1.3\ \mathrm{cm}}$ = 1.13 mJy, $F_{6\ \mathrm{cm}}$ = 5.48 mJy). The amplitude and phase were calibrated by monitoring the quasars J0555+3948, J0559+2353, J1832−1035, and J1851+0035. We used the standard guidelines for the calibration of VLA data. The data were processed using the Common Astronomy Software Applications (CASA; McMullin et al. 2007).

Continuum images of each source were obtained after channels with line emission were excluded, corresponding to H_2O and CH_3OH maser lines. The images were obtained using the "clean" task with the Briggs weighting parameter set to 2, which results in a typical synthesized beam of 1.″5 and 0.″4 for the *C* and *K* bands, respectively, and typical rms noise levels of ∼22 μJy beam^{-1} at 6 cm and ∼30 μJy beam^{-1} at 1.3 cm (see Table 1).

The spectral resolution of the observations is limited (about 50 and 13 km s^{-1} for the *C* and *K* bands, respectively) and insufficient to resolve spectral features. Despite this limitation, we produced image cubes of spectral windows that cover the frequencies of the H_2O maser line at 22 235.0798 MHz and the CH_3OH maser line at 6668.519 MHz. This allowed us to search for maser features that can be associated with the continuum emission. The rms noise levels of these cubes are 0.5 mJy beam^{-1} and 0.3 mJy beam^{-1} per channel of 13 and 50 km s^{-1} for the H_2O and CH_3OH images, respectively.

[1] NRAO VLA Sky Survey.
[2] The Multi-Array Galactic Plane Imaging Survey.
[3] Co-Ordinated Radio "N" Infrared Survey for High-mass star formation.
[4] Red MSX Source survey.
[5] The Very Large Array (VLA) is operated by the National Radio Astronomy Observatory (NRAO), a facility of the National Science Foundation operated under cooperative agreement by Associated Universities, Inc.

Table 1. High-mass star-forming regions observed with the VLA.

Region	RA (J2000) (h:m:s)	Dec (J2000) (°:′:″)	$d^{(a)}$ (kpc)	$M^{(a)}$ ($M_\odot$)	C band$^{(b)}$ $\theta_{\rm beam}$, PA	C band rms	K band$^{(b)}$ $\theta_{\rm beam}$, PA	K band rms
IRAS 05358+3543 †	05:39:12.2	+35:45:52.0	1.8	127	1.27 × 1.23, +61	8.1	… $^{(c)}$	…
G189.78+0.34 †	06:08:34.5	+20:38:51.0	1.8	150	1.28 × 1.09, +23	16.0	… $^{(c)}$	…
G192.58−0.04 †	06:12:52.9	+18:00:34.9	2.6	500	1.40 × 1.19, +21	23.6	… $^{(c)}$	…
G192.60−0.05 †	06:12:54.0	+17:59:23.0	2.6	460	1.36 × 1.14, +20	26.5	… $^{(c)}$	…
G18.18−0.30 †	18:25:07.3	−13:14:22.9	2.6	110	1.74 × 1.05, −16	10.0	0.54 × 0.31, +25	16.7
IRAS 18223−1243 †	18:25:10.9	−12:42:27.0	3.7	980	1.89 × 1.14, −14	24.5	0.58 × 0.34, +37	15.0
IRAS 18228−1312 †	18:25:42.3	−13:10:18.0	3.0	740	1.88 × 1.16, −14	35.0	0.73 × 0.67, −07	59.1
G19.27+0.1M2 ‡	18:25:52.6	−12:04:47.9	2.4	114	2.08 × 1.14, −14	9.8	0.50 × 0.32, −26	20.7
G19.27+0.1M1 ‡	18:25:58.5	−12:03:58.9	2.4	113	1.95 × 1.19, −16	9.6	0.79 × 0.42, +49	20.0
IRAS 18236−1205 †	18:26:25.4	−12:03:50.9	2.7	780	1.99 × 1.11, −18	10.2	0.51 × 0.32, −26	16.9
G23.60+0.0M1 ‡	18:34:11.6	−08:19:05.9	2.5	365	1.85 × 1.13, −22	8.7	0.54 × 0.30, +32	36.1
IRAS 18316−0602 †	18:34:20.5	−05:59:30.0	3.1	1000	1.71 × 1.09, −21	8.4	0.53 × 0.30, +35	40.0
G24.08+0.0M2 ‡	18:34:51.1	−07:45:32.0	2.5	201	1.80 × 1.13, −21	17.0	0.53 × 0.30, +32	37.0
G24.33+0.1M1 ‡	18:35:07.8	−07:35:04.0	3.8	1759	1.69 × 1.25, −13	21.0	0.49 × 0.31, −31	26.1
G24.60+0.1M2 ‡	18:35:35.7	−07:18:08.9	3.7	483	1.66 × 1.03, −20	18.2	0.79 × 0.41, +51	21.8
G24.60+0.1M1 ‡	18:35:40.2	−07:18:37.0	3.7	192	1.67 × 1.22, −10	12.7	0.75 × 0.38, +57	22.5
G34.43+0.2M3 ‡	18:53:20.3	+01:28:23.0	2.5	301	1.57 × 1.46, −59	17.9	0.53 × 0.29, +40	19.0
IRAS 19095+0930 †	19:11:54.0	+09:35:52.0	3.0	500	1.61 × 1.37, −83	17.0	0.53 × 0.29, +44	63.4

Notes. $^{(a)}$Distances (d) and clump masses (M) from López-Sepulcre et al. (2011) and Sánchez-Monge et al. (2013b). $^{(b)}$Synthesized beam ($\theta_{\rm beam}$) major and minor axis in arcsecond, and position angle (PA) in degrees. The rms noise level is given in units of μJy beam^{-1}. Regions marked with † and ‡ in the first column indicate IR-loud and IR-dark sources, respectively, based on the classification of López-Sepulcre et al. (2010). $^{(c)}$Region not observed in the K band.

3. Results

3.1. Continuum emission

We detected compact continuum emissions in all 18 observed high-mass star-forming regions. A total of 146 compact sources are identified with intensities above 3σ level, where σ is the rms noise level of each map (see Table 1). In Table B.1 we list the coordinates, fluxes, and source sizes.

Most of the sources (a total of 131) are only detected in the C-band image, while 4 of them are only detected in the K band (see Fig. 1). Only 11 sources are detected at both frequencies. The higher detection rate of sources in the C band is due to several factors. First, four regions were only observed in the C band (see Table 1). This results in 26 radio continuum sources for which we have no access to K-band images. Second, the field of view of the C-band images (primary beam ≈9′) is larger than that of the K-band primary beam (≈2′). Only 40 sources are located within the K-band primary beam (identified as iC/iK, see Fig. 1). This number is reduced to only 24 when we consider only the sources that have been observed in both frequency bands. A total of 68 sources are inside the C-band primary beam (identified as iC) but outside the K band primary beam (identified as oK, see Fig. 1). The remaining 38 sources are outside the primary beam of the C-band observations (marked oC; see also Table B.1). The sources that are outside the primary beam are bright enough to be detected even when the telescope sensitivity is highly reduced. Third, the spatial filtering of the interferometer is different at the two frequencies. In the B configuration, the VLA recovers scales up to 11″ in the C band, and only up to 4″ in the K band (see also Appendix A of Palau et al. 2010). Finally, we cannot exclude the possibility that some of these sources are extragalactic objects that can only be detected at low frequencies. We have followed the approach of Anglada et al. (1998) to determine the possible contamination of background sources in our catalog. The expected number of background sources $N_{\rm bg}$ is given by

$$N_{\rm bg} = 1.4\left\{1-\exp\left[-0.0066\left(\frac{\theta_F}{\rm arcmin}\right)^2\left(\frac{\nu}{5\ {\rm GHz}}\right)^2\right]\right\} \times \left(\frac{S_0}{\rm mJy}\right)^{-0.75}\left(\frac{\nu}{5\ {\rm GHz}}\right)^{-2.52}, \quad (1)$$

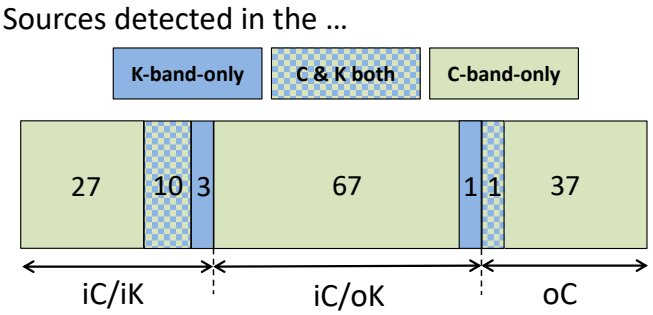

Fig. 1. Number of radio continuum sources detected in the K-band images (marked in blue and corresponding to 15 sources) and in the C-band images (marked in green and corresponding to 142 sources). Only 4 of the 146 detections are detected in the K-band images alone. The vast majority (131) are detected only in the C-band images (see Sect. 3.1 for more details). The bottom labels mark the sources that are located within the primary beams of the K-band and C-band images. Thirty-eight sources are located outside the C-band primary beam (oC), 68 sources are located inside the C-band primary beam but outside the K-band primary beam (iC/oK), and 40 sources are located within the primary beam of both images (iC/iK). See Sects. 3.1 and 3.2 for more details.

where θ_F is the area of the sky that has been observed (18 fields in C band, and 14 fields in K band), ν is the frequency of the observations, and S_0 is the detectable flux density threshold ($3\times$rms, with an average rms of 22 μJy beam^{-1} in the C band, and 30 μJy beam^{-1} in the K band). This results in $N_{\rm bg} = 11$ and $N_{\rm bg} = 0.2$ for the C- and K-band images, respectively. Less than 5% of the sources detected in the C band might be background objects not related to the star-forming regions, while we do not expect contamination in the K-band images.

3.2. Spectral index analysis

The spectral index (α) is defined as $S_\nu \propto \nu^\alpha$, where S_ν is the flux density and ν is the frequency. We calculated the spectral index for the continuum sources using the measured flux densities at 1.3 cm (K band) and 6 cm (C band). For the sources without detection in one of the bands, we assumed an upper limit of the flux density equal to 5σ. The flux densities of the sources were corrected for the primary beam response of the antennas. The sources far away from the phase centers (listed in Table 1) have larger uncertainties in the correction factors of the primary beam and therefore in the final (corrected) flux. The sources located within the primary beams in both frequency bands (i.e., sources listed as "iC/iK" in Table B.1) accordingly have more accurate flux estimates. For the sources outside one of the primary beams (i.e., oK or oC), we did not determine the spectral index because of the high uncertainty involved in the fluxes. In the last column of Table B.1 we list the calculated spectral indices. For the sources detected at both frequencies, we improved the determination of the spectral index by creating new images with the same uv (visibility) coverage (see Table B.3). This ensured that the interferometer is sensitive to similar spatial scales at both frequencies.

In Fig. 2 we present the spectral index against the ratio of flux density to intensity peak for the 24 continuum sources that were observed at both bands and located within the primary beams. For the sources detected at 6 cm only, we derive an upper limit to the spectral index, while we derive a lower limit for the spectral index for the sources detected only at 1.3 cm. We note that the real spectral index may not always be an upper limit if the source emission is completely filtered out in our K-band images. Further observations at different wavelengths, with a similar uv sampling and angular resolution are necessary to constrain the spectral index of the sources detected only in the C-band images. The sources detected at both wavelengths (black dots) have a more precise determination of the spectral index. For most sources, we derive spectral indices consistent with thermal emission (i.e., in the range of -0.1 to $+2$), and in agreement with observations of other radio-jets (e.g., Anglada et al. 2018). Only a few sources show very negative spectral indices (sources 48, 96, and 144). These sources are likely to be partially filtered out in the K-band images, which may result in lower limits for the actual value of the spectral index. In particular, source 48 appears as three distinguishable peaks, which we refer to as a, b, and c, surrounded by a more diffuse and extended structure that is mainly visible in the C-band image. High flux-to-intensity ratios indicate that the source is likely extended and most likely partially filtered out in the K-band images, which may result in negative spectral indices.

3.3. Maser emission

H_2O and CH_3OH masers are excellent indicators of star formation activity (e.g., Beuther et al. 2002b; Moscadelli et al. 2005; de Villiers et al. 2015). We created image cubes of the H_2O and CH_3OH spectral lines and searched for maser features by scanning the entire velocity range. Despite the limited spectral resolution of our observation setup (see Sect. 2), we found maser emission in 14 of the 18 regions. In Table 2 we list the coordinates of the maser features detected in each region together with the velocity at which the feature is detected and its intensity. We also compare the velocities of the maser features with the systemic velocities determined from $H^{13}CO^+$ (1–0) observations (López-Sepulcre et al. 2011). We find that the velocities of H_2O masers match the $H^{13}CO^+$ (1–0) velocities, while the CH_3OH masers have a larger discrepancy, probably due to the lower spectral resolution.

The low spectral resolution in our observations compared to the typical maser line widths (a few km s^{-1}; Elitzur 1982; Kalenskii & Kurtz 2016) leads to smearing of the maser intensities. The intensities given in Table 2 should be considered as lower limits. Despite this limitation, the high angular resolution of our observations can be used to spatially associate the H_2O and CH_3OH masers with the detected continuum sources. When the angular separation between the continuum source and the maser is smaller than the synthesized beam size (listed in Table 1), we assume that the maser is associated with the continuum source. In the last column of Table 2 we specify the identifier of the continuum source (see Table B.1) with which the maser is associated. We find 10 continuum sources associated with maser features (see Sect. 4.4 for more details).

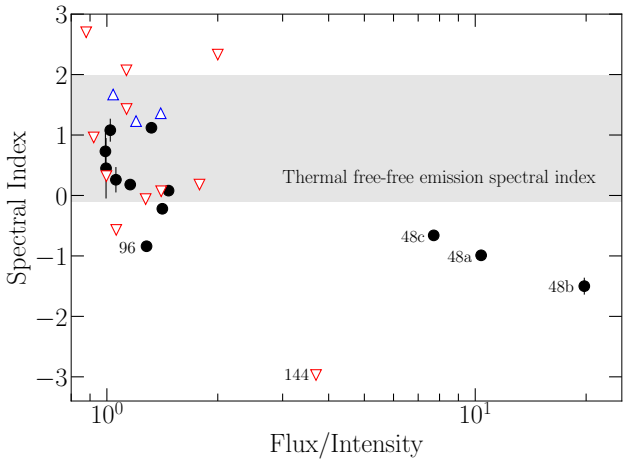

Fig. 2. Spectral index (α, see Sect. 3.2) against the flux-to-intensity ratio for the radio continuum sources detected in both frequency bands and inside the primary beam of both images (sources listed as "iC/iK" in Table B.1). The gray shaded region depicts the spectral index regime associated with thermal free–free emission (i.e., in the range from -0.1 to $+2$). Black dots correspond to sources detected in both bands (see spectral indices in Table 3), blue upward-pointing triangles correspond to sources detected only in the K band (i.e., lower limits), and red downward-pointing triangles correspond to sources detected only in the C band (i.e., upper limits).

4. Analysis and discussion

In this section, we determine how many sources in our sample are potential radio-jets. For this purpose, we study the nature of the detected radio continuum emission, and investigate the association with molecular outflows, masers, and EGOs[6]/IRAC

[6] The so-called extended green objects (EGOs) are sources with bright emission in the *Spitzer* maps.

Table 2. H_2O and CH_3OH maser features.

Region	Maser	RA (J2000) (h:m:s)	Dec (J2000) (°:′:″)	V_{maser} [(a)] (km s^{-1})	$V_{LSR}^{H^{13}CO^+}$ (km s^{-1})	Intensity (Jy beam^{-1})	Continuum source ID [(b)]
IRAS 05358+3543	CH_3OH	05:39:13.071	+35:45:50.938	−304	−15.8	0.028	2
G189.78+0.34	CH_3OH	06:08:35.304	+20:39:06.405	−13	+9.2	0.014	14
G192.58−0.04	CH_3OH	06:12:54.026	+17:59:23.060	−14	+9.1	0.72	22
G18.18−0.30	H_2O	18:25:07.575	−13:14:31.487	−3	+50.0	0.57	–
IRAS 18223−1243	H_2O	18:25:10.804	−12:42:26.234	+24	+45.2	0.006	–
IRAS 18228−1312	H_2O	18:25:41.935	−13:10:19.591	+24	+33.1	0.022	48
IRAS 18236−1205	H_2O	18:26:25.677	−12:03:48.402	+28	+26.5	0.010	63
	H_2O	18:26:25.575	−12:03:48.502	+28	+26.5	0.006	63
	H_2O	18:26:25.782	−12:03:53.263	+15	+26.5	0.010	64
	H_2O	18:26:27.149	−12:03:54.888	+15	+26.5	0.014	–
	CH_3OH	18:26:25.788	−12:03:53.456	+5	+26.5	0.26	64
G19.27+0.1M1	H_2O	18:25:58.546	−12:03:58.516	+28	+26.5	0.022	–
G23.60+0.0M1	H_2O	18:34:11.237	−08:19:07.680	+108	+106.5	0.44	–
	H_2O	18:34:11.452	−08:19:07.138	+108	+106.5	0.10	–
IRAS 18316−0602	H_2O	18:34:20.918	−05:59:41.638	+41	+42.5	11.1	83
	CH_3OH	18:34:20.913	−05:59:42.087	−233	+42.5	0.014	83
G24.33+0.1M1	H_2O	18:35:08.123	−07:35:04.216	+108	+113.6	4.03	110
	CH_3OH	18:35:08.147	−07:35:04.260	−182	+113.6	0.010	110
G24.60+0.1M2	H_2O	18:35:35.728	−07:18:08.796	+122	+115.3	0.031	–
G24.60+0.1M2	H_2O	18:35:40.120	−07:18:37.417	+54	+53.2	1.02	136
IRAS 19095+0930	H_2O	19:11:53.975	+09:35:50.559	+37	+43.9	26.8	143
	H_2O	19:11:53.990	+09:35:49.848	+37	+43.9	10.3	143
	CH_3OH	19:11:53.993	+09:35:50.641	+39	+43.9	0.043	143

Notes. [(a)]Uncertainties in the reported maser velocities (V_{maser}) are expected to be ∼50 km s^{-1} for the CH_3OH masers and ∼13 km s^{-1} for the H_2O masers (see Sect. 2). The systemic velocities ($V_{LSR}^{H^{13}CO^+}$) are reported in López-Sepulcre et al. (2011). [(b)]Radio continuum source spatially associated with the maser feature and listed as identified in Table B.1.

4.5 μm band and are usually found to be associated with strong shocks and jets (e.g., Cyganowski et al. 2008, 2009). Based on these criteria, we identify the best radio-jet candidates in our sample and characterize their properties.

4.1. Nature of the radio continuum emission

Usually, two mechanisms are invoked to explain the origin of thermal free-free radiation from ionized gas in star-forming regions: photoionization, and ionization through shocks (e.g., Gordon & Sorochenko 2002; Kurtz 2005; Sánchez-Monge et al. 2008, 2013c; Anglada et al. 2018). In the case of photoionization, ultraviolet (UV) photons with energies above 13.6 eV are emitted by massive stars and ionize the surrounding atomic hydrogen. In the second scenario, the ionization is produced when ejected material associated with outflows and jets interacts in a shock with neutral and dense material surrounding the forming star (e.g., Curiel et al. 1987, 1989; Anglada et al. 1992).

Anglada (1995, 1996) showed that the relation between the radio luminosity and the bolometric luminosity of young stellar objects (YSOs) depends on the origin of the ionization: stellar UV radiation, or shocks (see also Anglada et al. 2018). We used this relation to investigate the nature of our continuum sources. The solid line in Fig. 3 shows the maximum radio luminosity that a high-mass object of a given luminosity may have according to its UV radiation, the so-called Lyman continuum limit that is usually associated with H II regions. The radio luminosity decreases fast with decreasing bolometric luminosity. In contrast, the radio luminosity originated in shocks (i.e., radio jets) has a flatter curve. The dotted line in Fig. 3 shows the least-squares fit to the sample of radio jets studied in Anglada et al. (2018) that are shown as gray squares in the figure.

We calculated the radio luminosity of our continuum sources as $L_{radio} = S_\nu d^2$, where S_ν is the observed flux density in the C band (listed in Table B.1) and d is the distance to the source (listed in Table 1). The bolometric luminosity (L_{bol}) of each source is uncertain because we lack high-resolution data at far-infrared wavelengths. The bolometric luminosity of each region is given in Table A.1 of López-Sepulcre et al. (2011) and provides an upper limit to the actual luminosity. As a simple approach, we divided the bolometric luminosity by the number of radio sources detected within the primary beam to have an estimate of the expected average luminosity for the continuum sources in the region. Circle symbols in Fig. 3 show the continuum sources detected in our work and located inside the K-band primary beam (i.e., with reliable flux measurements and listed as iC/iK in Table B.1). Colored symbols correspond to those sources for which we could derive the spectral index (see Fig. 2), with blue symbols corresponding to positive spectral indices (i.e., $\alpha > +0.0$, mainly thermal emission) and red symbols corresponding to negative spectral indices. In general, our sources lie in between the two lines defining the radio jet and H II region regimes[7]. Interestingly, sources with positive spectral indices (blue symbols) seem to preferentially follow, although with some

[7] Some sources lie above the solid curve depicting the Lyman continuum limit. This is in agreement with other studies that report the existence of a population of H II regions with radio fluxes higher than the Lyman continuum limit (see, e.g., Sánchez-Monge et al. 2013d; Cesaroni et al. 2016).

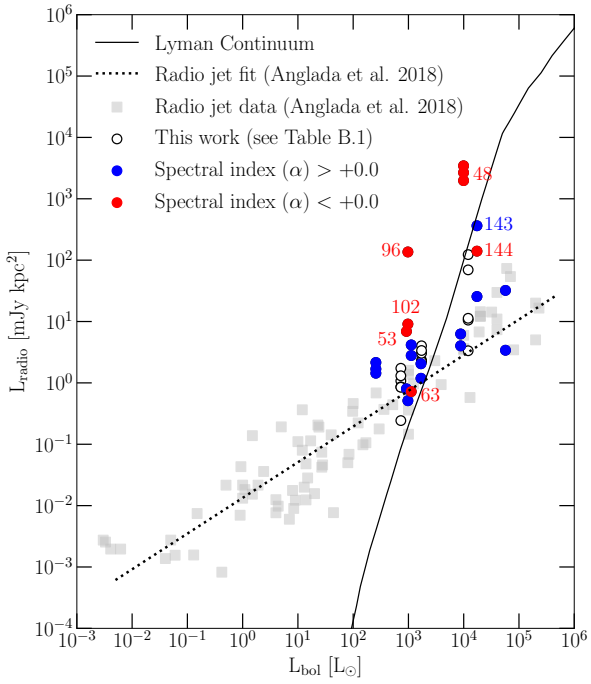

Fig. 3. Scatter plot of bolometric luminosity (L_{bol}) and observed radio continuum luminosity (L_{radio}) at 6 cm (C band). Open black circles correspond to the continuum sources detected in our work that are located within the primary beam of the K-band (1.3 cm) images (i.e., "iC/iK" in Table B.1). Blue and red symbols mark the sources with positive and negative spectral indices, respectively, as listed in Table B.1 and shown in Fig. 2. The solid line represents the values expected from Lyman continuum radiation for a zero-age main-sequence star of a given luminosity (Thompson 1984). The dashed line is the least-squares fit to the radio jets reported by Anglada et al. (2018, shown as gray squares), corresponding to $[L_{radio}/\mathrm{mJy\ kpc^2}] = 10^{-1.90}\ [L_{bol}/L_\odot]^{+0.59}$ (see their Eq. (28)).

dispersion, the relation found for radio jets, while sources with negative spectral indices (red symbols) are located closer to the Lyman continuum regime. This favors our previous interpretation that sources with negative spectral indices may be slightly extended H II regions that are partially filtered out in the K-band images.

4.2. Association with molecular outflows

We investigated the association of radio continuum sources with molecular outflows by comparing the location of radio sources with respect to the molecular outflow emission reported mainly by López-Sepulcre et al. (2010) and Sánchez-Monge et al. (2013b). It is expected that the most promising radio-jet candidates is in the center of the molecular outflow emission.

We find a total of 24 radio continuum sources that are spatially associated with molecular outflow emission (see Table 3 and Fig. 4 for more details). Out of these sources, 18 (sources 2, 4, 13, 14, 15, 16, 22, 23, 25, 48a, 48b, 48c, 74, 83, 95, 110, 137 and 143) are located at or near the geometric center of the molecular outflow emission, while the remaining 6 (sources 12, 63, 64, 65, 73, and 144) are located within the outflow lobes. Although we cannot confirm that these 6 sources are at the base of the outflows detected with single-dish telescopes (with angular resolutions of 11–29″), we cannot exclude that they might drive molecular outflows. Further observations of outflow tracers at higher angular resolution are necessary to confirm and better associated the molecular outflows with the radio continuum sources. In Table 3 we list the outflow momentum rates reported in the literature (see López-Sepulcre et al. 2010; Sánchez-Monge et al. 2013b). For sources 137, no outflow momentum rate has been reported (Hatchell et al. 2001; Liu et al. 2013).

4.3. Association with EGOs

In this section, we investigate the association of radio continuum sources with *Spitzer*/IRAC 4.5 μm emission tracing EGOs, which are considered related to the shocked gas. For the association with EGOs we used the catalogs of Cyganowski et al. (2008, 2009). In total, we found six sources (sources 42, 63, 64, 119, 137 and 139) with an EGO counterpart (see Table 3).

We also inspected the *Spitzer*/IRAC images of the different regions to search for other possible EGOs not included in previous catalogues. We identified nine radio continuum sources in this category (see sources 48, 65, 73, 74, 83, 110, and 143, marked with a questionmark in Table 3). The association of these sources with bright 4.5 μm emission suggests their association with strong shocks and favors the hypothesis of a radio-jet origin for the radio continuum emission of these objects. However, a more detailed characterization of the infrared properties of the nine additional sources is necessary to confirm whether these objects are EGOs.

4.4. Association with masers

Our VLA observations (see Sect. 2.2) allow us to search for H_2O and CH_3OH maser spots associated with radio continuum sources. As shown in Table 2, we have found 16 H_2O and 7 CH_3OH maser spots.

We find ten radio continuum sources associated with maser features, of which three (sources 2, 14, and 22) are associated with CH_3OH masers only, three sources (sources 48, 63, and 136) are associated only with H_2O masers, and four sources (sources 64, 83, 110, and 143) are associated with both types of masers (see Table 3 and Fig. 4). It is worth noting that the three sources associated only with CH_3OH masers correspond to regions observed only in the C band. Future observations of these sources in the K band together with observations of the H_2O maser line could confirm that all sources associated with CH_3OH maser are also associated with H_2O maser features.

The observed Class II 6.7 GHz CH_3OH masers are ideal indicators for embedded YSOs and mark the location of deeply embedded massive protostars (e.g., Breen et al. 2013). On the other hand, 22 GHz H_2O masers have been found associated with outflow activity (e.g., Torrelles et al. 2011) as well as tracing disk-like structures around young stellar objects (e.g., Moscadelli et al. 2019). Our maser observations have therefore enabled us to identify at least seven potential candidates for a radio-jet (i.e., sources associated with outflow activity).

4.5. Radio-jet candidates

Out of the 146 radio continuum sources detected in our study, we identified 28 sources (see list at the beginning of Table 3) as possible radio-jet candidates, based on their association with outflow and shock activity. We find 24 of these sources associated with molecular outflow emission, 6 of them with EGOs, and 10 with masers. In the sketch presented in Fig. 4, we summarize these findings.

In addition to these 28 sources, we also identified 8 radio-continuum sources with spectral indices consistent with thermal

Table 3. Properties of the radio-jet candidates.

ID	Flux properties [a]			Source size properties [b]			Outflow/shock activity [c]		
	$S_{\rm C\ band}$	$S_{\rm K\ band}$	α	$\theta_{\rm C\ band}$	$\theta_{\rm K\ band}$	β	$\log(\dot{P}_{\rm out})$	EGOs	Masers
Radio-jet candidates with signposts of outflow activity									
2 [d]	0.53 ± 0.01	–	–	0.75	–	–	−3.9	n	CH_3OH
4 [d]	0.33 ± 0.01	–	–	1.23	–	–	−3.9	n	…
12 [d]	0.72 ± 0.03	–	–	0.97	–	–	−3.1 †	n	…
13 [d]	1.24 ± 0.05	–	–	0.75	–	–	−3.1	n	…
14 [d]	0.69 ± 0.05	–	–	1.08	–	–	−3.1	n	CH_3OH
15 [d]	0.94 ± 0.04	–	–	1.60	–	–	−3.1	n	…
16 [d]	1.04 ± 0.04	–	–	1.16	–	–	−3.1	n	…
22 [d]	10.27 ± 0.22	–	–	1.55	–	–	−3.3	n	CH_3OH
23 [d]	1.56 ± 0.05	–	–	…	–	–	−3.3	n	…
25 [d]	0.49 ± 0.02	–	–	…	–	–	−3.3	n	…
42	4.16 ± 0.08	…	…	0.81	…	…	…	Y	…
48a [e]	55.32 ± 3.50	15.19 ± 1.51	−0.99 ± 0.09	2.70	2.07	−0.20	−2.9	?	H_2O
48b [e]	75.41 ± 9.50	10.53 ± 1.30	−1.50 ± 0.14	3.84	1.64	−0.65	−2.9	?	…
48c [e]	129.52 ± 8.30	54.41 ± 3.51	−0.66 ± 0.07	2.28	1.89	−0.14	−2.9	?	…
63 [e]	0.99 ± 0.06	0.75 ± 0.13	−0.22 ± 0.07	1.19	1.11	−0.05	−2.6 †	Y	H_2O
64 [e]	0.28 ± 0.02	0.35 ± 0.08	+0.18 ± 0.04	<1.38	0.66	>−0.56	−2.6 †	Y	H_2O, CH_3OH
65 [e]	0.57 ± 0.14	2.31 ± 0.09	+1.08 ± 0.19	<1.46	<0.75	…	−2.6 †	?	…
73 [e]	0.24 ± 0.15	0.43 ± 0.09	+0.45 ± 0.50	0.38	<0.74	<+0.51	−2.4 †	?	…
74 [e]	0.35 ± 0.03	0.49 ± 0.13	+0.26 ± 0.21	0.53	0.42	−0.18	−2.4	?	…
83 [e]	3.35 ± 0.21	3.73 ± 0.29	+0.08 ± 0.08	0.87	0.85	−0.02	−1.8	?	H_2O, CH_3OH
95	<0.042	0.25 ± 0.07	> +1.36	…	<0.42	…	−1.8	n	…
110 [e]	0.46 ± 0.21	1.20 ± 0.06	+0.73 ± 0.35	<1.39	0.37	>−1.01	−2.9	?	H_2O, CH_3OH
119	1.11 ± 0.06	<0.022	…	2.28	…	…	…	Y	…
136	<0.10	0.85 ± 0.12	>+1.67	…	1.50	…	…	n	H_2O
137 [e]	14.40 ± 1.20	2.21 ± 0.20	…	2.53	1.60	−0.35	… ‡	Y	…
139	0.73 ± 0.03	< 0.019	…	0.87	…	…	…	Y	…
143 [e]	39.50 ± 1.60	130.87 ± 2.60	+1.12 ± 0.04	0.55	0.28	−0.52	−3.4	?	H_2O, CH_3OH
144	15.57 ± 0.89	<0.32	<−2.97	2.44	…		−3.4 †	n	…
Radio continuum sources consistent with positive spectral index, but with no signposts of outflow activity									
61	0.14 ± 0.03	<2.10	<+2.07	1.79	…	…	…	n	…
62	<0.05	0.24 ± 0.09	>+1.23	…	<0.44	…	…	n	…
86	0.35 ± 0.01	<2.32	<+1.43	<1.45	…	…	…	n	…
109	0.08 ± 0.03	<1.75	<+2.33	<0.94	…	…	…	n	…
113	0.28 ± 0.01	<0.31	<+0.07	0.85	…	…	…	n	…
126	0.11 ± 0.01	<0.37	<+0.96	<1.37	…	…	…	n	…
129	0.16 ± 0.01	<0.20	<+0.18	1.23	…	…	…	n	…
145	2.84 ± 0.02	<4.34	<+0.32	<1.48	…	…	…	n	…

Notes. [a]Primary beam corrected fluxes in mJy as listed in Table B.1. For sources 42, 119, 137 and 139 it was not possible primary beam correct the fluxes at both bands (see Sect. 3), resulting in not usable spectral indices. The spectral index α is defined in Eq. (2). [b]Source sizes in arcsec determined as $\sqrt{\theta_{\rm major} \times \theta_{\rm minor}}$, with $\theta_{\rm major}$ and $\theta_{\rm minor}$ listed in Table B.2. Upper limits corresponds to sources for which we could not determine a deconvolved source size. The source size index β is defined in Eq. (2). [c]Association of the radio continuum source with outflow and shock activity. The associations correspond to (i) molecular outflows, with the outflow momentum rate $\dot{P}_{\rm out}$ given in units of $M_\odot$ yr^{-1} km s^{-1} (from López-Sepulcre et al. 2010; Sánchez-Monge et al. 2013b), with the dagger indicating those radio continuum sources located within the outflow lobes and not at the center of the outflow, (ii) EGOs (or extended green objects), based on the catalog of Cyganowski et al. (2008, questionmarks indicate the presence of bright *Spitzer*/IRAC 4.5 μm emission although without confirmation of the object being an EGO), and (iii) H_2O and CH_3OH masers, as listed in Table 2. Source 137, marked with a double cross, is associated with molecular outflow emission (Hatchell et al. 2001; Liu et al. 2013), but no outflow momentum rate has been reported. [d]Sources not observed in the *K* band. For these sources we do not have information on the *K*-band flux and presence of H_2O masers. [e]Sources detected at both frequency bands and for which we have created new images using a common *uv*-range that allows us to sample similar spatial scales. Fluxes and source sizes for these sources are taken from Table B.3. Fluxes for source 137 can not be primary beam corrected and cannot be used to determine a spectral index.

emission (see bottom list in Table 3). Based on the results shown in Fig. 3, these sources could also be radio-jet candidates, despite their lack of association with tracers of outflow and shock activity. In the following, we build on the properties of the identified radio-jet candidates.

4.5.1. Radio continuum properties

Reynolds (1986) describe radio-jets with a model that assumes a jet of varying temperature, velocity, and ionization fraction. In case of constant temperature, the relations of the flux density

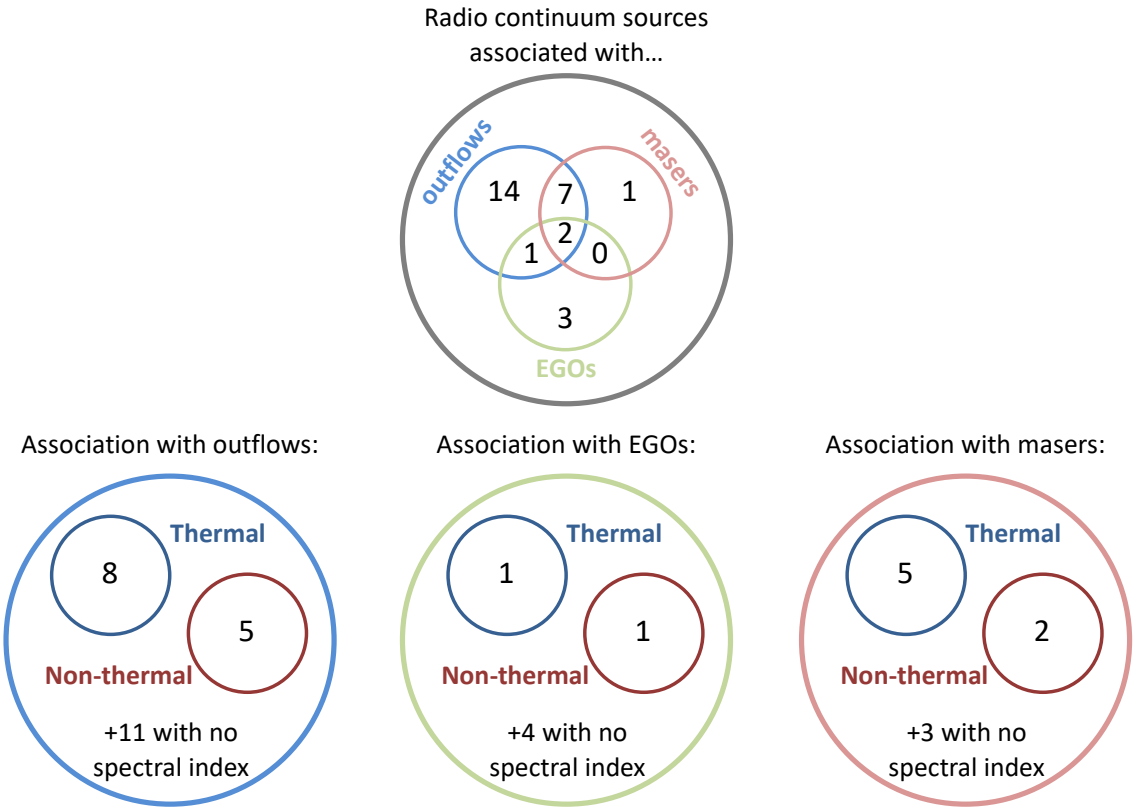

Fig. 4. Diagrams summarizing the outflow-activity associations of the radio-jet candidates studied in this work. The integer numbers indicate the number radio-jet candidates in a specific group (see Table 3). The *top diagram* summarizes the association of the radio-jet candidates with molecular outflows, masers, and EGOs (see Sect. 4, for EGOs we only consider an association if the source is labeled "Y" in Table 3). *Bottom row diagrams*: results regarding the thermal (spectral index >−0.1) and nonthermal (spectral index <−0.1) properties of the radio continuum emission. The number of sources for which we could not derive the spectral index is also indicated.

(S_ν), and source size (θ_ν) with frequency are given by

$$S_\nu \propto \nu^{\alpha} = \nu^{1.3-0.7/\epsilon} \quad \text{and} \quad \theta_\nu \propto \nu^{\beta} = \nu^{-0.7/\epsilon}, \tag{2}$$

where ϵ depends only on the geometry of the jet and is the power-law index that describes how the width of the jet varies with the distance from the central object. In this model, the spectral index α is always smaller than 1.3 and drops to values <0.6 for confined jets ($\epsilon < 1$; Anglada et al. 1998).

In Table 3 we list the spectral index (α) and the source size index (β) for our radio-jet candidates. The latter only for the sources detected at both frequencies. Nine of the radio-jet candidates associated with outflow/shock activity have spectral indices consistent with thermal emission (>−0.1), with six showing clear positive (>+0.4) spectral indices. These values are consistent with the model of Reynolds (1986) for values of $\epsilon > 0.6$. For such geometries of the jet, the source size index (β) is expected to be about −1. The source size indices reported in Table 3 are mainly in the range −0.1 to −1.0, in agreement with the model of Reynolds (1986) for radio-jets.

Although most of our radio-jet candidates have spectral indices consistent with thermal emission (64% of the sample, see Table 3), we find some sources (accounting for 36% of the sample, five sources[8]) that show negative spectral indices. This finding is in agreement with some recent works. For example, Moscadelli et al. (2016) find about 20% of their sample of 15 radio continuum sources to be associated with nonthermal emission. The presence of nonthermal emission is explained in terms of synchrotron emission from relativistic electrons accelerated in strong shocks within the jets, and a number of cases have been studied in more detail (e.g., Carrasco-González et al. 2010; Sanna et al. 2019). Further detailed observations toward these new four nonthermal radio-jet candidates, can provide further constraints to understand the characteristics of these types of objects.

We searched for possible relations between the presence of thermal and non-thermal radio-jets and different outflow/shock activity signs (i.e., outflows, masers, and EGOs). We summarize our findings in the bottom panels of Fig. 4. We do not find a preferred relation between thermal and nonthermal radio-jets with the outflow activity signs, since we find similar percentages (see Table 4) for the association with outflows (88% and 100, respectively), EGOs (13 and 20%), and masers (55 and 40%). The

Table 4. Number of the sources with thermal and nonthermal radio continuum emission associated with different outflow activity signatures.

	Nonthermal sources	Thermal sources
Outflows	5/5 (100%)	7/8 (88%)
EGOs	1/5 (20%)	1/8 (13%)
Masers (all)	2/5 (40%)	5/8 (63%)
H_2O	2/5 (40%)	5/8 (63%)
CH_3OH	0/5 (0%)	4/8 (50%)

[8] As discussed in Sect. 4.5.3, four of these five sources are most likely H II regions. This would reduce the number of nonthermal radio-jets to only one out of 14 (7% of our sample).

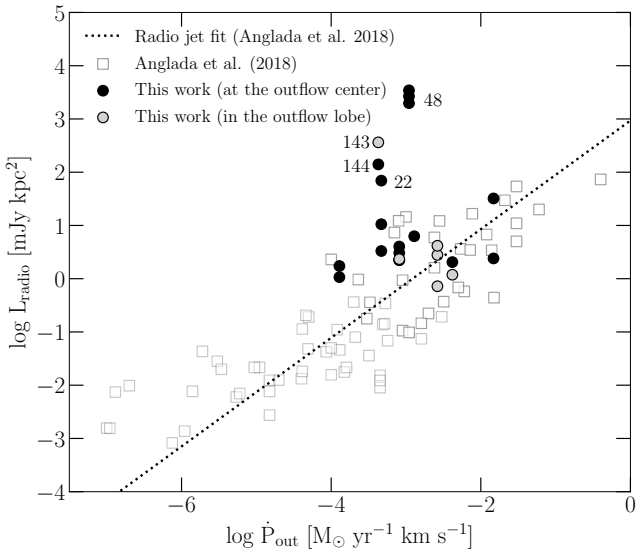

Fig. 5. Relation between radio luminosity ($L_{\rm radio}$) and outflow momentum rate ($\dot{P}_{\rm out}$). Open boxes show data from Anglada et al. (1992, 2018). The dashed line is a least-squares fit to the radio-jets reported by Anglada et al. (2018), corresponding to $[L_{\rm radio}/{\rm mJy\ kpc^2}] = 10^{+2.97}\ [\dot{P}/M_\odot\ {\rm yr^{-1}\ km\ s^{-1}}]^{+1.02}$ (see their Eq. (31)).

low number of objects included in our analysis prevents us from deriving further conclusions, and we indicate that a larger sample of radio-jets needs to be studied to better understand the properties and differences between thermal and nonthermal radio-jets. It is also worth noting that all the four objects associated with both CH_3OH and H_2O masers are thermal radio-jet candidates (see Table 3), while only one of the three objects associated with only H_2O masers shows thermal emission. This might suggest that radio-jets associated with CH_3OH masers tend to have positive spectral indices (i.e., thermal emission), while radio-jets associated with only H_2O masers might preferentially have negative spectral indices (i.e., nonthermal emission). However, the low number of sources studied in our sample prevents from deriving further conclusions. The different levels of association of the radio continuum sources with maser emission may be affected by the variability of masers (Felli et al. 2007; Sugiyama et al. 2017; Ashimbaeva et al. 2017). Moreover, we cannot discard that the poor spectral resolution of our observations, which may smear out the intensity of the maser lines making some of them undetectable with our sensitivity limits, may also affect our detectability limits. Despite these limitations, our results are in agreement with the 6.7 GHz CH_3OH masers tracing the actual location of the newly born YSOs usually associated with thermal winds/jets, while H_2O masers may be originated in strong shocks where nonthermal synchrotron emission can be relevant (see, e.g., Moscadelli et al. 2013, 2016).

4.5.2. Jet-outflow connection

It has been found that the radio luminosity ($L_{\rm rad} = S_\nu d^2$) of thermal radio-jets is correlated with the energetics of the associated molecular outflows. The relation between radio luminosity and momentum rate in the outflow ($\dot{P}_{\rm out}$) was empirically derived by Anglada et al. (1992, see also Anglada et al. 2018). In Fig. 5 we compare our radio-jet candidates (see Table 3) with the radio-jets studied by Anglada et al. (2018). As reported by Anglada et al. (2018), there is a tight correlation between the radio luminosity of the jet and the outflow momentum rate. This relation is interpreted as proof that shocks are the ionization mechanism of radio-jets (see, e.g., Rodríguez et al. 2008; Anglada et al. 2018). Most of the radio-jet candidates investigated in this work, with the exception of only a few sources, follow this relation, suggesting a radio-jet origin for the detected radio continuum emission. The exceptions are mainly sources 48a, 48b, 48c, 143, and 144, which have a much higher radio luminosity than the associated outflow momentum rate. This excess suggests that another mechanism could be responsible for a large fraction of the observed radio continuum emission. Based on the location of these sources in the diagram shown in Fig. 3, these sources may correspond to more evolved and extended H II regions instead of radio-jets, which would explain the discrepancy between the observed radio luminosity and outflow momentum rate. In this case, we could be facing two possible scenarios. The first is that the sources are indeed radio-jets that transition into a more evolved H II region phase (similar to what has been proposed for G35.20−0.74N, Beltrán et al. 2016). The second scenario is that the radio continuum sources that we are detecting are only associated with an H II region, and the spatial coincidence with the molecular outflow emission is due to the presence of another (lower mass) object that powers the outflow, but with nondetectable radio continuum emission in our maps. Higher angular resolution observations of the molecular outflow can better establish the location of the powering source and its association with the detected radio continuum sources.

Following Eq. (8) of Anglada et al. (2018, see also Reynolds 1986), we estimated the ionized mass-loss rate ($\dot{M}_{\rm ion}$) of our radio-jet candidates as

$$\left(\frac{\dot{M}_{\rm ion}}{10^{-6}\ M_\odot\ {\rm yr^{-1}}}\right) = 0.108 \left(\frac{d}{\rm kpc}\right)^{1.5} \left[\frac{(2-\alpha)\,(0.1+\alpha)}{1.3-\alpha}\right]^{0.75} \times \left(\frac{T}{10^4\ {\rm K}}\right)^{-0.075} \left[\left(\frac{S_\nu}{\rm mJy}\right)\left(\frac{\nu}{10\ {\rm GHz}}\right)^{-\alpha}\right]^{0.75} \times \left(\frac{V_{\rm jet}}{200\ {\rm km\ s^{-1}}}\right)\left(\frac{\nu_m}{10\ {\rm GHz}}\right)^{0.75\alpha-0.45} \times \left(\frac{\theta_0}{\rm rad}\right)^{0.75} (\sin\ i)^{-0.25}, \quad (3)$$

where α is the spectral index and S_ν is the radio continuum flux, both listed in Table 3, and d is the distance to the source. The opening angle of the jet θ_0 can be approximated as $2\arctan(\theta_{\rm min}/\theta_{\rm maj})$ (Beltrán et al. 2001; Anglada et al. 2018). We assumed a value of 0.5 for the ratio of the minor and major axis of the jet. We also assumed that the velocity of the jet ($V_{\rm jet}$) is 500 km s^{-1} and that it lies in the plane of the sky (i.e., sin $i = 1$). For a random orientation of the jet in the celestial plane, the value of sin i is on average $\pi/4$ (e.g., Beltrán et al. 2001). Usually, a value of $T = 10^4$ K is adopted for ionized gas. For the turnover frequency ν_m, we assumed a value of 40 GHz (see the discussion in Anglada et al. 2018). In Fig. 6 we show the relation between the mass-loss rates of the ionized and the molecular outflow for the thermal radio-jet candidates listed in Table 3 and associated with the molecular outflows. Major uncertainties in the determination of $\dot{M}_{\rm ion}$ may arise from parameters such as the jet velocity, the turnover frequency, or the aspect ratio of the jet because they cannot be determined from our observational data. However, their effects are almost negligible, and variations within reasonable ranges result in variations of the ionized mass-loss rate of less than a factor of 10. Our derived $\dot{M}_{\rm ion}$ are mainly in the range of 10^{-7} to 10^{-5} $M_\odot$ yr^{-1}, consistent with the values reported for low-mass radio-jets ($\approx 10^{-10}$ $M_\odot$ yr^{-1})

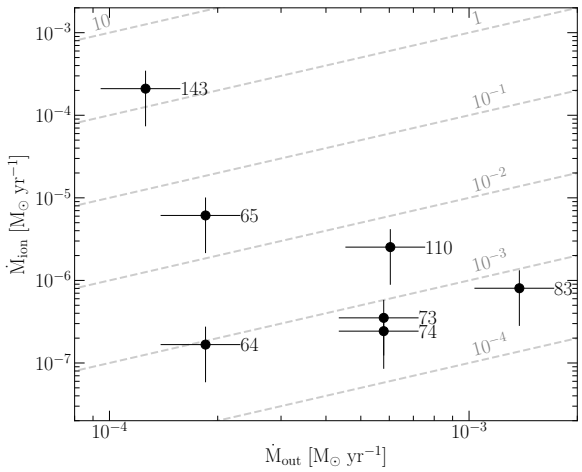

Fig. 6. Relation between ionized ($\dot{M}_{ion}$) and molecular outflow ($\dot{M}_{out}$) mass-loss rates for the radio-jet candidates listed in Table 3. The ionized mass-loss rate is derived for the thermal radio jets using Eq. (3), while the molecular outflow mass-loss rate is provided in López-Sepulcre et al. (2010) and Sánchez-Monge et al. (2013b). The dashed lines indicate different ionization levels given by the ratio $\dot{M}_{ion}$ to $\dot{M}_{out}$.

and high-mass radio-jets ($\approx 10^{-5}$ $M_\odot$ yr^{-1}, see Rodriguez et al. 1994; Beltrán et al. 2001; Guzmán et al. 2010, 2012). The dashed lines in Fig. 6 indicate different degrees of ionization for the mass-loss rate. Most of our radio-jet candidates, with the exception of source 143, which is probably associated with an already developed H II region (see Fig. 5 and discussion above), have ionization levels of $\dot{M}_{ion} = 10^{-3} \times \dot{M}_{out}$. These values are about one to two orders of magnitude lower than those reported in previous studies (see, e.g., Rodriguez et al. 1990; Hartigan et al. 1994; Bacciotti et al. 1995; Anglada et al. 2018). This difference may be due to uncertainties in the assumed parameters of Eq. (3), as well as to the fact that our molecular outflow emission is studied with a single dish (sensitive to all scale structures), while the radio-jet observations were carried out with a large interferometric configuration that probably resolved out part of the radio-jet emission.

4.5.3. Best radio-jet candidates

In previous sections, we have analyzed the properties of the 146 detected radio continuum sources and built a sample of possible radio jet candidates based on their association with outflow activity: molecular outflows, EGOs, and masers (see Table 3). In Sects. 4.5.1 and 4.5.2 we have investigated in more detail the possible nature of the radio continuum emission and its relation to the outflow activity tracers, in particular, the outflow momentum rate. The results presented in Figs. 3 and 5 allow us to identify sources with properties that differ from those expected from radio jets, which therefore suggests that these sources are not radio jets after all. From this analysis and the individual description of selected sources (see Appendix A), we discuss in this section which objects are most likely to be radio jets.

Out of the 28 sources listed in Table 3, 5 have radio luminosities similar to those expected for H II regions: sources 48a, 48b, 48c, 143, and 144 (see Fig. 3). In addition, all of these sources, with the exception of source143, have negative spectral indices. These negative values could be due to a slight extension of the sources (as expected for H II regions) and partial filtering-out in the K-band images. Moreover, these 5 sources also exhibit higher radio luminosities than their associated outflow momentum rates (see Fig. 5), which supports the interpretation that there may be an excess of radio continuum emission that is not necessarily associated with a radio jet, but with an H II region. In the absence of further evidence, we are not in a position to interpret further, and we cannot consider these sources to be among the best radio jet candidates. Further observations, sensitive to extended emission, can provide the necessary information to better characterize these sources in terms of their spatial extent and the nature of the emission. It is also worth noting that sources with negative spectral indices could correspond to background sources with synchrotron radiation because we expect about 11 objects in our sample to have this possible origin (see Sect. 3.1). Source 22 also shows an excess of radio continuum emission compared to its outflow momentum rate, which suggests that this is also a dubious radio-jet candidate. From the individual source descriptions presented in Appendix A, sources 42 and 137 seem to be radio continuum sources with most of their emission dominated by cometary/ultracompact H II regions, which makes it difficult to identify a radio jet in our data.

Out of the remaining sources listed in Table 3, we can identify seven that have a high probability to be radio jets. These are sources 2, 14, 22, 64, 74, 83, and 110, which are associated with additional outflow/shock activity such as masers and EGOs. Source 74 is adjacent to two H_2O maser features, which are only 2″ away and coincident with extended 4.5 μm emission (see Fig. A.7). The remaining sources do still classify as radio-jet candidates because we do not have clear evidence against it. Some of them are located at the center of molecular outflows (e.g., source 95) but are not associated with additional outflow/shock signs. This could be related to the variability of H_2O masers (see Sect. 4.5.1). Others are located within molecular outflow lobes (e.g., sources 12, 63, 64, 65, 73, and 144), and for which higher angular resolution observations of outflow tracers are necessary to confirm if they are powering some of the molecular outflows. Although they are not associated with molecular outflows, other sources show other shock activity signs such as the presence of EGOs (e.g., sources 119, 136, and 139). Further observational constraints are therefore needed to fully confirm or discard these objects as radio jets. The results acquired so far allow us to classify them as radio-jet candidates.

5. Implications for high-mass star formation

Recently, Rosero et al. (2019) studied the properties of 70 radio continuum sources associated with the earliest stages of high-mass star formation. They find that ≈30–50% of their sample are ionized jets. This fraction is in agreement with our findings. Out of the 146 radio continuum sources detected in our study, we identify 28 possible radio jets (i.e., about 19% of our sample). However, when we focus on the sources for which we have more accurate information (i.e., sources classified as iC/iK in Table B.1, see also Sect. 3.1), 24 out of 40 sources are potential radio jets. Therefore the percentage of radio continuum sources that are radio jets increases to 60%. This suggests that about half of the radio continuum sources found in star-forming regions at early evolutionary stages may indeed be radio jets powered by young stars. The remaining ≈50% of objects could still be radio jets for which we have not yet identified shock activity signs, or they could represent extremely compact H II regions in early stages of their development. These objects could be powered by early B-type stars and not necessarily by the most massive stars, and could be an intermediate stage between radio jets and already developed H II regions (see, e.g., Beltrán et al. 2016; Rivera-Soto et al. 2020).

López-Sepulcre et al. (2010) classified the regions studied in our work as infrared-dark (IRDC, infrared-dark cloud) and infrared-bright (HMSFR, high-mass star-forming region) based on their detectable infrared emission. Our sample therefore consists of two subclasses: IRDC (eight regions) and HMSFR (ten regions; see Table 1). We assume that these two types belong to different evolutionary phases of massive star formation, with the IRDC regions being less evolved than the HMSRF regions. Considering the 40 sources located within the primary beam of our images (i.e., sources classified as iC/iK), we find ≈2.8 radio continuum sources per HMSFR region, and ≈1.8 radio continuum sources per IRDC region. This suggests that it is more probable to detect compact radio continuum emission in more evolved regions. Regarding the presence of radio jets in these two evolutionary stages, we find 21 out of the 28 radio jet candidates listed in Table 3 in HMSFR regions (corresponding to 75%), while we only find 7 (corresponding to 25%) in the less evolved IRDC regions. When we consider only the best radio-jet candidates (see Sect. 4.5.3), we find five radio jets (sources 2, 14, 22, 64, and 83; corresponding to 71%) in HMSRF regions and two radio jets (sources 74 and 110; corresponding to 29%) in IRDC regions. This shows a preference of radio jets to be found in more evolved clouds. Complementary to this, we can determine the fraction of IRDC and HMSFR regions that harbor radio jets. Out of the eight IRDC regions studied in this work, only two (corresponding to 25%) harbor one of the best radio-jet candidates. This increases to 50% (five out of ten) for the HMSFR regions. This means that the frequency of radio jets in IRDC regions is lower than in HMSFR regions. One possible explanation is that the jets may become larger and brighter with time. Our limited data do not show that IRDC jets are smaller or fainter than HMSFR jets, but future work on larger source samples may provide further insight.

6. Summary

We have used of the VLA in two different bands (*C* and *K* band, corresponding to 6 and 1.3 cm wavelengths) to search for radio jets powered by high-mass YSOs. We studied a sample of 18 high-mass star-forming regions with signs of SiO and HCO^+ outflow activity. In the following we summarize our main results.

We have identified 146 radio continuum sources in the 18 high-mass star forming regions, with 40 of the radio continuum sources located within the primary beams of our images (i.e., labeled iC/iK and with reliable flux measurements). Out of these sources, 131 (27 iC/iKs) are only detected in the *C* band, 4 (3 iC/iKs) are only detected in the *K* band, and 11 (10 iC/iKs) are detected in both bands. This different detection level is likely due to different factors: (i) four regions were not observed in the *K* band, (ii) the *C*-band images have a larger field of view, and (iii) the *K*-band images are affected by a larger interferometric spatial filtering. In addition to the continuum emission, we detected 23 maser features in the 6.7 GHz CH_3OH and 22 GHz H_2O lines.

Out of the 146 continuum sources, only 40 sources are located within the field of view of both images, allowing for an accurate characterization of their radio properties. For these sources we derived the spectral index, which we find to be consistent with thermal emission (i.e., in the range −0.1 to +2.0) for most of the objects (73%).

We investigated the nature of the radio continuum emission by comparing the radio luminosity to the bolometric luminosity. We find that most sources with positive spectral indices (i.e., thermal emission) follow the trend expected for radio jets, while sources with large negative spectral indices seem to follow the relation expected for H II regions. These large negative spectral indices probably arise because the emission in the *K*-band images is partially filtered out.

Based on the association of the radio continuum sources with shock activity signs (i.e., association with molecular outflows, EGOs, or masers), we compiled a list of 28 radio-jet candidates. This corresponds to ≈60% of the radio continuum sources located within the field of view of both VLA images. In this sample of radio-jet candidates, we identified 7 objects (sources 2, 14, 22, 64, 74, 83, and 110) as the most probable radio jets. The remaining 21 require additional observations, either at different radio frequency bands or of molecular outflow tracers at higher resolution, to confirm or discard them as radio jets.

We find about 7–36% of the possible radio jet candidates to show nonthermal radio continuum emission. This is consistent with previous studies reporting ≈20% nonthermal radio jets. We do not find a clear association of the nonthermal emission with the presence of outflows, EGOs, or masers. However, despite the low statistics, we find that radio jet candidates associated with CH_3OH masers have thermal emission, while the radio-jet candidates associated with only H_2O masers tend to have nonthermal emission. This is in agreement with the 6.7 GHz CH_3OH masers tracing the actual location of newly born YSOs powering thermal winds and jets, while the H_2O masers may originate in strong shocks where nonthermal emission becomes relevant.

As previously found in other works, we find a correlation between the radio luminosity of our radio-jet candidates and their associated outflow momentum rates. We derive an ionized mass-loss rate in the range 10^{-7} to 10^{-5} $M_\odot$ yr^{-1}, which results in ionization levels of $\dot{M}_{ion} = 10^{-3}$ $\dot{M}_{out}$ (i.e., ≈0.1% of the outflow mass that is ionized).

The 18 high-mass star-forming regions studied in this work are classified into two different evolutionary stages: eight less evolved IRDC, and ten more evolved HMSFR. We find more radio continuum sources (≈2.8 sources per region) in the more evolved HMSFR than in the IRDC (≈1.8). Regarding radio jets, we find about 71% of the radio jet candidates to be located in HMSFR regions, and only 29% in IRDC regions. Complemenary to this, 25% of the IRDC regions harbor one of the most probable radio-jet candidates, while this percentage increases to 50% for the HMSFR regions. This suggests that the frequency of radio jets in the less evolved IRDC regions is lower than in the more evolved HMSFR regions.

Acknowledgements. The authors thank the referee for his/her review and greatly appreciate the comments and suggestions that have contributed significantly to improve the quality of the publication. Ü.K. also thanks Jonathan Tan for useful discussions. This work has been partially supported by the Scientific and Technological Research Council of Turkey (TÜBİTAK), project number: 116F003. Part of this work was supported by the Research Fund of Istanbul University, project number: 44 659. ASM research is carried out within the Collaborative Research Centre 956, sub-project A6, funded by the Deutsche Forschungsgemeinschaft (DFG; project ID 184 018 867). Ü.K. would like to thank William Pearson for checking the language of the paper and Kyle Oman for helping with Python issues.

References

Andre, P., Ward-Thompson, D., & Barsony, M. 2000, Protostars and Planets IV, eds. V. Mannings, A. P. Boss, & S. S. Russell (Tucson, AZ: University of Arizona Press), 59
Anglada, G. 1995, Rev. Mex. Astron. Astrof. Conf. Ser., 1, 67
Anglada, G. 1996, ASP Conf. Ser., 93, 3
Anglada, G., Rodriguez, L. F., Canto, J., Estalella, R., & Torrelles, J. M. 1992, ApJ, 395, 494

Anglada, G., Villuendas, E., Estalella, R., et al. 1998, AJ, 116, 2953
Anglada, G., Rodríguez, L. F., & Carrasco-González, C. 2018, A&ARv, 26, 3
Arce, H. G., Shepherd, D., Gueth, F., et al. 2007, Protostars and Planets V, eds. B. Reipurth, D. Jewitt, & K. Keil (Tucson, AZ: University of Arizona Press), 245
Ashimbaeva, N. T., Colom, P., Krasnov, V. V., et al. 2017, Astron. Rep., 61, 16
Azatyan, N. M., Nikoghosyan, E. H., & Khachatryan, K. G. 2016, Astrophysics, 59, 339
Bacciotti, F., Chiuderi, C., & Oliva, E. 1995, A&A, 296, 185
Bachiller, R. 1996, ARA&A, 34, 111
Bally, J. 2016, ARA&A, 54, 491
Battersby, C., Bally, J., Jackson, J. M., et al. 2010, ApJ, 721, 222
Beltrán, M. T., Estalella, R., Anglada, G., Rodríguez, L. F., & Torrelles, J. M. 2001, AJ, 121, 1556
Beltrán, M. T., Sánchez-Monge, Á., Cesaroni, R., et al. 2014, A&A, 571, A52
Beltrán, M. T., Cesaroni, R., Moscadelli, L., et al. 2016, A&A, 593, A49
Beuther, H., Schilke, P., Sridharan, T. K., et al. 2002a, A&A, 383, 892
Beuther, H., Walsh, A., Schilke, P., et al. 2002b, A&A, 390, 289
Breen, S. L., Ellingsen, S. P., Contreras, Y., et al. 2013, MNRAS, 435, 524
Carrasco-González, C., Rodríguez, L. F., Anglada, G., et al. 2010, Science, 330, 1209
Carrasco-González, C., Torrelles, J. M., Cantó, J., et al. 2015, Science, 348, 114
Caswell, J. L., & Green, J. A. 2011, MNRAS, 411, 2059
Caswell, J. L., Fuller, G. A., Green, J. A., et al. 2010, MNRAS, 404, 1029
Cesaroni, R., Sánchez-Monge, Á., Beltrán, M. T., et al. 2016, A&A, 588, L5
Cesaroni, R., Sánchez-Monge, Á., Beltrán, M. T., et al. 2017, A&A, 602, A59
Chini, R., Kruegel, E., & Wargau, W. 1987, A&A, 181, 378
Condon, J. J., Cotton, W. D., Greisen, E. W., et al. 1998, AJ, 115, 1693
Curiel, S., Canto, J., & Rodriguez, L. F. 1987, Rev. Mex. Astron. Astrofis, 14, 595
Curiel, S., Rodríguez, L. F., Cantó, J., et al. 1989, Astrophys. Lett. Commun., 27, 299
Cutri, R. M., Wright, E. L., Conrow, T. et al. 2012, Explanatory Supplement to the WISE All-Sky Data Release Products
Cyganowski, C. J., Whitney, B. A., Holden, E., et al. 2008, AJ, 136, 2391
Cyganowski, C. J., Brogan, C. L., Hunter, T. R., & Churchwell, E. 2009, ApJ, 702, 1615
Cyganowski, C. J., Brogan, C. L., Hunter, T. R., & Churchwell, E. 2011, ApJ, 743, 56
Cyganowski, C. J., Brogan, C. L., Hunter, T. R., et al. 2012, ApJ, 760, L20
Cyganowski, C. J., Koda, J., Rosolowsky, E., et al. 2013, ApJ, 764, 61
De Buizer, J. M., Radomski, J. T., Telesco, C. M., & Piña, R. K. 2005, ApJS, 156, 179
de Villiers, H. M., Chrysostomou, A., Thompson, M. A., et al. 2015, MNRAS, 449, 119
Elitzur, M. 1982, Rev. Mod. Phys., 54, 1225
Felli, M., Brand, J., Cesaroni, R., et al. 2007, A&A, 476, 373
Froebrich, D., Makin, S. V., Davis, C. J., et al. 2015, MNRAS, 454, 2586
Gasiprong, N., Cohen, R. J., & Hutawarakorn, B. 2002, MNRAS, 336, 47
Gaume, R. A., Fey, A. L., & Claussen, M. J. 1994, ApJ, 432, 648
Ginsburg, A., Glenn, J., Rosolowsky, E., et al. 2013, ApJS, 208, 14
Gordon, M. A., & Sorochenko, R. L. 2002, Radio Recombination Lines. Their Physics and Astronomical Applications (New York: Springer), 282
Guzmán, A. E., Garay, G., & Brooks, K. J. 2010, ApJ, 725, 734
Guzmán, A. E., Garay, G., Brooks, K. J., & Voronkov, M. A. 2012, ApJ, 753, 51
Hartigan, P., Morse, J. A., & Raymond, J. 1994, ApJ, 436, 125
Hatchell, J., Fuller, G. A., & Millar, T. J. 2001, A&A, 372, 281
Helfand, D. J., Becker, R. H., White, R. L., Fallon, A., & Tuttle, S. 2006, AJ, 131, 2525
Hoare, M. G., Purcell, C. R., Churchwell, E. B., et al. 2012, PASP, 124, 939
Johnston, K. G., Robitaille, T. P., Beuther, H., et al. 2015, ApJ, 813, L19
Kalenskii, S. V., & Kurtz, S. 2016, Astron. Rep., 60, 702
Kuchar, T. A., & Clark, F. O. 1997, ApJ, 488, 224
Kurtz, S. 2005, IAU Symp., 227, 111
Kurtz, S., Churchwell, E., & Wood, D. O. S. 1994, ApJS, 91, 659
Larson, R. B. 1969, MNRAS, 145, 271
Lekht, E. E. 2000, A&AS, 141, 185
Leto, P., Umana, G., Trigilio, C., et al. 2009, A&A, 507, 1467
Liu, T., Wu, Y., & Zhang, H. 2013, ApJ, 776, 29
Lockman, F. J. 1989, ApJS, 71, 469
López-Sepulcre, A., Codella, C., Cesaroni, R., Marcelino, N., & Walmsley, C. M. 2009, A&A, 499, 811
López-Sepulcre, A., Cesaroni, R., & Walmsley, C. M. 2010, A&A, 517, A66
López-Sepulcre, A., Walmsley, C. M., Cesaroni, R., et al. 2011, A&A, 526, L2
Lu, X., Zhang, Q., Liu, H. B., Wang, J., & Gu, Q. 2014, ApJ, 790, 84
Luhman, K. L. 2012, ARA&A, 50, 65
Lumsden, S. L., Hoare, M. G., Urquhart, J. S., et al. 2013, ApJS, 208, 11
Marti, J., Rodriguez, L. F., & Reipurth, B. 1993, ApJ, 416, 208
Maud, L. T., Cesaroni, R., Kumar, M. S. N., et al. 2019, A&A, 627, L6
McMullin, J. P., Waters, B., Schiebel, D., Young, W., & Golap, K. 2007, ASP Conf. Ser., 376, 127
Moscadelli, L., Cesaroni, R., & Rioja, M. J. 2005, A&A, 438, 889
Moscadelli, L., Cesaroni, R., Sánchez-Monge, Á., et al. 2013, A&A, 558, A145
Moscadelli, L., Sánchez-Monge, Á., Goddi, C., et al. 2016, A&A, 585, A71
Moscadelli, L., Sanna, A., Goddi, C., et al. 2019, A&A, 631, A74
Motte, F., Nony, T., Louvet, F., et al. 2018, Nat. Astron., 2, 478
Palau, A., Sánchez-Monge, Á., Busquet, G., et al. 2010, A&A, 510, A5
Purcell, C. R., Hoare, M. G., Cotton, W. D., et al. 2013, ApJS, 205, 1
Purser, S. J. D., Lumsden, S. L., Hoare, M. G., & Cunningham, N. 2018, MNRAS, 475, 2
Rathborne, J. M., Jackson, J. M., & Simon, R. 2006, ApJ, 641, 389
Rathborne, J. M., Simon, R., & Jackson, J. M. 2007, ApJ, 662, 1082
Reid, M. J., & Ho, P. T. P. 1985, ApJ, 288, L17
Reid, M. J., Argon, A. L., Masson, C. R., Menten, K. M., & Moran, J. M. 1995, ApJ, 443, 238
Reynolds, S. P. 1986, ApJ, 304, 713
Rivera-Soto, R., Galván-Madrid, R., Ginsburg, A., & Kurtz, S. 2020, ApJ, 899, 94
Rodriguez, L. F. 1995, Rev. Mex. Astron. Astrofis. Conf. Ser., 1, 1
Rodriguez, L. F., Ho, P. T. P., Torrelles, J. M., Curiel, S., & Canto, J. 1990, ApJ, 352, 645
Rodriguez, L. F., Garay, G., Curiel, S., et al. 1994, ApJ, 430, L65
Rodríguez, L. F., Moran, J. M., Franco-Hernández, R., et al. 2008, AJ, 135, 2370
Rosero, V., Hofner, P., Claussen, M., et al. 2016, ApJS, 227, 25
Rosero, V., Hofner, P., Kurtz, S., et al. 2019, ApJ, 880, 99
Roueff, E., Dartois, E., Geballe, T. R., & Gerin, M. 2006, A&A, 447, 963
Sánchez-Monge, Á., Palau, A., Estalella, R., Beltrán, M. T., & Girart, J. M. 2008, A&A, 485, 497
Sánchez-Monge, Á., Cesaroni, R., Beltrán, M. T., et al. 2013a, A&A, 552, L10
Sánchez-Monge, Á., López-Sepulcre, A., Cesaroni, R., et al. 2013b, A&A, 557, A94
Sánchez-Monge, Á., Kurtz, S., Palau, A., et al. 2013c, ApJ, 766, 114
Sánchez-Monge, Á., Beltrán, M. T., Cesaroni, R., et al. 2013d, A&A, 550, A21
Sánchez-Monge, Á., Beltrán, M. T., Cesaroni, R., et al. 2014, A&A, 569, A11
Sanna, A., Moscadelli, L., Goddi, C., Krishnan, V., & Massi, F. 2018, A&A, 619, A107
Sanna, A., Moscadelli, L., Goddi, C., et al. 2019, A&A, 623, L3
Sewiło, M., Churchwell, E., Kurtz, S., Goss, W. M., & Hofner, P. 2011, ApJS, 194, 44
Shepherd, D. S., Nürnberger, D. E. A., & Bronfman, L. 2004, ApJ, 602, 850
Stecklum, B., Caratti o Garatti, A., Klose, S., & Wiseman, P. 2017, ATel, 10, 842, 1
Sugiyama, K., Nagase, K., Yonekura, Y., et al. 2017, PASJ, 69, 59
Tan, J. C., Beltrán, M. T., Caselli, P., et al. 2014, Protostars and Planets VI, eds. H. Beuther, R. S. Klessen, C. P. Dullemond, & T. Henning (Tucson, AZ: University of Arizona Press), 149
Thompson, R. I. 1984, ApJ, 283, 165
Torrelles, J. M., Ho, P. T. P., Rodriguez, L. F., & Canto, J. 1985, ApJ, 288, 595
Torrelles, J. M., Patel, N. A., Curiel, S., et al. 2011, MNRAS, 410, 627
Urquhart, J. S., Hoare, M. G., Lumsden, S. L., Oudmaijer, R. D., & Moore, T. J. T. 2008, ASP Conf. Ser., 387, 381
Williams, J. P., & Cieza, L. A. 2011, ARA&A, 49, 67

Appendix A: Comments on individual sources

In the following, we comment on various aspects of selected sources for which additional literature information is available. We presented the region(s) where the radio-jet maps with outflow emission contours are given.

IRAS 05358+3543 (sources 2 and 4)

In region IRAS 05358+3543, we identified two radio continuum sources that can be potential radio jets (see Fig. A.1). Sources 2 and 4 were observed only in the *C* band, and therefore we cannot determine a spectral index for these sources. Despite this limitation, both sources are located at the center of the molecular outflow reported by López-Sepulcre et al. (2010). Furthermore, source 2 is associated with a 6.7 GHz CH_3OH maser emission, suggesting that this marks the position of a massive YSO. Of the two radio continuum sources, source 2 is likely the main object powering the molecular outflow for which its centimeter emission traces a radio jet. Further observations at different frequency bands are necessary to better constrain its properties.

G189.78+0.34 (sources 12, 13, 14, 15, and 16)

In region G189.78+0.34, we identified five radio continuum sources (sources 12 to 16) associated with the molecular outflow reported by López-Sepulcre et al. (2010). All of them are located at the center of the outflow, with source 12 slightly offset from the rest (see Fig. A.2). All these sources were observed only in the *C* band, and no spectral index can be derived. Out of the five sources, source 14 is associated with CH_3OH maser emission (see also Caswell et al. 2010), suggesting that this marks the location of a massive YSO. The radio continuum sources are found in an elongated chain extending from the southeast to the northwest. This direction is consistent with the orientation of the molecular outflow (López-Sepulcre et al. 2010). Overall, we consider that source 14 is the powering source and most likely the main component of the radio jet. The other sources could correspond to different radio continuum knots located along the jet, as seen in other sources (e.g., HH 80-81: Carrasco-González et al. 2010, and G35.20−0.74 N: Beltrán et al. 2016), where the radio continuum knots usually show nonthermal spectral indices. Observations at different frequency bands are necessary to gather information on the spectral index and thermal/nonthermal nature of the different radio continuum sources in the region.

G192.58−0.04 (sources 22, 23, and 25)

In region G192.58−0.04, we identified sources 22, 23, and 25 as potential radio jets (see Fig. A.3). These sources were observed only in the *C* band and no spectral index can be derived. Out of the three sources, source 22 is associated with CH_3OH maser emission, suggesting that this source may mark the location of a massive YSO. The sources are located at the center of the molecular outflow reported by López-Sepulcre et al. (2010). Out of the three sources, we consider that source 22 is the most probable radio jet. The comparison between the radio continuum luminosity with the outflow momentum rate (see Fig. 5) also confirms this possibility, although there appears to be a slight excess of radio continuum emission, suggesting that there can be an additional contribution to the radio continuum source (e.g., from an H II region in an early stage).

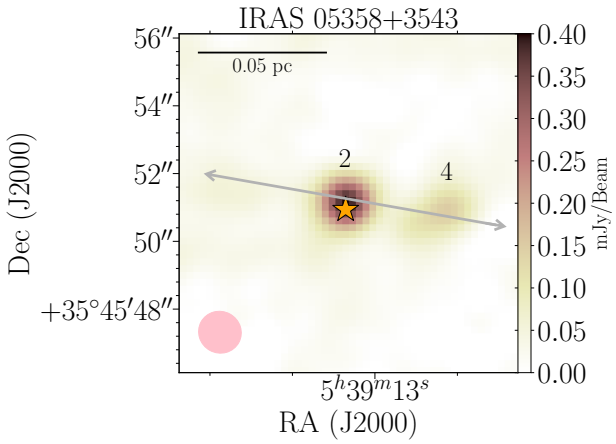

Fig. A.1. VLA *C*-band (6 cm) continuum emission map of radio-jet candidates 2 and 4 located in the region IRAS 05358+3543. The pink ellipse is the beam size of the *C* band. The orange star marks the location of the CH_3OH maser (see Table 2). The gray double-headed arrow indicates the direction of the outflows.

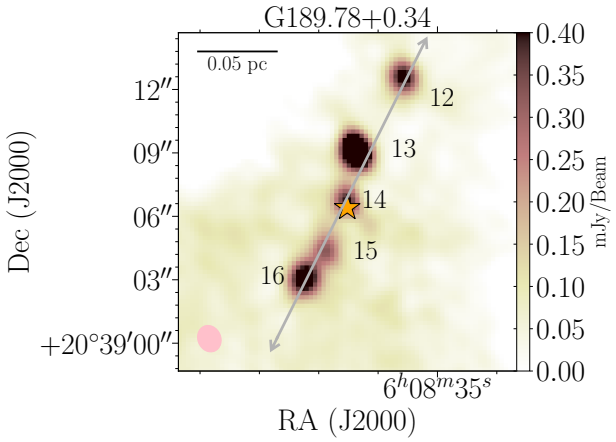

Fig. A.2. VLA *C*-band (6 cm) continuum emission map of radio jet candidates 12, 13, 14, 15, and 16 located in the region G189.78+0.34. The pink ellipse is the beam size of the *C* band. The orange star marks the location of the CH_3OH maser (see Table 2). The gray double-headed arrow indicates the direction of the outflows.

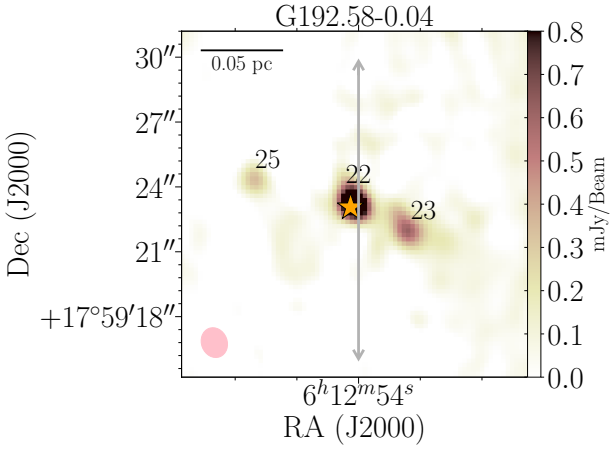

Fig. A.3. VLA *C*-band (6 cm) continuum emission map of radio-jet candidates 22, 23, and 25 located in the region G192.58−0.04. The pink ellipse is the beam size of the *C* band. The orange star marks the location of the CH_3OH maser (see Table 2). The gray double-headed arrow indicates the direction of the outflows.

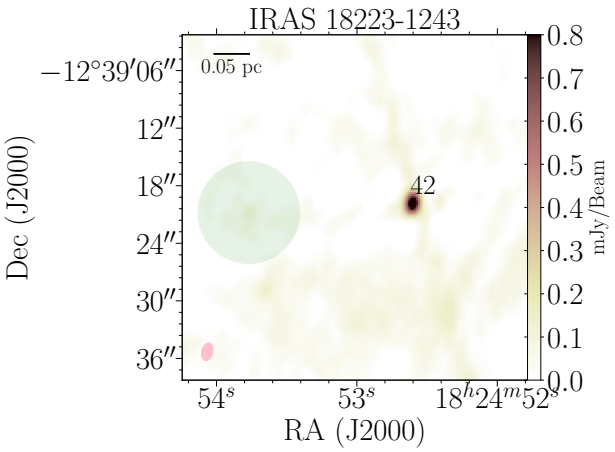

Fig. A.4. VLA *C*-band (6 cm) continuum emission map of radio-jet candidate 42 located in the region IRAS 18223−1243. The pink ellipse is the beam size of the *C* band. The green circle with a radius of ∼5″ marks the EGO F G18.67+0.03-CM1 reported by Cyganowski et al. (2011).

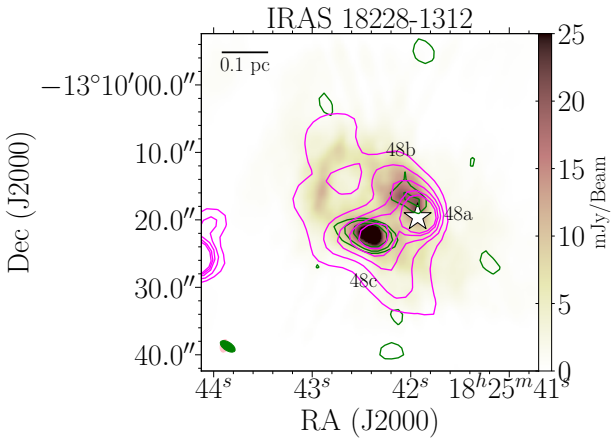

Fig. A.5. VLA *C*-band (6 cm) continuum emission map of source 48 located in the region IRAS 18228−1312. Three bright peaks are visible and labeled 48a, 48b, and 48c. The green contour levels of the *K*-band (1.3 cm) continuum emission are 3, 5 and 9 times 0.7 mJy beam^{-1}. The magenta contours show the *Spitzer*/GLIMPSE 4.5 μm emission. The pink and green ellipses are the beam sizes of the *C* and *K* bands, respectively. The white star marks the location of the H_2O maser (see Table 2).

IRAS 18223−1243 (source 42)

In the region IRAS 18223−1243, we identified the radio continuum source 42 (see Fig. A.4) as adjacent to the one reported in Cyganowski et al. (2011) EGO F G18.67+0.03−CM1. This is the only sign of shock activity because neither molecular outflow nor maser emission are found for this object. In addition, Cyganowski et al. (2012) reported a massive protocluster consisting of a hot molecular core and an ultracompact H II region. Our source appears to be located at the same position as the ultracompact H II region, which makes us to doubt whether this can be a radio-jet candidate.

IRAS 18228−1312 (source 48)

Radio continuum source 48 is observed as a group of three compact sources (sources 48a, 48b, and 48c) surrounded by an extended and more diffuse structure. One of these compact sources (source 48a) is clearly associated with H_2O maser emission (see Fig. A.5). The *Spitzer*/IRAC 4.5 μm emission is extended and spatially coincident with the radio continuum extended emission. The spectral indices for these three compact sources are in the range −0.6 to −1.5, most likely due to additional filtering of the emission in the *K*-band image. Previous studies have classified this extended source as a region containing hypercompact (HC) and ultracompact (UC) H II regions (e.g., Chini et al. 1987; Lockman 1989; Kurtz et al. 1994; Kuchar & Clark 1997; Leto et al. 2009), which is consistent with our derived radio continuum luminosity (see Figs. 3 and 5). The three sources are spatially located at the center of a molecular outflow (e.g., López-Sepulcre et al. 2010). This may suggest that one of the compact sources may be powering the molecular outflow. In this case, this object would be in a evolutionary stage where the radio jet still exists but a young H II region has already developed, similar to the high-mass young stellar object G35.20−0.74 N (e.g., Sánchez-Monge et al. 2013a, 2014; Beltrán et al. 2016).

IRAS 18236−1205 (sources 63, 64, and 65)

We identified nine radio continuum sources in the IRAS 18236−1205 region (also referred to in the literature as G19.36−0.03), three of which have been classified as radio jet candidates: sources 63, 64, and 65 with spectral indices of -0.22 ± 0.07, $+0.18 \pm 0.04$, and $+1.08 \pm 0.19$. We identified four H_2O maser features near these sources (see Fig. A.6). Two maser features are associated with source 63, one maser feature is associated with source 64 (which also spatially coincides with a CH_3OH maser), and the last maser feature is located in the center of the redshifted outflow lobe where no radio continuum emission is detected. The molecular outflow in this region has been mapped in the lines SiO (2–1) and HCO^+ (1–0) by Sánchez-Monge et al. (2013b).

Sources 63 and 64 are associated with EGOs (see Cyganowski et al. 2009), indicating strong shock activity in these two sources. Their location near the center of the molecular outflow together with their association with H_2O maser emission and EGOs suggests that these two sources could be candidates for radio jets. Source 64 is spatially more coincident with the geometric center of the outflow, and its association with 6.7 GHz CH_3OH maser emission suggests that a massive YSO is located at this position. This massive YSO could be the driving source of the molecular outflow seen on larger scales. The third candidate (source 65) is located ∼28″ away from source 64 and the center of the outflow, and has been studied by Cyganowski et al. (2011, G19.36-0.03-CM2). This source is associated with an emission of 4.5 μm, although it is unclear whether it can be convincingly classified as an EGO (Cyganowski et al. 2009). The positive spectral index indicates thermal emission, which could come from a radio jet. However, there is no clear evidence of outflow or shock activity. Source 65 is also located in the vicinity of a dense core (18236−1205 P8) identified by Lu et al. (2014) in the VLA NH_3 maps, which supports the interpretation of this source as an embedded YSO. Overall, source 65 could be a YSO-powered radio jet in the vicinity of the more massive object (sources 63 and 64) in IRAS 18236−1205.

G23.60+0.0M1 (sources 73 and 74)

The G23.60+0.01M1 star-forming region has been studied in the literature by various authors (e.g., Rathborne et al. 2006;

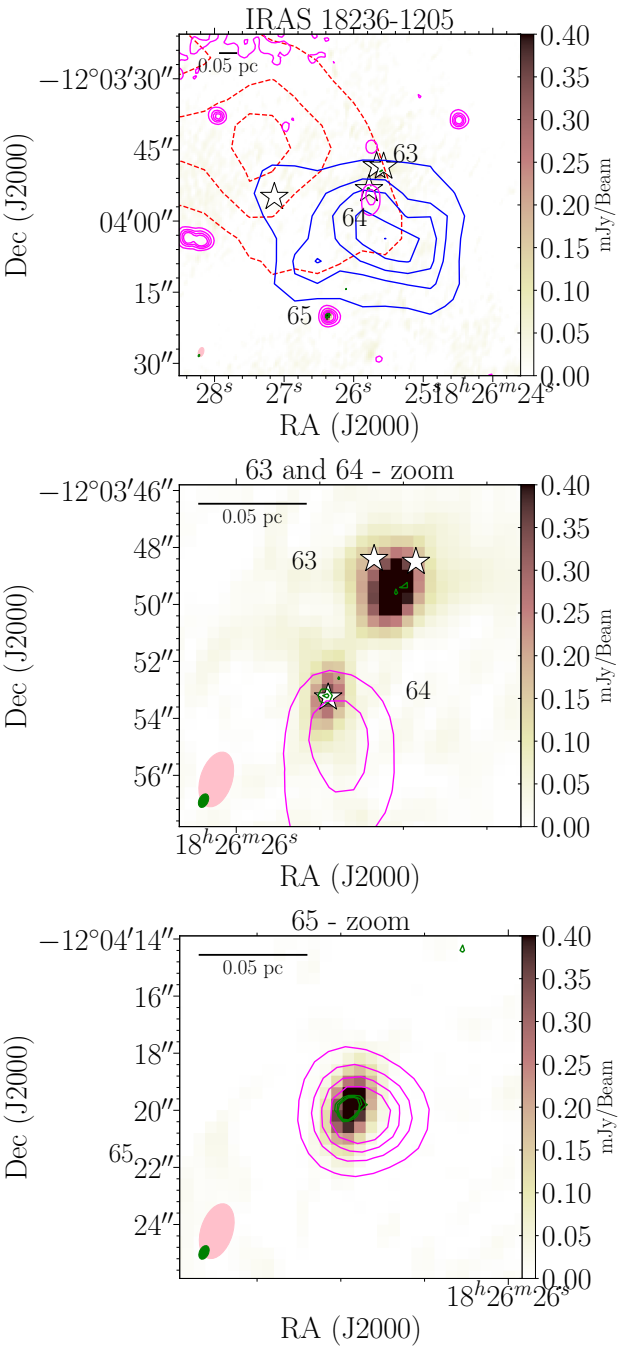

Fig. A.6. VLA *C*-band (6 cm) continuum emission map of radio-jet candidates 63, 64, and 65 located in the region IRAS 18236−1205. A close-up view of the three radio sources is shown in the *middle and bottom panels*. The green contour levels of the *K*-band (1.3 cm) continuum emission are 3, 5, and 7 times 30 μJy beam^{-1}. The magenta contours show the *Spitzer*/GLIMPSE 4.5 μm emission. The blue- and redshifted outflow lobes of SiO (2−1) are shown as solid blue and dashed red contours, respectively (see Sánchez-Monge et al. 2013b). The pink and green ellipses are the beam sizes of the *C* and *K* bands, respectively. The white stars mark the location of the H_2O masers (see Table 2).

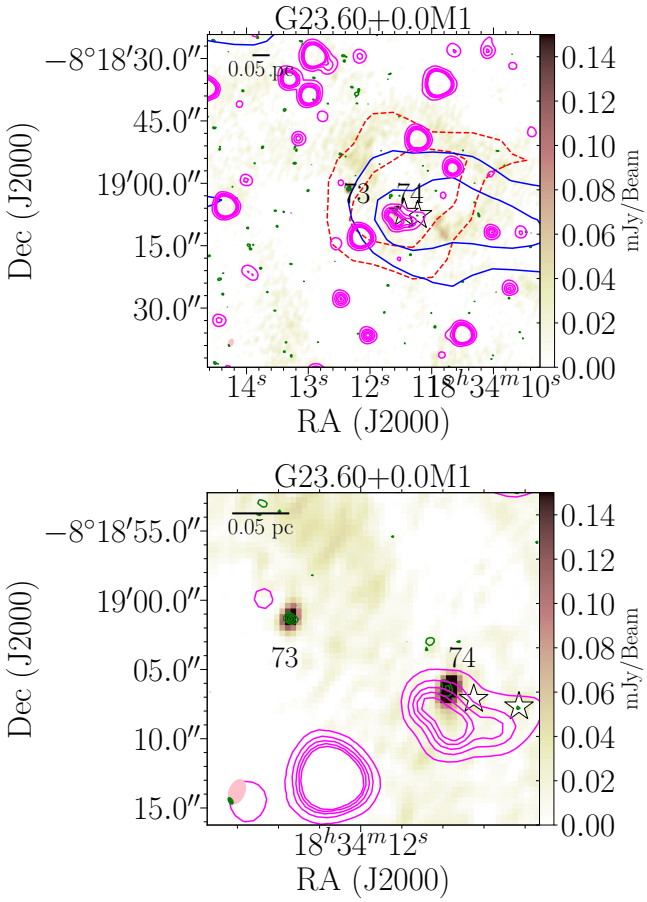

Fig. A.7. VLA *C*-band (6 cm) continuum emission map of radio jet candidates 73 and 74 located in the region G23.60+0.0M1. A close-up view of the two radio sources is shown in the *bottom panel*. The green contour levels of the *K*-band (1.3 cm) continuum emission are 3, 5, 7, 9, and 11 times 20 μJy beam^{-1}. The magenta contours show the *Spitzer*/GLIMPSE 4.5 μm emission. The blue- and redshifted outflow lobes of SiO (2−1) are shown as solid blue and dashed red contours, respectively (see Sánchez-Monge et al. 2013b). The pink and green ellipses are the beam sizes of the *C* and *K* bands, respectively. The white stars mark the location of the H_2O masers (see Table 2).

Battersby et al. 2010; Ginsburg et al. 2013), who reported the presence of two massive dense clumps with masses of 100 $M_\odot$ and 120 $M_\odot$. The two candidate radio jets (73 and 74) have positive spectral indices consistent with thermal emission of radio jets. In particular, source 74 is located at the center of the molecular outflow reported by Sánchez-Monge et al. (2013b) and is associated with a strong 4.5 μm emission (see Fig. A.7). The two H_2O masers detected in the region are slightly displaced from the radio continuum source, but coincide with the extended 4.5 μm emission (see Fig. A.7-bottom). The association of molecular outflow emission, bright and extended 4.5 μm emission, and close H_2O maser features favor the interpretation of this source as a good radio-jet candidate.

The second radio continuum source (source 73) is located relatively close to the center of the outflow. However, no maser or EGOs are found in connection with the source. Although we cannot reject this source as a radio jet, we prefer source 74 as the main object driving the outflow observed in the region.

IRAS 18316−0602 (sources 83 and 95)

We identified 13 radio continuum sources in the IRAS 18316−0602 region, 2 of which were classified as radio-jet candidates: sources 83 and 95. Source 83 has an almost flat spectral index (0.08 ± 0.08) and shows a weak extension to the south, which is better resolved in the *K*-band image. Source

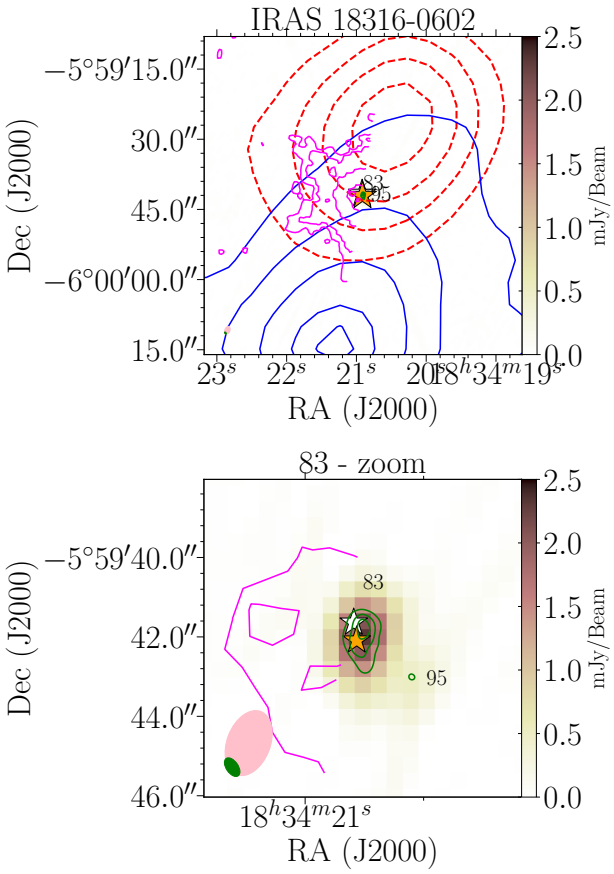

Fig. A.8. VLA *C*-band (6 cm) continuum emission map of radio jet candidates 83 and 95 located in the region IRAS 18316−1602. A close-up view of the two radio sources is shown in the *bottom panel*. The green contour levels of the *K*-band (1.3 cm) continuum emission are 3, 5, 9, and 11 times 27 μJy beam^{-1}. The magenta contours show the *Spitzer*/GLIMPSE 4.5 μm emission (note that half of the region was not covered in the mapped area). The blue- and redshifted outflow lobes of SiO (2−1) are shown as solid blue and dashed red contours, respectively (see Sánchez-Monge et al. 2013b). The pink and green ellipses are the beam sizes of the *C* and *K* bands, respectively. The white and orange stars mark the location of the H_2O and CH_3OH masers, respectively (see Table 2).

95 is fainter, appears to be located about 3″to the southeast of source 83, and is visible only in the *K* band (some faint emission slightly above the noise level is visible in the *C*-band image, see Fig. A.8). As for the maser emission, we identified both a H_2O and a CH_3OH maser feature associated with the brightest source 83. This source has been studied in previous works (e.g., Roueff et al. 2006; Cutri et al. 2012; Azatyan et al. 2016; Stecklum et al. 2017), in some of them, it is called RAFGL 7009S. The source is detected in the near-infrared together with two other objects separated by about 10″, and it is surrounded by a diffuse and extended structure (see, e.g., Stecklum et al. 2017).

López-Sepulcre et al. (2010) and Sánchez-Monge et al. (2013b) reported on the molecular outflow emission in the region. The blue and red contours in Fig. A.8 show the SiO (2–1) blueshifted and redshifted outflow emission. The two radio continuum sources (83 and 95) are located close to the center of the outflow. Although this region was not included in the Cyganowski et al. (2008, 2009, 2011) surveys, we identified a bright 4.5 μm source in the *Spitzer*/GLIMPSE data. However, the source is located at the edge of the area surveyed by *Spitzer*, which prevents a detailed characterization of its infrared

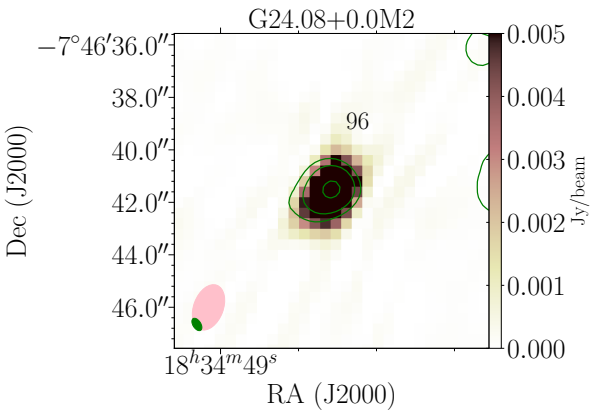

Fig. A.9. VLA *C*-band (6 cm) continuum emission map of radio source 96 located in the region G24.08+0.0M2. The green contour levels of the *K*-band (1.3 cm) continuum emission are 3, 5, and 9 times 20 μJy beam^{-1}. The pink and green ellipses are the beam sizes of the *C* and *K* bands, respectively.

emission. The association of source 83 with a 6.7 GHz CH_3OH maser emission suggests that this source harbors a massive YSO. Together with its central location within the outflow and its association with a H_2O maser, this indicates that this source is the radio jet that drives the outflow. The almost flat spectral index may indicate that this is a fully ionized radio jet. However, further observations in different frequency bands may help to better determine the spectral index and the status of radio continuum emission.

G24.08+0.0 M2 (source 96)

We identified 14 radio continuum sources in the region G24.08+0.0 M2, one of which, source 96, is detected in both frequency bands and has a negative spectral index ($-0.84 \pm +0.08$, see Fig. A.9). The outflow activity in the region has been studied by López-Sepulcre et al. (2011) and Sánchez-Monge et al. (2013b), who found molecular outflow in different tracers. However, this outflow is not spatially related to any of the radio continuum sources identified in this work. Moreover, this source could be a background source.

G24.33+0.1 M1 (source 110)

In the region G24.33+0.1 M1 we identified a radio continuum source (source 110) located in the center of our field of view and detected in both frequency bands (see Fig. A.10). This source has a positive spectral index of $+0.73 \pm 0.35$, which is consistent with thermal emission. We also detected maser features of both H_2O and CH_3OH associated with the continuum source. In addition, other authors have reported OH masers towards this object (see, e.g., Caswell & Green 2011). Rathborne et al. (2007) studied this source in the millimeter regime and identified a singular compact source with a rich chemistry characteristic of hot molecular cores. Sánchez-Monge et al. (2013b) reported molecular outflow activity, with source 110 at its geometric center. Overall, this source is one of the best candidates for a thermal radio jet.

G24.60+0.1M1 (source 119)

The only information we have for source 119 is that it is associated with an EGO. The nearest studied object is a extended H_2

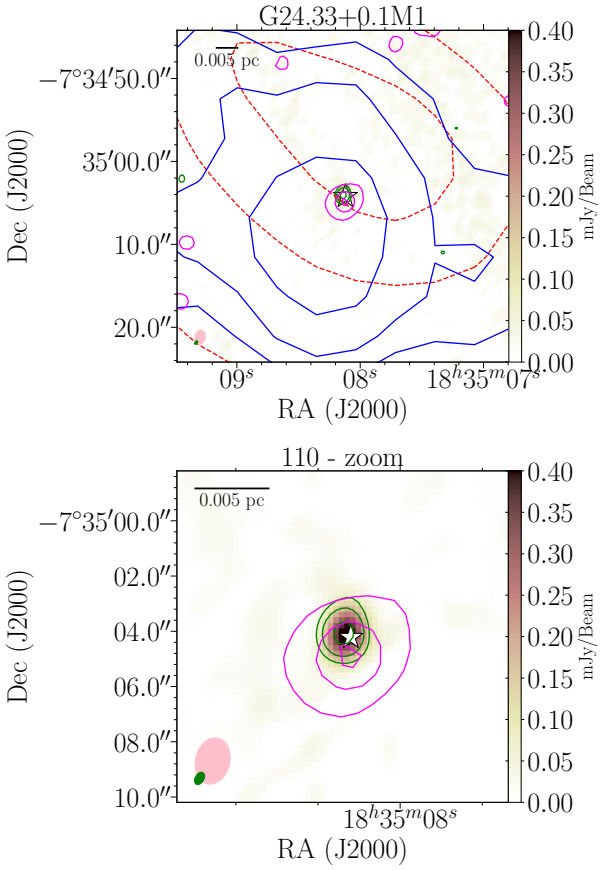

Fig. A.10. VLA *C*-band (6 cm) continuum emission map of radio-jet candidate 110 located in the region G24.33+0.1 M1. A close-up view of the radio source is shown in the *bottom panel*. The green contour levels of the *K*-band (1.3 cm) continuum emission are 3, 5, and 9 times 7 μJy beam^{-1}. The blue- and redshifted outflow lobes of SiO (2−1) are shown as solid blue and dashed red contours, respectively (see Sánchez-Monge et al. 2013b). The pink and green ellipses are the beam sizes of the *C* and *K* bands, respectively. The white star marks the location of the H_2O (see Table 2).

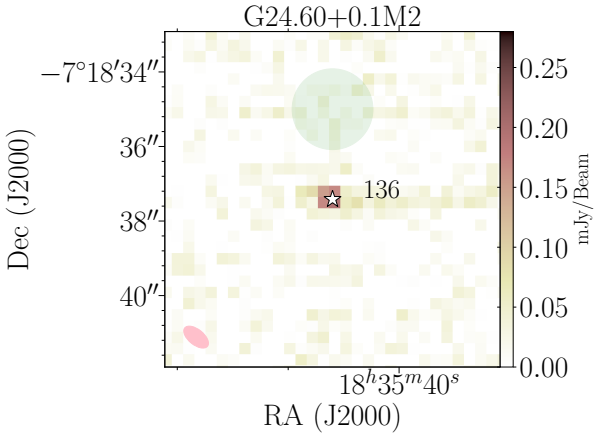

Fig. A.11. VLA *K*-band (1.3 cm) continuum emission map of radio-jet candidate 136 located in the region G24.60+0.1 M2. The green circle with a radius of ∼4″ marks EGO G24.63+0.15, reported by Cyganowski et al. (2008). The pink ellipse is the beam size of the *K* band. The white star marks the location of the H_2O (see Table 2).

emission that is 19″ away from source 119 (Froebrich et al. 2015). We cannot determine the spectral index because the source is outside the primary beam of the *K*-band images, but we propose that source 119 is a radio jet.

G24.60+0.1M2 (136)

Source 136 is detected only in the *K* band, resulting in a spectral index limit (>+1.67) that is consistent with thermal emission. The source is associated with H_2O maser emission. This source, although not directly associated with one EGO, is located in the vicinity of G24.63+0.15 reported by Cyganowski et al. (2008, see green circle in Fig. A.11). Rathborne et al. (2007) suggested that the main dense condensation, hosting source 136, may contain several condensations, referred to as G024.60+00.08 MM1 (A, B, and C). Our radio continuum source appears to be related to component C which is an IRDC condensation. Further observations of this object are necessary to confirm its possible nature as a radio jet.

G34.43+0.2M3 (sources 137 and 139)

Our radio continuum observations toward the region G34.43+0.2 M3 have led to the discovery of six radio continuum sources, although most of them are located far from the central region studied in Sánchez-Monge et al. (2013b). The brightest source is source 137, which is about 13′ from the phase center of our observations, that is, the source is outside the primary beam responses of the VLA antennas on both bands. This object is so bright that it is detected in both the *C* and *K* bands. At 6 cm, the source appears as a comet-like structure (see Fig. A.12), which resembles cometary H II regions. The 1.3 cm continuum emission also shows an arc-shaped structure shifted to the east, probably tracing the head of the cometary object. This source, referred to in the literature as G34.26+0.15, has been studied by other authors who reported two hypercompact H II regions (A and B) and one ultracompact H II region (C), all marked in the figure (see also Reid & Ho 1985; Gaume et al. 1994; Sewiło et al. 2011). Various studies (e.g., Hatchell et al. 2001; Liu et al. 2013) have reported outflow activity in this region, but no information on the outflow energetics such as the outflow momentum rate is reported. Although this source is associated with an EGO (Cyganowski et al. 2008) and with a molecular outflow, the bright emission together with previous studies suggests that a major fraction of the radio continuum emission we detected originates in a H II region rather than in a radio jet. Source 139 in the region is also classified as a radio-jet candidate in Table 3. However, the only information we have for this object is its association with an EGO (i.e., G34.41+0.24, Cyganowski et al. 2008). Shepherd et al. (2004) suggested that the embedded object (G34.4 MM) appears to be a massive B2 protostar at an early stage of evolution. This region is also associated with the H_2O maser activity (Cyganowski et al. 2013), which may favor a radio-jet origin for the detected radio continuum emission. Further observations are needed to better constrain its properties.

IRAS 19095+0930 (sources 143 and 144)

We identified four radio continuum sources in the region IRAS 19095+0930, also known in the literature as G43.80−0.13. Two of these radio sources, sources 143 and 144, are located close to each other and in the center of a molecular outflow (Sánchez-Monge et al. 2013b, see also Fig. A.13). Source 143 has a brighter flux, is also clearly visible in the *K*-band image, and is associated with H_2O maser emission features.

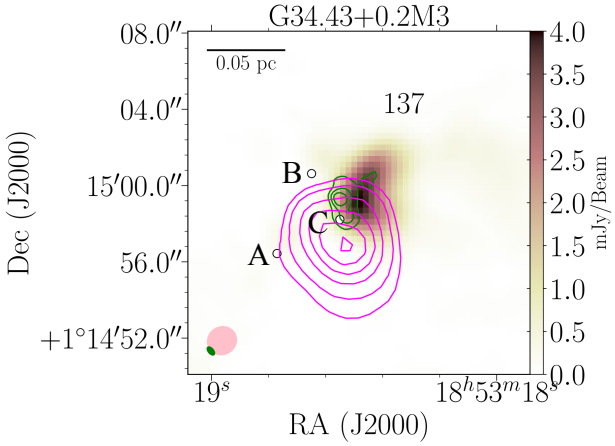

Fig. A.12. VLA *C*-band (6 cm) continuum emission map of radio-jet candidate 137 located in the region G34.43+0.2 M3. The green contour levels of the *K*-band (1.3 cm) continuum emission are 3, 5, and 7 times 20 μJy beam^{-1}. The magenta contours show the *Spitzer*/GLIMPSE 4.5 μm emission. The pink and green ellipses are the beam sizes of the *C* and *K* bands, respectively. The white circles (A, B, and C) mark the position of the 2 mm continuum sources reported by Gasiprong et al. (2002).

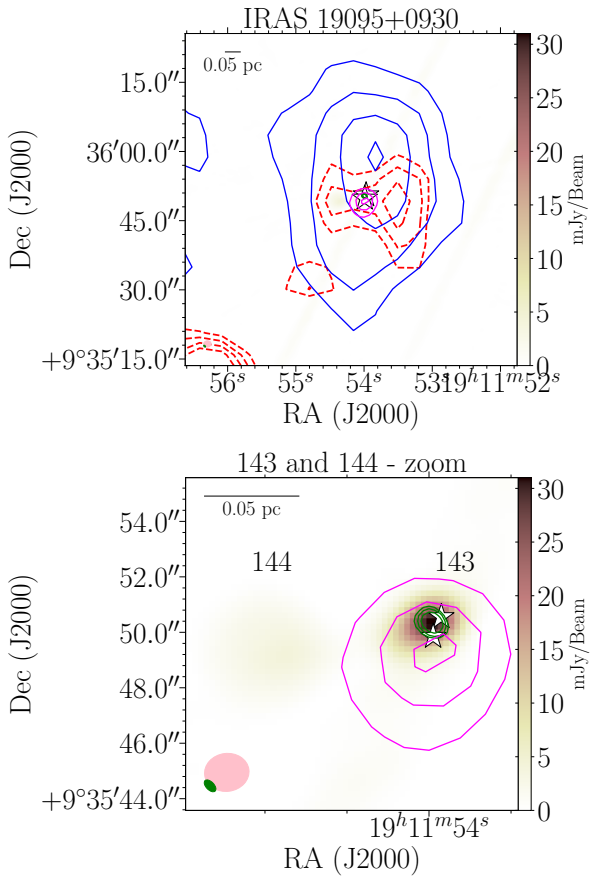

Fig. A.13. VLA *C*-band (6 cm) continuum emission map of radio sources 143 and 144 located in the region IRAS 19095+0930. A close-up view of the radio sources (143 and 144) is shown in the *bottom panel*. The green contour levels of the *K*-band (1.3 cm) continuum emission are 3, 5, and 9 times 2 mJy beam^{-1}. The blue- and redshifted outflow lobes of SiO (2−1) are shown as solid blue and dashed red contours, respectively (see Sánchez-Monge et al. 2013b). The magenta contours show the *Spitzer*/GLIMPSE 4.5 μm emission. The pink and green ellipses are the beam sizes of the *C* and *K* bands, respectively. The white and orange stars mark the of the H_2O and CH_3OH masers (see Table 2).

This region has been studied in the past by different authors at different wavelengths (Kurtz et al. 1994; Lekht 2000; De Buizer et al. 2005). De Buizer et al. (2005) reported a kidney-bean shape structure at mid-infrared wavelengths that matches the radio continuum sources reported by Kurtz et al. (1994) that were referred to as a H II region. The object is also associated with OH masers. We did not find this source in the EGO catalogs (Cyganowski et al. 2008, 2009), but we identified a 4.5 μm source associated with source 143. No 4.5 μm infrared source appears to be associated with the eastern source 144.

We derive a spectral index of $+1.12 \pm 0.04$ for source 143, which is consistent with thermal emission. Together with its location at the geometrical center of the outflow and its association with masers, this may suggest that source 143 is a good radio-jet candidate. However, the high radio continuum flux of this source does not appear to be consistent with the typical properties of other radio jets (see Figs. 3 and 5). This might mean that this source is in a transition phase from a radio jet to a H II region. However, this requires further investigation.

Appendix B: Catalog of the continuum sources

In the following tables and figures, we provide information on the properties of the radio continuum sources detected in the VLA observations presented in this work. In Table B.1 we list the coordinates of the 146 radio continuum sources together with their flux density, intensity peak, and deconvolved size at 6 cm (*C* band) and 1.3 cm (*K* band). The fluxes and intensities are corrected for the primary beam response of the VLA antennas. For sources outside the *C*-band primary beam (listed as "oC" in Col. 11 of Table B.1) the primary beam correction is not reliable and the flux has to be taken with caution. Similarly, for sources located outside the *K*-band primary beam (labeled "oK" in the table), the *K*-band flux has to be taken with caution. The last column of the table lists the spectral index, α. For sources with no reliable flux estimate at one of the bands, we did not determine the spectral index. For sources detected at both frequency bands (*C* and *K* bands), the spectral index was determined using the fluxes determined after creating images with a common *uv* range (see Sect. 3.2 for more details). In Table B.2 we list the observed and deconvolved source sizes of all the detected sources. The source sizes are determined as $\sqrt{\theta_{\rm major} \times \theta_{\rm minor}}$, where $\theta_{\rm major}$ and $\theta_{\rm minor}$ are listed in Table B.2. We transformed the angular size of each source into astronomical unit (au) using the distances listed in Table 1. We give the source size in Table B.1. Finally, in Table B.3, we list the intensities, flux densities, and sizes determined from the images generated using a common *uv* range at the *C* and *K* bands. In Figs. B.1–B.16, we present close-up views of the *C*- and *K*-band emission for the 146 detected continuum sources.

Table B.1. Catalog of radio continuum sources detected with the VLA.

		Coordinates		*C* band [(a)]			*K* band [(b)]				
ID	Region	RA(J2000) (h:m:s)	Dec(J2000) (°:′:″)	Intensity (mJy beam^{-1})	Flux (mJy)	Size (au)	Intensity (mJy beam^{-1})	Flux (mJy)	Size (au)		Spectral index [(c)]
1	IRAS 05358+3543	05:39:25.838	+35:45:53.861	37.733 ± 0.272	38.134 ± 0.272	<2200	–	–	–	iC/oK	–
2		05:39:13.064	+35:45:51.125	0.387 ± 0.010	0.534 ± 0.014	1300	–	–	–	iC/iK	–
3		05:39:10.056	+35:46:07.731	0.105 ± 0.003	0.075 ± 0.002	<1800	–	–	–	iC/iK	–
4		05:39:12.839	+35:45:50.854	0.147 ± 0.006	0.332 ± 0.015	2200	–	–	–	iC/iK	–
5		05:39:09.938	+35:45:17.196	0.267 ± 0.008	0.403 ± 0.013	1500	–	–	–	iC/iK	–
6		05:39:33.539	+35:48:03.740	0.282 ± 0.006	0.345 ± 0.007	1000	–	–	–	iC/oK	–
7		05:39:14.367	+35:44:29.634	0.191 ± 0.006	0.266 ± 0.009	1300	–	–	–	iC/iK	–
8		05:39:12.120	+35:44:02.155	0.238 ± 0.006	0.262 ± 0.007	500	–	–	–	iC/iK	–
9		05:38:54.931	+35:44:41.720	0.521 ± 0.004	0.571 ± 0.005	600	–	–	–	iC/oK	–
10		05:38:39.158	+35:49:43.533	0.886 ± 0.060	1.640 ± 0.110	2000	–	–	–	iC/oK	–
11		05:39:37.247	+35:46:45.155	0.265 ± 0.014	0.197 ± 0.010	<1900	–	–	–	iC/oK	–
12	G189.78+0.34	06:08:35.111	+20:39:12.570	0.429 ± 0.016	0.722 ± 0.027	1700	–	–	–	iC/iK	–
13		06:08:35.273	+20:39:09.010	0.874 ± 0.032	1.241 ± 0.046	1300	–	–	–	iC/iK	–
14		06:08:35.308	+20:39:06.771	0.372 ± 0.024	0.687 ± 0.045	1900	–	–	–	iC/iK	–
15		06:08:35.380	+20:39:04.423	0.313 ± 0.013	0.938 ± 0.040	2800	–	–	–	iC/iK	–
16		06:08:35.449	+20:39:03.118	0.503 ± 0.021	1.040 ± 0.044	2000	–	–	–	iC/iK	–
17		06:08:43.600	+20:41:08.591	0.183 ± 0.008	0.119 ± 0.005	<1700	–	–	–	iC/oK	–
18		06:08:45.199	+20:38:16.647	0.114 ± 0.008	0.164 ± 0.011	1300	–	–	–	iC/oK	–
19		06:08:36.598	+20:43:14.366	0.185 ± 0.015	0.300 ± 0.024	800	–	–	–	iC/oK	–
20		06:08:44.256	+20:33:06.465	0.595 ± 0.038	0.569 ± 0.036	<2000	–	–	–	iC/oK	–
21	G192.58−0.04	06:12:53.607	+18:00:26.360	12.029 ± 0.460	18.208 ± 0.701	2400	–	–	–	iC/iK	–
22		06:12:54.013	+17:59:23.202	3.998 ± 0.087	10.274 ± 0.220	4000	–	–	–	iC/iK	–
23		06:12:53.842	+17:59:22.168	1.540 ± 0.047	1.558 ± 0.047	<3300	–	–	–	iC/iK	–
24		06:12:54.299	+17:59:33.802	0.637 ± 0.033	0.494 ± 0.025	<2900	–	–	–	iC/iK	–
25		06:12:54.335	+17:59:24.274	0.303 ± 0.011	0.470 ± 0.049	5800	–	–	–	iC/iK	–
26		06:12:49.910	+18:03:05.366	0.313 ± 0.009	0.408 ± 0.012	1500	–	–	–	iC/oK	–
27	G18.18−0.30	18:25:01.066	−13:15:39.515	4.240 ± 0.262	21.202 ± 1.367	6600	…	…	…	iC/oK	…
28		18:25:07.460	−13:17:58.837	2.412 ± 0.089	3.863 ± 0.144	2200	…	…	…	iC/oK	…
29		18:25:06.979	−13:18:10.638	1.745 ± 0.034	3.390 ± 0.069	3000	…	…	…	iC/oK	…
30		18:25:01.186	−13:15:45.881	1.303 ± 0.020	1.989 ± 0.032	2400	…	…	…	iC/oK	…
31		18:25:00.956	−13:15:35.726	1.298 ± 0.039	6.719 ± 0.204	7000	…	…	…	iC/oK	…
32		18:24:44.852	−13:14:45.806	2.647 ± 0.036	4.447 ± 0.064	2400	…	…	…	iC/oK	…
33		18:24:53.825	−13:12:52.490	0.713 ± 0.007	0.670 ± 0.007	<3400	…	…	…	iC/oK	…
34		18:25:06.706	−13:12:28.027	0.307 ± 0.008	0.331 ± 0.009	<3600	…	…	…	iC/oK	…
35		18:25:42.356	−13:10:21.217	0.361 ± 0.023	1.177 ± 0.075	4500	…	…	…	oC	…
36		18:25:18.546	−13:15:33.062	0.182 ± 0.006	0.259 ± 0.009	2100	…	…	…	iC/oK	…
37		18:24:55.788	−13:10:16.391	0.404 ± 0.023	1.782 ± 0.101	6400	…	…	…	iC/oK	…
38		18:24:55.941	−13:10:17.447	0.291 ± 0.012	1.226 ± 0.053	6100	…	…	…	iC/oK	…
39	IRAS 18223−1243	18:25:31.473	−12:41:24.031	54.190 ± 1.078	105.645 ± 2.077	4500	…	…	…	iC/oK	…
40		18:25:04.143	−12:37:44.910	48.631 ± 1.238	75.337 ± 1.932	3800	…	…	…	iC/oK	…
41		18:25:26.731	−12:40:33.237	1.694 ± 0.063	2.477 ± 0.094	3600	…	…	…	iC/oK	…
42		18:24:52.605	−12:39:19.804	2.989 ± 0.054	4.158 ± 0.075	2900	…	…	…	iC/oK	…
43		18:24:36.306	−12:51:03.315	1.762 ± 0.091	6.550 ± 0.340	8800	…	…	…	oC	…
44		18:24:34.617	−12:52:03.911	0.374 ± 0.016	1.583 ± 0.069	9600	…	…	…	oC	…
45		18:26:04.962	−12:34:35.177	0.250 ± 0.009	0.577 ± 0.023	6000	…	…	…	oC	…
46		18:26:05.248	−12:34:35.621	0.289 ± 0.039	0.579 ± 0.039	<8200	…	…	…	oC	…
47		18:24:34.692	−12:50:59.457	0.771 ± 0.083	1.542 ± 0.083	<16800	…	…	…	oC	…

Notes. [(a)]Flux density, intensity peak and deconvolved source size for the sources detected at 6 cm in the *C* band images. The fluxes are corrected by the primary beam response of the antennas, except for sources located outside the primary beam (listed as "oC"). Source sizes are calculated as indicated in Appendix B and based on the values reported in Table B.2. Upper limits in the source size indicate that the source could not be deconvolved (see more details in Table B.2). [(b)]Flux density, intensity peak and deconvolved source size for the sources detected at 1.3 cm in the *K* band images. The fluxes are corrected by the primary beam response of the antennas, except for sources located outside the primary beam (listed either as "iC/oK" or "oC", see Sect. 3.1 for more details about this classification). [(c)]Spectral index determined from the fluxes at 6 cm (*C* band) and 1.3 cm (*K* band). For the sources detected in one band, we use a 5σ upper limit for the non-detected band flux. Only for sources located with the primary beam of both images (sources listed as "iC/iK") we can derive reliable fluxes and therefore spectral indices. Sources marked with [†] have been re-imaged using the common *uv*-range (see Table B.3). More accurate spectral indices, derived using these new images, are listed in Table 3.

Table B.1. continued.

		Coordinates		*C* band [(a)]			*K* band [(b)]				
ID	Region	RA(J2000) (h:m:s)	Dec(J2000) (°:′:″)	Intensity (mJy beam^{-1})	Flux (mJy)	Size (au)	Intensity (mJy beam^{-1})	Flux (mJy)	Size (au)		Spectral index [(c)]
48a	IRAS 18228−1312	18:25:41.925	−13:10:17.630	21.200 ± 0.450	219.960 ± 5.101	13500	6.992 ± 0.835	13.782 ± 2.314	<7500	iC/iK	−2.11 ± 0.13[†]
48b		18:25:42.059	−13:10:16.545	19.373 ± 0.720	383.051 ± 9.900	19100	6.218 ± 1.203	14.341 ± 3.711	5400	iC/iK	−2.51 ± 0.20[†]
48c		18:25:42.407	−13:10:22.149	38.507 ± 2.700	297.053 ± 9.900	11200	25.098 ± 1.807	64.552 ± 6.425	6500	iC/iK	−1.17 ± 0.10[†]
49		18:26:26.274	−13:05:48.537	0.468 ± 0.010	0.445 ± 0.009	<4300	…	…	…	oC	…
50		18:25:00.730	−13:15:35.808	0.312 ± 0.019	13.170 ± 0.800	28300	…	…	…	oC	…
51	G19.27+0.1M1	18:27:37.962	−11:56:33.896	0.348 ± 0.023	2.140 ± 0.140	8200	…	…	…	oC	…
52		18:26:20.973	−12:05:33.129	0.797 ± 0.033	0.878 ± 0.037	1100	…	…	…	iC/oK	…
53		18:26:03.677	−12:04:37.085	1.130 ± 0.019	1.198 ± 0.020	800	…	…	…	iC/iK	<−0.57
54		18:25:45.520	−12:05:18.590	0.265 ± 0.005	0.326 ± 0.007	1400	…	…	…	iC/oK	…
55		18:25:54.272	−11:52:19.022	0.186 ± 0.012	1.138 ± 0.071	3600	…	…	…	oC	…
56		18:26:04.228	−11:52:32.053	0.299 ± 0.041	7.300 ± 1.000	17600	…	…	…	oC	…
57		18:26:48.638	−12:26:17.050	0.199 ± 0.009	0.599 ± 0.030	5000	…	…	…	oC	…
58		18:26:34.300	−11:57:59.910	0.284 ± 0.008	0.518 ± 0.016	3100	…	…	…	oC	…
59		18:26:13.780	−12:01:19.596	0.258 ± 0.007	0.249 ± 0.006	<3500	…	…	…	iC/oK	…
60		18:27:37.166	−11:56:26.273	0.168 ± 0.008	0.409 ± 0.021	2200	…	…	…	oC	…
61		18:26:05.577	−12:04:33.534	0.123 ± 0.003	0.139 ± 0.003	4300	…	…	…	iC/iK	<+2.07
62		18:25:51.964	−12:05:13.440	…	…	…	0.203 ± 0.006	0.244 ± 0.092	<1100	iC/iK	>+1.23
63	IRAS 18236−1205	18:26:25.064	−12:03:48.923	0.070 ± 0.004	0.099 ± 0.006	<1100	0.281 ± 0.010	0.140 ± 0.010	2800	iC/iK	+0.26 ± 0.21[†]
64		18:26:25.782	−12:03:53.203	0.331 ± 0.013	0.383 ± 0.015	<4300	0.182 ± 0.006	0.280 ± 0.010	930	iC/iK	−0.24 ± 0.12[†]
65		18:26:26.380	−12:04:19.782	0.558 ± 0.004	0.570 ± 0.004	<4000	1.774 ± 0.004	1.960 ± 0.006	310	iC/iK	+0.94 ± 0.02[†]
66		18:26:35.471	−12:01:13.807	0.125 ± 0.002	0.113 ± 0.002	<3800	…	…	…	iC/oK	…
67		18:26:22.554	−12:05:58.888	0.224 ± 0.035	0.708 ± 0.060	<7400	…	…	…	iC/oK	…
68		18:26:22.308	−12:05:58.065	0.135 ± 0.005	0.270 ± 0.020	<6000	…	…	…	iC/oK	…
69		18:26:22.051	−12:07:28.996	0.092 ± 0.003	0.449 ± 0.034	<9700	…	…	…	iC/oK	…
70		18:26:21.849	−12:07:31.842	0.070 ± 0.001	0.143 ± 0.019	<4300	…	…	…	iC/oK	…
71		18:26:21:659	−12:07:35.409	0.198 ± 0.001	0.394 ± 0.031	<6500	…	…	…	iC/oK	…
72	G23.60+0.0M1	18:33:53.474	−08:07:12.198	0.817 ± 0.110	9.900 ± 1.300	11900	…	…	…	oC	…
73		18:34:12.339	−08:19:01.195	0.191 ± 0.003	0.190 ± 0.003	<3600	0.357 ± 0.042	0.480 ± 0.054	<1200	iC/iK	+0.70 ± 0.26[†]
74		18:34:11.574	−08:19:06.420	0.310 ± 0.004	0.328 ± 0.004	<3700	0.109 ± 0.045	1.040 ± 0.430	1100	iC/iK	+0.87 ± 0.94[†]
75		18:34:21.063	−08:18:12.357	0.420 ± 0.006	0.452 ± 0.006	800	…	…	…	iC/oK	…
76		18:34:33.022	−08:15:26.757	11.325 ± 0.194	12.813 ± 0.219	1200	…	…	…	iC/oK	…
77		18:34:44.839	−08:31:05.331	0.210 ± 0.003	0.272 ± 0.003	1700	…	…	…	oC	…
78		18:33:44.014	−08:21:22.952	1.234 ± 0.038	2.500 ± 0.077	3500	…	…	…	iC/oK	…
79		18:33:47.803	−08:23:34.272	0.763 ± 0.049	1.718 ± 0.109	3900	…	…	…	iC/oK	…
80		18:34:06.126	−08:24:38.779	0.276 ± 0.012	0.336 ± 0.015	<3900	…	…	…	iC/oK	…
81		18:34:17.741	−08:21:08.236	0.096 ± 0.004	0.119 ± 0.005	<4000	…	…	…	iC/oK	…
82		18:34:14.297	−08:24:10.308	0.351 ± 0.010	0.390 ± 0.011	<3800	…	…	…	iC/oK	…
83	IRAS 18316−0602	18:34:20.904	−05:59:41.968	2.275 ± 0.081	3.345 ± 0.120	2500	0.606 ± 0.062	2.621 ± 0.259	2000	iC/iK	−0.19 ± 0.24[†]
84		18:34:33.930	−06:02:21.993	1.618 ± 0.025	1.863 ± 0.029	1200	…	…	…	iC/oK	…
85		18:34:27.632	−06:05:09.136	2.103 ± 0.026	2.493 ± 0.030	1300	…	…	…	iC/oK	…
86		18:34:14.921	−06:00:23.582	0.313 ± 0.005	0.354 ± 0.006	<4400	…	…	…	iC/iK	<+1.43
87		18:34:26.746	−05:57:21.183	0.907 ± 0.016	0.998 ± 0.019	<4400	…	…	…	iC/oK	…
88		18:34:16.533	−05:45:48.502	0.109 ± 0.006	0.742 ± 0.045	9900	…	…	…	oC	…
89		18:32:42.034	−06:10:19.838	0.146 ± 0.011	0.301 ± 0.022	3700	…	…	…	oC	…
90		18:34:08.906	−05:52:55.202	1.454 ± 0.064	1.658 ± 0.073	<4500	…	…	…	iC/oK	…
91		18:34:32.327	−06:00:15.075	0.130 ± 0.007	0.147 ± 0.008	<4400	…	…	…	iC/oK	…
92		18:34:13.821	−05:53:01.189	0.405 ± 0.013	0.971 ± 0.031	3400	…	…	…	iC/oK	…
93		18:35:10.900	−06:02:32.533	0.067 ± 0.001	0.136 ± 0.008	4000	…	…	…	oC	…
94		18:34:17.698	−06:05:05.398	…	…	…	0.222 ± 0.006	0.311 ± 0.009	2100	iC/oK	…
95		18:34:20.819	−05:59:42.997	…	…	…	0.227 ± 0.037	0.251 ± 0.069	<1300	iC/iK	>+1.36
96	G24.08+0.0M2	18:34:48.710	−07:46:41.510	16.982 ± 0.338	21.761 ± 0.433	1600	4.098 ± 0.166	5.300 ± 0.212	<1100	iC/iK	−1.08 ± 0.10[†]
97		18:34:41.391	−07:43:55.450	7.986 ± 0.172	10.670 ± 0.239	1600	…	…	…	iC/oK	…
98		18:34:41.452	−07:43:47.693	1.411 ± 0.017	2.558 ± 0.032	3000	…	…	…	iC/oK	…
99		18:34:57.182	−07:43:26.184	3.122 ± 0.052	4.364 ± 0.073	2000	…	…	…	iC/oK	…
100		18:34:59.593	−07:43:00.526	3.762 ± 0.104	7.750 ± 0.217	3500	…	…	…	iC/oK	…
101		18:34:59.600	−07:42:57.062	1.208 ± 0.021	2.517 ± 0.089	2800	…	…	…	iC/oK	…

Table B.1. continued.

		Coordinates		*C* band[(a)]			*K* band[(b)]				
ID	Region	RA(J2000) (h:m:s)	Dec(J2000) (°:′:″)	Intensity (mJy beam^{-1})	Flux (mJy)	Size (au)	Intensity (mJy beam^{-1})	Flux (mJy)	Size (au)		Spectral index[(c)]
102		18:34:57.132	−07:45:22.485	1.141 ± 0.014	1.454 ± 0.017	1700	…	…	…	iC/iK	<−0.06
103		18:34:12.138	−07:52:54.065	0.136 ± 0.004	0.202 ± 0.005	2400	…	…	…	oC	…
104		18:34:11.271	−07:53:07.879	0.088 ± 0.004	0.146 ± 0.006	2800	…	…	…	oC	…
105		18:33:59.500	−07:52:36.635	0.304 ± 0.005	0.608 ± 0.056	<7600	…	…	…	oC	…
106		18:34:25.403	−07:54:46.135	0.239 ± 0.074	59.000 ± 18.00	55700	…	…	…	oC	…
107		18:34:51.288	−07:42:14.421	0.094 ± 0.005	0.195 ± 0.033	<2900	…	…	…	iC/oK	…
108		18:35:23.922	−07:37:38.200	1.510 ± 0.150	2.080 ± 0.020	<3500	…	…	…	oC	…
109		18:34:52.966	−07:47:03.052	0.041 ± 0.003	0.082 ± 0.032	<2300	…	…	…	iC/iK	<+2.33
110	G24.33+0.1M1	18:35:08.132	−07:35:04.176	0.438 ± 0.007	0.434 ± 0.007	<5400	0.769 ± 0.029	0.905 ± 0.034	<1600	iC/iK	+0.55 ± 0.09[†]
111		18:35:13.569	−07:38:20.379	0.382 ± 0.014	0.659 ± 0.024	2700	…	…	…	iC/oK	…
112		18:35:33.971	−07:37:34.491	1.630 ± 0.078	4.685 ± 0.228	7400	…	…	…	iC/oK	…
113		18:35:10.888	−07:34:22.080	0.198 ± 0.007	0.278 ± 0.011	3200	…	…	…	iC/iK	< +0.07
114		18:35:02.821	−07:31:20.729	0.290 ± 0.005	0.328 ± 0.005	2000	…	…	…	iC/oK	…
115		18:34:48.656	−07:46:40.369	0.151 ± 0.006	0.225 ± 0.009	3700	…	…	…	oC	…
116		18:35:56.006	−07:27:23.278	0.196 ± 0.009	0.289 ± 0.015	2400	…	…	…	oC	…
117	G24.60+0.1M1	18:36:12.517	−07:12:09.922	0.437 ± 0.015	0.526 ± 0.018	1300	…	…	…	oC	…
118		18:36:12.607	−07:12:14.144	0.420 ± 0.022	0.983 ± 0.052	5700	…	…	…	oC	…
119		18:35:40.677	−07:22:05.797	0.305 ± 0.016	1.107 ± 0.059	8400	…	…	…	iC/oK	…
120		18:35:40.739	−07:22:00.863	0.284 ± 0.009	0.457 ± 0.014	3000	…	…	…	iC/oK	…
121		18:35:40.869	−07:21:57.887	0.286 ± 0.020	1.705 ± 0.126	10900	…	…	…	iC/oK	…
122		18:36:05.589	−07:31:21.640	0.349 ± 0.036	3.790 ± 0.390	16200	…	…	…	oC	…
123		18:35:53.123	−07:14:20.492	1.058 ± 0.011	1.164 ± 0.012	<5500	…	…	…	iC/oK	…
124		18:35:16.807	−07:05:08.357	0.239 ± 0.011	0.400 ± 0.019	3800	…	…	…	oC	…
125		18:35:41.070	−07:16:41.062	0.140 ± 0.004	0.123 ± 0.004	<4900	…	…	…	iC/iK	…
126		18:35:43.769	−07:19:26.186	0.114 ± 0.003	0.105 ± 0.002	<5000	…	…	…	iC/iK	<+0.96
127		18:35:03.755	−07:26:00.913	0.146 ± 0.012	0.529 ± 0.044	8400	…	…	…	oC	…
128		18:36:18.116	−07:08:50.104	0.128 ± 0.003	0.705 ± 0.018	11000	…	…	…	oC	…
129		18:35:40.400	−07:19:28.740	0.088 ± 0.005	0.157 ± 0.009	4500	…	…	…	iC/iK	<+0.18
130		18:34:59.859	−07:26:39.367	0.078 ± 0.002	0.110 ± 0.003	3000	…	…	…	oC	…
131		18:34:39.433	−07:02:39.152	0.068 ± 0.002	0.081 ± 0.003	<5700	…	…	…	oC	…
132	G24.60+0.1M2	18:35:47.199	−07:12:59.443	0.300 ± 0.008	0.543 ± 0.015	3800	…	…	…	iC/oK	…
133		18:35:40.955	−07:21:56.177	0.275 ± 0.010	0.992 ± 0.036	7600	…	…	…	iC/oK	…
134		18:35:56.070	−07:27:23.872	0.133 ± 0.015	0.243 ± 0.028	<6500	…	…	…	oC	…
135		18:35:29.951	−07:27:46.840	0.064 ± 0.003	0.077 ± 0.003	1900	…	…	…	oC	…
136		18:35:40.124	−07:18:37.396	…	…	…	0.821 ± 0.110	0.853 ± 0.116	<2100	iC/iK	>+1.67
137	G34.43+0.2M3	18:53:18.845	+01:14:59.320	4.070 ± 0.280	18.400 ± 1.300	7000	0.242 ± 0.022	1.270 ± 0.120	2000	oC	…
138		18:53:18.672	+01:24:47.737	6.046 ± 0.080	7.393 ± 0.097	1600	…	…	…	iC/oK	…
139		18:53:18.020	+01:25:25.608	0.439 ± 0.017	0.729 ± 0.029	2100	…	…	…	iC/oK	…
140		18:53:08.320	+01:29:33.994	0.858 ± 0.013	0.820 ± 0.012	3000	…	…	…	iC/oK	…
141		18:53:35.990	+01:35:18.770	2.290 ± 0.147	10.435 ± 0.672	<5600	…	…	…	iC/oK	…
142		18:54:14.014	+01:19:18.429	0.089 ± 0.003	0.148 ± 0.005	7100	…	…	…	oC	…
143	IRAS 19095+0930	19:11:53.997	+09:35:50.404	30.580 ± 0.860	40.400 ± 1.100	1900	90.545 ± 2.101	126.364 ± 3.001	660	iC/iK	+0.87 ± 0.08[†]
144		19:11:54.369	+09:35:49.254	4.211 ± 0.240	15.565 ± 0.890	7300	…	…	…	iC/iK	<−2.97
145		19:12:00.546	+09:36:24.232	2.847 ± 0.023	2.838 ± 0.023	<4400	…	…	…	iC/iK	<+0.32
146		19:11:46.436	+09:37:03.679	1.927 ± 0.025	2.048 ± 0.027	<4500	…	…	…	iC/oK	…

Table B.2. Observed and deconvolved angular sizes for the radio continuum sources (see Table B.1).

		Observed source size			Deconvolved diameter		
ID	Region	Major axis (″)	Minor axis (″)	PA (°)	Major axis (″)	Minor axis (″)	PA (°)
Observed and deconvolved source sizes for *C* band detections							
1	IRAS 05358+3543	1.269 ± 0.009	1.239 ± 0.009	53.0 ± 3.8	…	…	…
2		1.532 ± 0.034	1.402 ± 0.034	106.7 ± 3.4	0.894 ± 0.063	0.633 ± 0.085	114.9 ± 9.9
3		1.113 ± 0.044	1.001 ± 0.043	155.4 ± 5.2	…	…	…
4		2.411 ± 0.058	1.455 ± 0.057	120.4 ± 1.1	2.069 ± 0.069	0.730 ± 0.124	121.1 ± 1.2
5		1.667 ± 0.041	1.409 ± 0.041	104.5 ± 2.0	1.105 ± 0.065	0.654 ± 0.098	108.5 ± 3.8
6		1.412 ± 0.028	1.349 ± 0.027	0.1 ± 7.5	0.690 ± 0.066	0.472 ± 0.094	169.0 ± 9.0
7		1.520 ± 0.046	1.424 ± 0.044	145.4 ± 6.4	0.899 ± 0.082	0.644 ± 0.106	147.1 ± 6.4
8		1.330 ± 0.035	1.286 ± 0.034	168.0 ± 9.0	0.512 ± 0.758	0.215 ± 1.011	160.0 ± 9.0
9		1.357 ± 0.012	1.255 ± 0.012	76.4 ± 1.4	0.490 ± 0.035	0.249 ± 0.076	85.0 ± 9.0
10		1.918 ± 0.083	1.502 ± 0.086	65.3 ± 3.1	1.440 ± 0.110	0.870 ± 0.160	65.6 ± 3.8
11		1.089 ± 0.070	1.065 ± 0.068	135.0 ± 9.0	…	…	…
12	G189.78+0.34	1.673 ± 0.041	1.397 ± 0.048	12.0 ± 2.2	1.095 ± 0.070	0.860 ± 0.089	0.5 ± 9.6
13		1.578 ± 0.041	1.249 ± 0.048	14.6 ± 1.8	0.934 ± 0.074	0.602 ± 0.115	6.7 ± 9.5
14		1.781 ± 0.072	1.441 ± 0.083	10.1 ± 3.9	1.250 ± 0.110	0.930 ± 0.150	1.7 ± 9.4
15		2.461 ± 0.073	1.688 ± 0.050	158.3 ± 2.0	2.161 ± 0.088	1.194 ± 0.079	154.2 ± 2.7
16		1.920 ± 0.050	1.493 ± 0.050	156.9 ± 1.8	1.525 ± 0.068	0.880 ± 0.096	148.3 ± 3.9
17		1.014 ± 0.052	0.892 ± 0.061	18.6 ± 6.4	…	…	…
18		1.598 ± 0.078	1.254 ± 0.092	21.7 ± 4.9	0.958 ± 0.136	0.629 ± 0.226	20.0 ± 9.0
19		1.959 ± 0.091	1.148 ± 0.100	174.7 ± 2.0	1.524 ± 0.091	0.136 ± 0.100	169.9 ± 2.0
20		1.382 ± 0.071	0.961 ± 0.083	16.5 ± 2.4	…	…	…
21	G192.58−0.04	1.741 ± 0.046	1.451 ± 0.054	25.8 ± 2.2	1.033 ± 0.082	0.827 ± 0.106	32.0 ± 9.0
22		2.524 ± 0.064	1.700 ± 0.029	59.1 ± 1.5	2.152 ± 0.078	1.116 ± 0.052	63.7 ± 2.1
23		1.454 ± 0.036	1.162 ± 0.043	30.3 ± 1.8	…	…	…
24		1.206 ± 0.066	1.073 ± 0.072	170.4 ± 6.4	…	…	…
25		2.903 ± 0.050	2.375 ± 0.038	148.1 ± 2.4	2.614 ± 0.060	1.961 ± 0.052	143.0 ± 3.1
26		1.745 ± 0.050	1.247 ± 0.042	28.1 ± 1.9	1.043 ± 0.064	0.360 ± 0.221	32.0 ± 4.4
27	G18.18−0.30	3.480 ± 0.102	2.620 ± 0.077	47.0 ± 1.4	3.270 ± 0.110	2.030 ± 0.110	53.9 ± 2.4
28		1.884 ± 0.040	1.550 ± 0.064	174.8 ± 2.4	1.180 ± 0.098	0.657 ± 0.172	61.0 ± 9.0
29		2.210 ± 0.025	1.604 ± 0.033	11.5 ± 0.8	1.629 ± 0.042	0.820 ± 0.085	37.9 ± 3.1
30		1.962 ± 0.017	1.419 ± 0.028	165.8 ± 0.8	0.971 ± 0.050	0.890 ± 0.053	50.0 ± 9.0
31		3.244 ± 0.057	2.909 ± 0.052	151.8 ± 4.5	2.803 ± 0.090	2.645 ± 0.091	117.0 ± 9.0
32		1.926 ± 0.016	1.591 ± 0.024	179.5 ± 0.7	1.267 ± 0.034	0.711 ± 0.058	57.4 ± 3.7
33		1.637 ± 0.011	1.047 ± 0.019	166.6 ± 0.3	…	…	…
34		1.714 ± 0.030	1.148 ± 0.049	161.5 ± 1.0	…	…	…
35		2.876 ± 0.108	2.066 ± 0.072	56.7 ± 1.5	2.660 ± 0.120	1.160 ± 0.140	62.3 ± 2.0
36		2.114 ± 0.037	1.225 ± 0.061	157.9 ± 1.0	1.224 ± 0.073	0.584 ± 0.164	147.5 ± 6.1
37		3.407 ± 0.061	2.362 ± 0.099	156.2 ± 1.4	2.938 ± 0.074	2.105 ± 0.117	152.7 ± 3.1
38		3.376 ± 0.103	2.275 ± 0.068	132.8 ± 1.9	3.000 ± 0.130	1.850 ± 0.110	123.8 ± 3.9
39	IRAS 18223−1243	2.267 ± 0.027	1.865 ± 0.034	18.1 ± 0.8	1.715 ± 0.043	0.882 ± 0.088	54.0 ± 3.4
40		2.167 ± 0.030	1.550 ± 0.048	172.3 ± 0.7	1.163 ± 0.073	0.920 ± 0.096	33.0 ± 9.0
41		2.230 ± 0.044	1.423 ± 0.072	166.4 ± 1.0	1.178 ± 0.085	0.844 ± 0.132	168.0 ± 9.0
42		2.064 ± 0.021	1.461 ± 0.034	175.2 ± 0.5	1.053 ± 0.055	0.622 ± 0.099	41.7 ± 7.7
43		3.002 ± 0.060	2.684 ± 0.098	161.3 ± 2.7	2.440 ± 0.120	2.320 ± 0.100	91.0 ± 9.0
44		3.271 ± 0.056	2.803 ± 0.078	142.1 ± 1.7	2.810 ± 0.081	2.401 ± 0.104	116.0 ± 9.0
45		2.538 ± 0.046	1.970 ± 0.075	158.5 ± 1.5	1.748 ± 0.088	1.538 ± 0.113	129.0 ± 9.0
46		2.548 ± 1.973	1.973 ± 0.091	157.0 ± 7.0	…	…	…
47		5.050 ± 0.250	4.120 ± 0.200	143.0 ± 9.0	…	…	…
48a	IRAS 18228−1312	6.450 ± 0.144	3.501 ± 0.070	4.3 ± 1.2	6.189 ± 0.153	3.268 ± 0.080	5.7 ± 1.5
48b		7.250 ± 0.270	5.940 ± 0.220	46.1 ± 7.4	7.120 ± 0.290	5.670 ± 0.250	49.0 ± 8.0
48c		4.610 ± 0.340	3.640 ± 0.250	65.0 ± 9.0	4.450 ± 0.370	3.130 ± 0.320	67.0 ± 9.0
49		1.784 ± 0.025	1.160 ± 0.040	163.8 ± 0.7	…	…	…
50		11.100 ± 0.080	8.271 ± 0.107	140.4 ± 0.5	10.960 ± 0.082	8.164 ± 0.109	139.5 ± 0.6
51	G19.27+0.1M1	4.790 ± 0.110	2.980 ± 0.130	167.3 ± 1.7	4.380 ± 0.120	2.730 ± 0.150	167.9 ± 2.2
52		2.071 ± 0.050	1.231 ± 0.082	163.8 ± 1.7	0.694 ± 1.257	0.317 ± 0.872	161.0 ± 9.0
53		2.018 ± 0.021	1.218 ± 0.034	164.9 ± 0.7	0.518 ± 1.433	0.258 ± 0.931	173.0 ± 9.0

Table B.2. continued.

ID	Region	Observed source size			Deconvolved diameter		
		Major axis (″)	Minor axis (″)	PA (°)	Major axis (″)	Minor axis (″)	PA (°)
54		2.060 ± 0.028	1.387 ± 0.042	171.9 ± 1.3	0.889 ± 1.063	0.391 ± 0.797	36.0 ± 9.0
55		4.480 ± 0.140	3.170 ± 0.110	95.3 ± 2.9	4.290 ± 0.150	0.550 ± 0.150	91.0 ± 9.0
56		8.700 ± 0.260	6.540 ± 0.260	100.9 ± 4.2	8.590 ± 0.280	6.280 ± 0.280	99.3 ± 4.4
57		3.057 ± 0.094	2.282 ± 0.092	141.4 ± 3.5	2.480 ± 0.140	1.780 ± 0.170	124.0 ± 9.0
58		2.447 ± 0.037	1.724 ± 0.059	175.3 ± 1.3	1.571 ± 0.077	1.125 ± 0.116	19.6 ± 9.9
59		1.951 ± 0.033	1.147 ± 0.053	159.8 ± 1.2	…	…	…
60		2.300 ± 0.140	1.430 ± 0.120	170.1 ± 3.6	1.250 ± 0.310	0.730 ± 0.480	4.2 ± 9.8
61		2.950 ± 0.100	1.900 ± 0.100	152.8 ± 2.5	2.250 ± 0.150	1.430 ± 0.170	143.8 ± 8.4
63	IRAS 18236−1205	0.485 ± 0.019	0.393 ± 0.021	134.6 ± 7.2	…	…	…
64		2.229 ± 0.061	1.148 ± 0.079	170.1 ± 1.5	…	…	…
65		2.033 ± 0.012	1.112 ± 0.017	163.6 ± 0.3	…	…	…
66		1.785 ± 0.044	1.121 ± 0.042	156.1 ± 1.6	…	…	…
67		4.068 ± 1.886	1.886 ± 0.093	116.0 ± 2.0	…	…	…
68		2.633 ± 0.156	1.893 ± 0.092	138.0 ± 6.0	…	…	…
69		6.040 ± 0.820	2.180 ± 0.210	3.0 ± 3.0	…	…	…
70		1.840 ± 0.170	1.400 ± 0.100	126.0 ± 9.0	…	…	…
71		3.193 ± 0.223	1.823 ± 0.093	159.0 ± 4.0	…	…	…
72	G23.60+0.0M1	5.110 ± 0.210	4.960 ± 0.210	114.0 ± 9.0	4.930 ± 0.290	4.660 ± 0.300	86.0 ± 9.0
73		1.770 ± 0.029	1.175 ± 0.035	160.1 ± 1.4	…	…	…
74		1.793 ± 0.021	1.236 ± 0.025	160.3 ± 1.0	…	…	…
75		1.884 ± 0.020	1.198 ± 0.026	156.3 ± 0.8	0.444 ± 1.410	0.290 ± 0.842	105.0 ± 9.0
76		1.926 ± 0.019	1.230 ± 0.032	157.3 ± 0.8	0.541 ± 0.083	0.475 ± 0.117	141.0 ± 9.0
77		1.975 ± 0.017	1.372 ± 0.027	162.3 ± 0.9	0.847 ± 0.061	0.602 ± 0.087	35.0 ± 9.0
78		2.285 ± 0.041	1.856 ± 0.057	152.2 ± 3.1	1.497 ± 0.095	1.312 ± 0.111	88.0 ± 9.0
79		2.672 ± 0.090	1.760 ± 0.116	174.9 ± 2.6	2.010 ± 0.140	1.220 ± 0.220	8.9 ± 9.8
80		1.817 ± 0.065	1.405 ± 0.084	173.7 ± 4.9	…	…	…
81		1.828 ± 0.051	1.418 ± 0.080	169.0 ± 4.0	…	…	…
82		1.762 ± 0.033	1.324 ± 0.054	152.6 ± 2.3	…	…	…
83	IRAS 18316−0602	1.987 ± 0.041	1.376 ± 0.060	174.1 ± 1.9	1.181 ± 0.096	0.592 ± 0.228	22.5 ± 9.8
84		1.741 ± 0.018	1.230 ± 0.028	163.2 ± 1.1	0.620 ± 1.085	0.251 ± 0.838	46.0 ± 9.0
85		1.759 ± 0.014	1.253 ± 0.021	165.1 ± 0.9	0.696 ± 0.053	0.283 ± 0.184	41.5 ± 7.6
86		1.683 ± 0.021	1.250 ± 0.031	163.2 ± 1.7	…	…	…
87		1.685 ± 0.021	1.215 ± 0.032	159.8 ± 1.4	…	…	…
88		4.688 ± 0.090	2.687 ± 0.094	13.0 ± 1.1	4.434 ± 0.099	2.333 ± 0.117	16.2 ± 1.5
89		2.250 ± 0.100	1.690 ± 0.110	118.4 ± 4.7	1.790 ± 0.160	0.800 ± 0.400	98.0 ± 9.0
90		1.709 ± 0.050	1.240 ± 0.074	145.2 ± 3.2	…	…	…
91		1.521 ± 0.081	1.376 ± 0.099	172.0 ± 9.0	…	…	…
92		2.140 ± 0.110	1.500 ± 0.110	145.9 ± 4.7	1.380 ± 0.230	0.910 ± 0.330	124.0 ± 9.0
93		2.474 ± 0.119	1.509 ± 0.075	173.9 ± 2.4	1.840 ± 0.180	0.950 ± 0.170	4.0 ± 7.9
96	G24.08+0.0M2	1.977 ± 0.023	1.317 ± 0.036	150.6 ± 1.0	0.942 ± 0.068	0.487 ± 0.151	118.6 ± 8.7
97		1.935 ± 0.026	1.402 ± 0.039	171.8 ± 1.5	1.008 ± 0.078	0.418 ± 0.265	37.1 ± 7.8
98		2.469 ± 0.022	1.492 ± 0.022	174.4 ± 0.6	1.759 ± 0.035	0.842 ± 0.052	6.8 ± 1.8
99		1.940 ± 0.019	1.464 ± 0.030	161.5 ± 1.2	0.942 ± 0.054	0.708 ± 0.068	59.0 ± 9.0
100		2.967 ± 0.039	1.410 ± 0.050	159.1 ± 0.7	2.357 ± 0.050	0.846 ± 0.086	159.1 ± 1.0
101		2.471 ± 0.101	1.714 ± 0.054	22.8 ± 3.0	2.020 ± 0.140	0.660 ± 0.280	39.1 ± 5.2
102		1.907 ± 0.016	1.358 ± 0.022	161.6 ± 0.9	0.776 ± 0.049	0.599 ± 0.070	50.0 ± 9.0
103		2.146 ± 0.049	1.399 ± 0.053	153.8 ± 1.7	1.190 ± 0.100	0.790 ± 0.130	140.0 ± 9.0
104		2.180 ± 0.150	1.540 ± 0.110	159.7 ± 5.7	1.230 ± 0.270	1.050 ± 0.270	162.0 ± 9.0
105		3.350 ± 0.270	2.830 ± 0.210	162.0 ± 9.0	…	…	…
106		26.310 ± 1.400	19.000 ± 0.530	69.7 ± 4.3	26.280 ± 1.400	18.910 ± 0.540	69.7 ± 4.3
107		1.369 ± 0.138	1.020 ± 0.072	160.0 ± 9.6	…	…	…
108		1.540 ± 1.289	1.289 ± 0.069	10.0 ± 9.1	…	…	…
109		0.940 ± 0.130	0.940 ± 0.130	168.0 ± 7.7	…	…	…
110	G24.33+0.1M1	1.661 ± 0.021	1.259 ± 0.029	166.9 ± 0.7	…	…	…
111		2.114 ± 0.064	1.722 ± 0.047	78.2 ± 1.8	1.708 ± 0.081	0.315 ± 0.931	78.0 ± 9.0

Table B.2. continued.

ID	Region	Observed source size			Deconvolved diameter		
		Major axis (″)	Minor axis (″)	PA (°)	Major axis (″)	Minor axis (″)	PA (°)
112		2.571 ± 0.064	2.361 ± 0.081	147.2 ± 4.0	2.070 ± 0.110	1.860 ± 0.120	103.0 ± 9.0
113		1.957 ± 0.051	1.511 ± 0.066	150.4 ± 1.8	1.120 ± 0.110	0.650 ± 0.220	121.0 ± 9.0
114		1.821 ± 0.022	1.314 ± 0.030	167.3 ± 0.7	0.670 ± 0.064	0.414 ± 0.114	170.0 ± 9.0
115		1.976 ± 0.051	1.584 ± 0.068	155.8 ± 2.0	1.120 ± 0.120	0.860 ± 0.160	121.0 ± 9.0
116		1.861 ± 0.079	1.673 ± 0.072	112.4 ± 4.5	1.321 ± 0.079	0.307 ± 0.072	87.9 ± 4.5
117	G24.60+0.1M1	1.681 ± 0.041	1.456 ± 0.056	168.5 ± 3.9	0.800 ± 0.873	0.170 ± 1.500	82.0 ± 9.0
118		2.304 ± 0.086	2.068 ± 0.067	60.9 ± 6.6	1.940 ± 0.110	1.240 ± 0.130	71.6 ± 6.6
119		3.087 ± 0.074	2.396 ± 0.081	132.6 ± 2.5	2.708 ± 0.096	1.914 ± 0.118	122.5 ± 5.1
120		2.232 ± 0.048	1.467 ± 0.052	20.8 ± 1.5	1.636 ± 0.076	0.426 ± 0.791	35.0 ± 9.0
121		5.480 ± 0.200	2.210 ± 0.110	34.4 ± 1.5	5.280 ± 0.210	1.650 ± 0.160	35.9 ± 1.7
122		6.720 ± 0.150	3.290 ± 0.150	38.5 ± 1.3	6.570 ± 0.160	2.930 ± 0.170	39.6 ± 1.4
123		1.856 ± 0.013	1.205 ± 0.018	163.1 ± 0.5	…	…	…
124		1.902 ± 0.066	1.788 ± 0.073	25.0 ± 9.0	1.380 ± 0.130	0.800 ± 0.250	71.0 ± 9.0
125		1.594 ± 0.041	1.122 ± 0.056	168.9 ± 2.3	…	…	…
126		1.708 ± 0.042	1.097 ± 0.044	162.8 ± 1.8	…	…	…
127		2.910 ± 0.120	2.530 ± 0.130	132.0 ± 7.6	2.530 ± 0.170	2.050 ± 0.200	114.0 ± 9.0
128		4.754 ± 0.072	2.358 ± 0.042	5.9 ± 0.6	4.462 ± 0.078	1.992 ± 0.052	7.2 ± 0.8
129		2.374 ± 0.071	1.524 ± 0.096	176.8 ± 2.1	1.690 ± 0.110	0.900 ± 0.190	1.1 ± 5.6
130		1.908 ± 0.037	1.501 ± 0.047	151.2 ± 3.0	1.115 ± 0.097	0.612 ± 0.201	118.0 ± 9.0
131		2.076 ± 0.077	1.161 ± 0.061	165.9 ± 2.1	…	…	…
132	G24.60+0.01M2	2.003 ± 0.081	1.537 ± 0.046	137.2 ± 3.8	1.400 ± 0.130	0.790 ± 0.220	103.0 ± 9.0
133		2.778 ± 0.097	2.206 ± 0.101	0.1 ± 5.5	2.310 ± 0.150	1.860 ± 0.170	17.0 ± 9.0
134		2.080 ± 0.180	1.490 ± 0.140	98.7 ± 6.2	…	…	…
135		1.826 ± 0.074	1.119 ± 0.078	166.0 ± 2.7	0.813 ± 0.843	0.354 ± 0.673	4.7 ± 9.8
137	G34.43+0.2M3	3.890 ± 0.110	2.660 ± 0.110	165.1 ± 1.4	3.580 ± 0.120	2.190 ± 0.130	166.2 ± 1.7
138		1.764 ± 0.020	1.587 ± 0.020	156.0 ± 1.8	0.898 ± 0.045	0.483 ± 0.084	172.0 ± 5.7
139		2.024 ± 0.065	1.596 ± 0.054	143.8 ± 2.5	1.287 ± 0.087	0.594 ± 0.181	149.0 ± 5.0
140		1.553 ± 0.023	1.880 ± 0.061	15.4 ± 8.2	1.390 ± 0.100	1.040 ± 0.120	21.0 ± 8.5
141		3.575 ± 0.098	1.410 ± 0.024	150.5 ± 2.5	…	…	…
142		2.217 ± 0.056	2.918 ± 0.098	74.9 ± 4.1	3.240 ± 0.110	2.490 ± 0.120	72.7 ± 4.9
143	IRAS 19095+0930	2.014 ± 0.039	1.445 ± 0.044	115.5 ± 0.8	1.250 ± 0.350	0.340 ± 1.030	124.0 ± 9.0
144		3.158 ± 0.079	2.577 ± 0.091	87.0 ± 1.6	2.724 ± 0.090	2.177 ± 0.111	84.3 ± 3.7
145		1.601 ± 0.011	1.370 ± 0.013	94.7 ± 0.6	…	…	…
146		1.715 ± 0.018	1.365 ± 0.021	105.1 ± 0.6	…	…	…
Observed and deconvolved source sizes for *K* band detections							
48a	IRAS 18228−1312	2.950 ± 0.390	2.090 ± 0.220	166.0 ± 9.0	…	…	…
48b		3.070 ± 0.640	2.330 ± 0.410	79.0 ± 9.0	3.060 ± 0.210	2.310 ± 0.160	169.0 ± 9.0
48c		7.619 ± 0.716	1.042 ± 0.085	81.9 ± 0.9	2.300 ± 1.000	1.400 ± 1.000	119.0 ± 9.0
62	G19.27+0.1M1	0.485 ± 0.019	0.393 ± 0.021	134.6 ± 7.2	…	…	…
63	IRAS 18236−1205	1.670 ± 0.024	0.970 ± 0.011	133.5 ± 7.9	1.510 ± 0.028	0.690 ± 0.017	132.5 ± 9.4
64		0.868 ± 0.036	0.738 ± 0.026	121.0 ± 8.9	0.499 ± 0.079	0.240 ± 0.168	109.0 ± 9.0
65		0.799 ± 0.016	0.713 ± 0.013	109.9 ± 6.5	0.394 ± 0.040	0.035 ± 0.136	93.2 ± 9.2
73	G23.60+0.0M1	0.598 ± 0.087	0.365 ± 0.035	54.1 ± 7.5	…	…	…
74		1.022 ± 0.279	0.397 ± 0.061	18.9 ± 5.7	0.878 ± 0.356	0.226 ± 0.111	15.0 ± 9.0
83	IRAS 18316−0602	1.069 ± 0.105	0.611 ± 0.048	178.4 ± 5.4	0.969 ± 0.126	0.451 ± 0.096	171.2 ± 9.2
94		0.946 ± 0.284	0.682 ± 0.180	57.0 ± 9.0	0.809 ± 0.374	0.576 ± 0.511	70.0 ± 9.0
95		0.455 ± 0.081	0.388 ± 0.059	16.0 ± 9.0	…	…	…
96	G24.08+0.0M2	0.503 ± 0.021	0.407 ± 0.023	27.4 ± 7.8	…	…	…
110	G24.33+0.1M1	0.528 ± 0.018	0.350 ± 0.020	33.4 ± 3.3	…	…	…
136	G24.60+0.01M2	0.685 ± 0.068	0.492 ± 0.068	78.0 ± 9.0	…	…	…
137	G34.43+0.2M3	1.025 ± 0.060	0.797 ± 0.070	61.0 ± 9.0	0.899 ± 0.085	0.715 ± 0.108	123.8 ± 3.9
143	IRAS 19095+0930	0.572 ± 0.012	0.371 ± 0.012	50.0 ± 1.9	0.269 ± 0.034	0.181 ± 0.058	94.0 ± 9.0

Table B.3. Intensities, fluxes and source sizes for the sources detected at both frequency bands and imaged using the common *uv* range (see Sect. 3.2).

				Convolved image size			Deconvolved image size				
ID	Region	Intensity [a] (mJy beam^{-1})	Flux [a] (mJy)	Major axis ($''$)	Minor axis ($''$)	PA (deg)	Major axis ($''$)	Minor axis ($''$)	PA (deg)	$\theta_{\rm beam}$, PA ($''\times''$, $^\circ$)	rms (mJy)
Intensities, fluxes and sizes from the *C* band images with common *uv* range											
48a	IRAS 18228−1312	11.50 ± 0.61	55.32 ± 3.50	4.60 ± 0.28	2.08 ± 0.10	0 ± 2	4.24 ± 0.31	1.72 ± 0.13	2 ± 3	1.88 ± 1.66, −14	0.400
48b		8.76 ± 0.99	75.41 ± 9.50	4.35 ± 0.50	3.93 ± 0.44	40 ± 44	4.15 ± 0.72	3.56 ± 0.65	52 ± 54	1.88 ± 1.66, −14	0.400
48c		32.31 ± 1.70	129.52 ± 8.30	3.21 ± 0.18	2.48 ± 0.12	61 ± 8	3.00 ± 0.21	1.73 ± 0.21	66 ± 8	1.88 ± 1.66, −14	0.400
63	IRAS 18236−1205	0.56 ± 0.02	0.99 ± 0.06	2.24 ± 0.11	1.66 ± 0.07	162 ± 5	1.26 ± 0.17	1.13 ± 0.28	71 ± 63	1.99 ± 1.11, −18	0.021
64		0.30 ± 0.01	0.28 ± 0.02	1.97 ± 0.09	0.97 ± 0.02	168 ± 1	…	…	…	1.94 ± 1.08, −18	0.005
65		0.56 ± 0.07	0.57 ± 0.14	1.99 ± 0.04	1.07 ± 0.01	163 ± 1	…	…	…	1.94 ± 1.08, −18	0.004
73	G23.60+0.0M1	0.22 ± 0.08	0.24 ± 0.15	1.82 ± 0.09	1.14 ± 0.03	159 ± 2	0.48 ± 0.28	0.30 ± 0.16	13 ± 41	1.77 ± 1.08, −23	0.008
74		0.29 ± 0.01	0.35 ± 0.03	1.94 ± 0.11	1.27 ± 0.05	163 ± 4	0.73 ± 0.28	0.38 ± 0.29	25 ± 40	1.85 ± 1.13, −22	0.008
83	IRAS 18316−0602	2.21 ± 0.09	3.35 ± 0.21	1.94 ± 0.09	1.36 ± 0.05	173 ± 4	1.16 ± 0.18	0.65 ± 0.29	21 ± 16	1.64 ± 1.05, −22	0.011
96	G24.08+0.0M2	18.70 ± 0.30	24.97 ± 0.65	1.95 ± 0.04	1.29 ± 0.02	151 ± 1	0.98 ± 0.09	0.57 ± 0.10	125 ± 10	1.73 ± 1.08, −21	0.624
110	G24.33+0.1M1	0.46 ± 0.12	0.46 ± 0.21	1.55 ± 0.05	1.24 ± 0.03	168 ± 4	…	…	…	1.61 ± 1.19, −13	0.009
137	G34.43+0.2M3	3.41 ± 0.23	14.40 ± 1.20	3.36 ± 0.24	2.54 ± 0.17	170 ± 9	3.04 ± 0.28	2.10 ± 0.21	171 ± 10	1.46 ± 1.38, −59	0.242
143	IRAS 19095+0930	30.03 ± 0.74	39.50 ± 1.60	1.88 ± 0.05	1.34 ± 0.03	113 ± 3	1.18 ± 0.01	0.26 ± 0.17	121 ± 5	1.49 ± 1.28, −85	0.107
Intensities, fluxes and sizes from the *K* band images with the common *uv* range											
48a	IRAS 18228−1312	1.51 ± 0.13	15.19 ± 1.51	3.02 ± 0.28	1.62 ± 0.13	1 ± 5	2.93 ± 0.29	1.47 ± 0.15	1 ± 5	2.50 ± 1.25, +57	0.200
48b		1.59 ± 0.17	10.53 ± 1.30	2.09 ± 0.23	1.54 ± 0.16	67 ± 13	1.98 ± 0.25	1.36 ± 0.18	67 ± 13	2.50 ± 1.25, +57	0.200
48c		6.28 ± 0.36	54.41 ± 3.51	2.81 ± 0.17	1.50 ± 0.08	67 ± 3	2.73 ± 0.18	1.31 ± 0.09	68 ± 3	2.50 ± 1.25, +57	0.200
63	IRAS 18236−1205	0.21 ± 0.03	0.75 ± 0.13	1.58 ± 0.23	1.13 ± 0.14	115 ± 15	1.41 ± 0.28	0.88 ± 0.21	113 ± 23	0.51 ± 0.32, −26	0.002
64		0.17 ± 0.03	0.35 ± 0.08	1.24 ± 0.24	0.81 ± 0.12	127 ± 13	1.01 ± 0.32	0.43 ± 0.28	125 ± 27	0.73 ± 0.67, −25	0.004
65		2.03 ± 0.05	2.31 ± 0.09	0.81 ± 0.02	0.70 ± 0.02	110 ± 6	…	…	…	0.73 ± 0.67, −25	0.002
73	G23.60+0.0M1	0.44 ± 0.05	0.43 ± 0.09	0.89 ± 0.12	0.61 ± 0.06	74 ± 10	…	…	…	0.76 ± 0.71, −1	0.001
74		0.20 ± 0.04	0.49 ± 0.13	1.01 ± 0.27	0.39 ± 0.06	18 ± 5	0.86 ± 0.34	0.21 ± 0.11	15 ± 17	0.54 ± 0.30, +32	0.002
83	IRAS 18316−0602	1.55 ± 0.09	3.73 ± 0.29	1.34 ± 0.08	0.96 ± 0.05	3 ± 6	1.11 ± 0.10	0.65 ± 0.08	3 ± 7	0.91 ± 0.84, −47	1.924
96	G24.08+0.0M2	4.75 ± 0.32	8.26 ± 0.83	1.18 ± 0.09	0.78 ± 0.05	128 ± 6	0.94 ± 0.12	0.24 ± 0.13	125 ± 7	0.73 ± 0.70, +6	0.008
110	G24.33+0.1M1	0.97 ± 0.31	1.20 ± 0.06	0.93 ± 0.03	0.85 ± 0.03	146 ± 13	0.45 ± 0.11	0.30 ± 0.18	1 ± 37	0.85 ± 0.75, −56	0.002
137	G34.43+0.2M3	0.53 ± 0.04	2.21 ± 0.20	2.33 ± 0.19	1.50 ± 0.10	179 ± 6	1.19 ± 0.14	2.14 ± 0.21	180 ± 7	0.95 ± 0.88, −41	0.043
143	IRAS 19095+0930	117.66 ± 1.40	130.87 ± 2.60	0.94 ± 0.01	0.90 ± 0.01	117 ± 10	0.34 ± 0.05	0.23 ± 0.09	66 ± 29	0.91 ± 0.84, −47	1.924

Notes. [a]The intensities and fluxes are corrected for the primary beam response of the antennas, except for source 137, which is located outside the primary beam of the antennas and no correction factor can be determined.

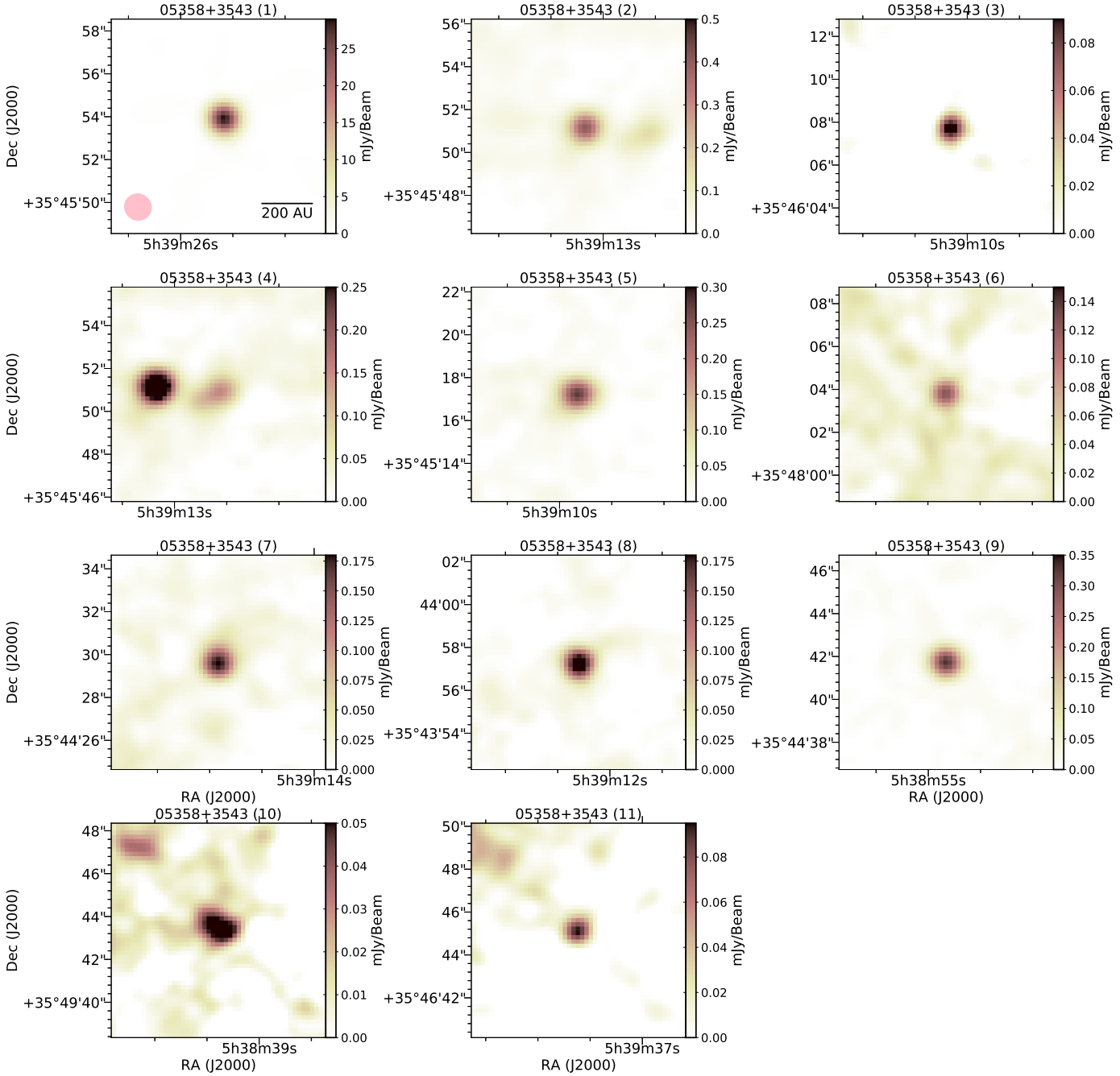

Fig. B.1. Close-up views of the *C*- (color-scale image) and *K*-band (contours) continuum images for the sources listed in Table B.1. Maps for the sources detected in region IRAS 05358+3543.

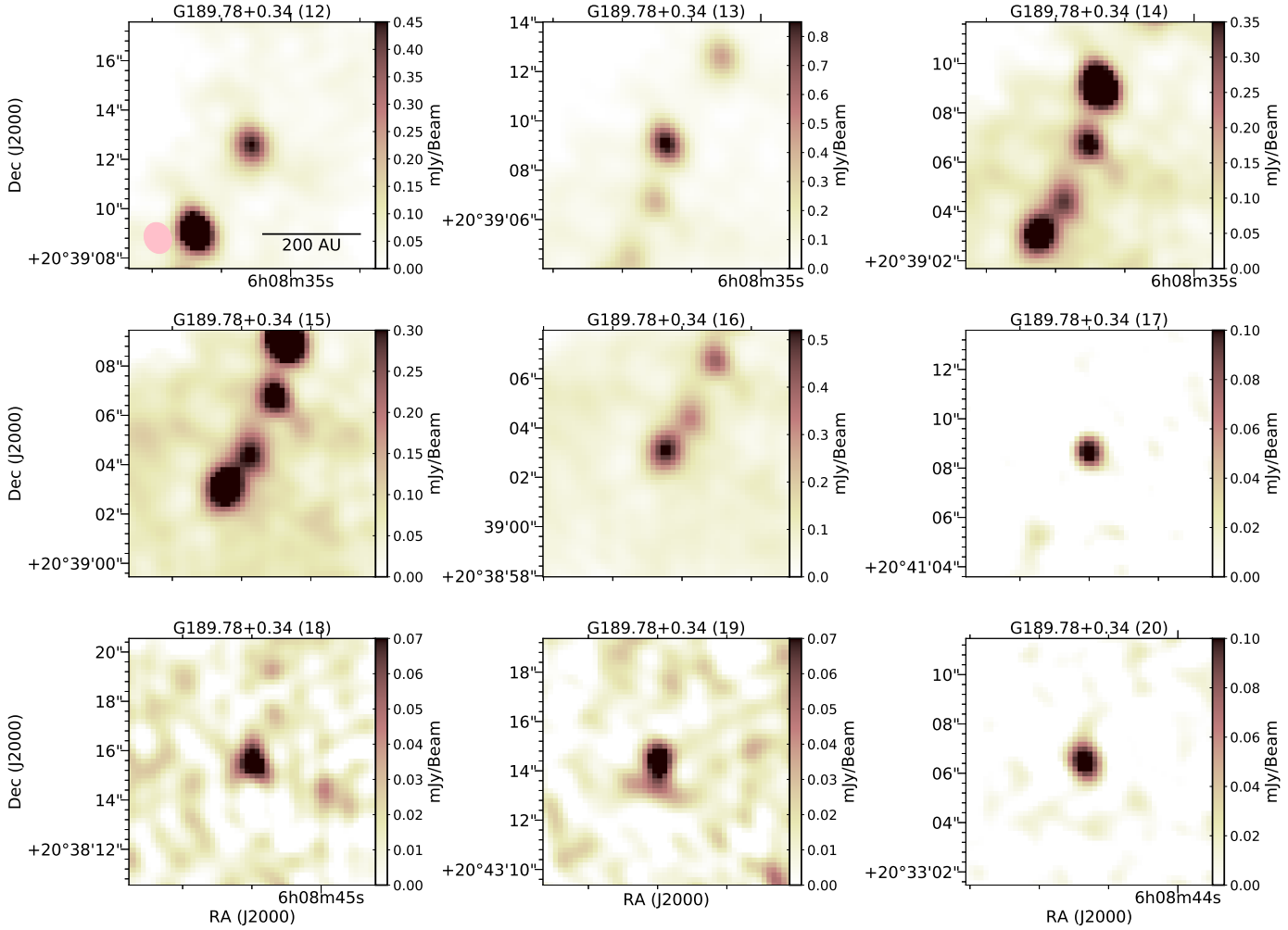

Fig. B.2. Close-up views of the *C*- (color-scale image) and *K*-band (contours) continuum images for the sources listed in Table B.1. Maps for the sources detected in region G189.78+0.34.

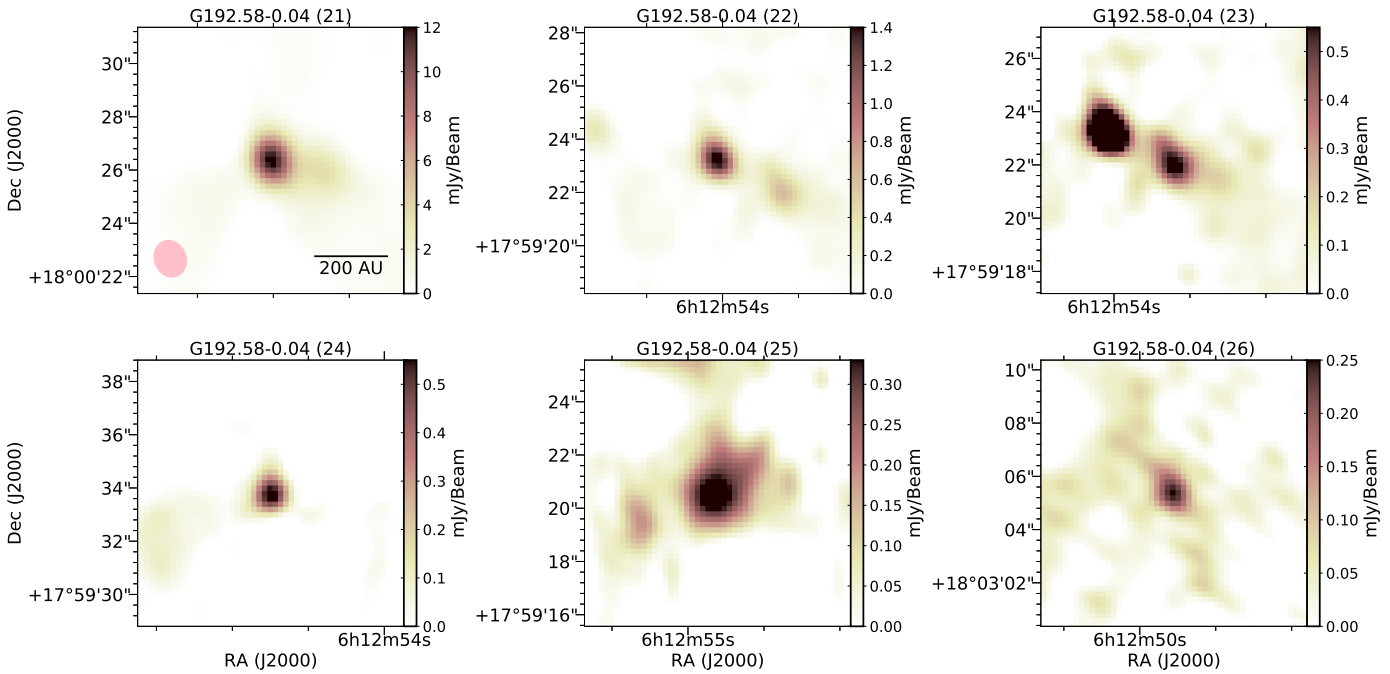

Fig. B.3. Close-up views of the *C*- (color-scale image) and *K*-band (contours) continuum images for the sources listed in Table B.1. Maps for the sources detected in region G192.58−0.04.

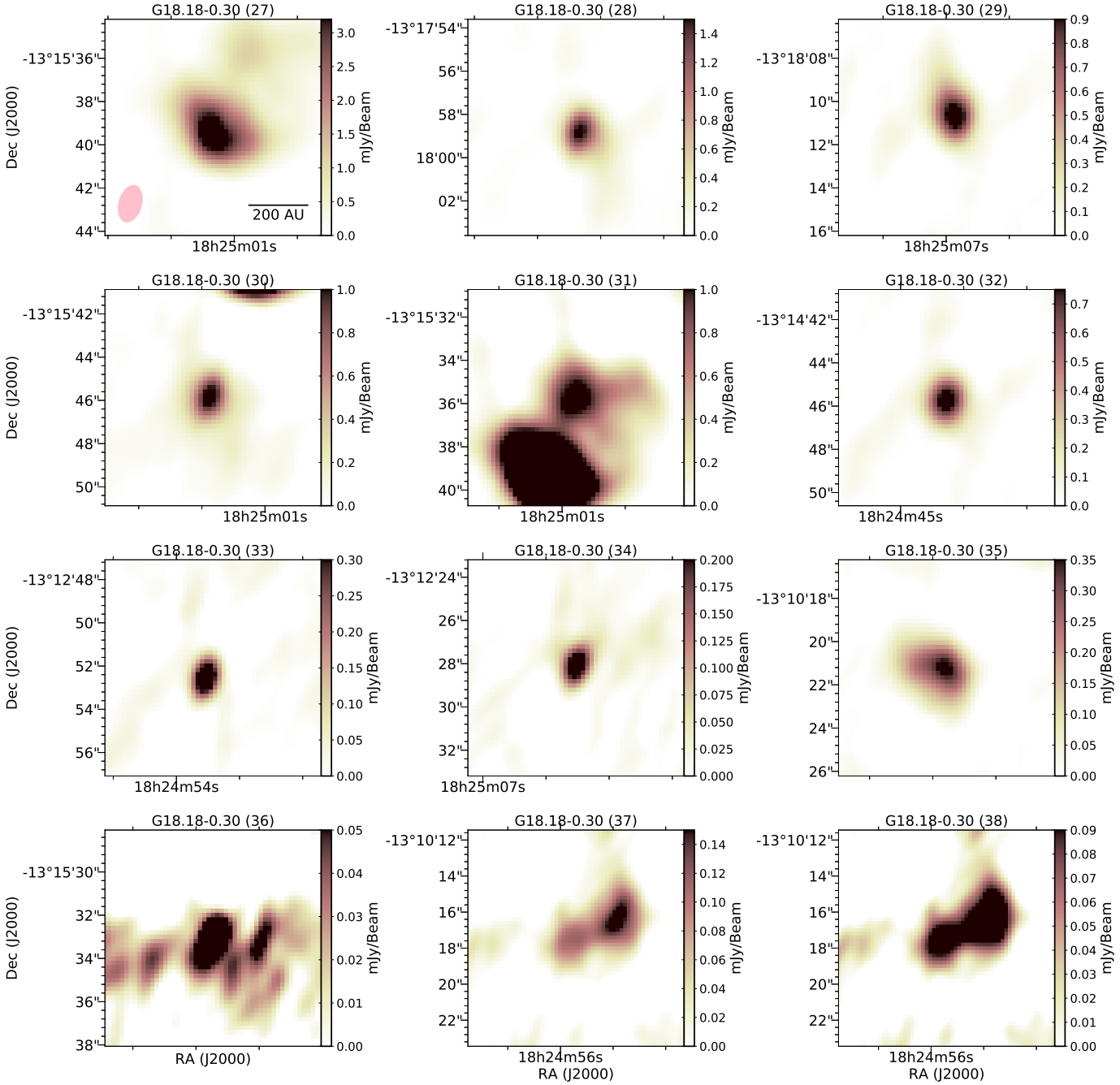

Fig. B.4. Close-up views of the *C*- (color-scale image) and *K*-band (contours) continuum images for the sources listed in Table B.1. Maps for the sources detected in region G18.18−0.30.

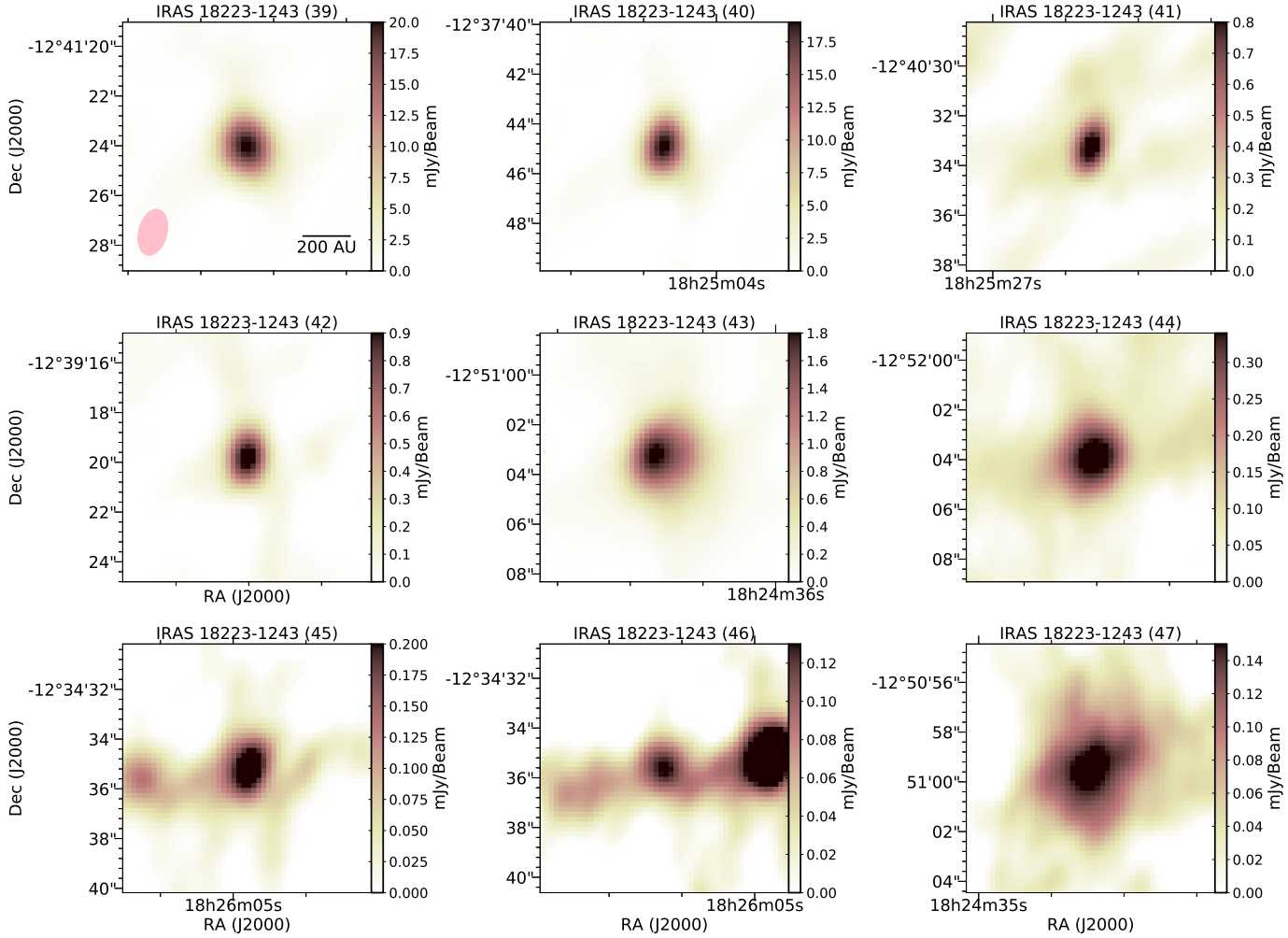

Fig. B.5. Close-up views of the *C*- (color-scale image) and *K*-band (contours) continuum images for the sources listed in Table B.1. Maps for the sources detected in region IRAS 18223−1243.

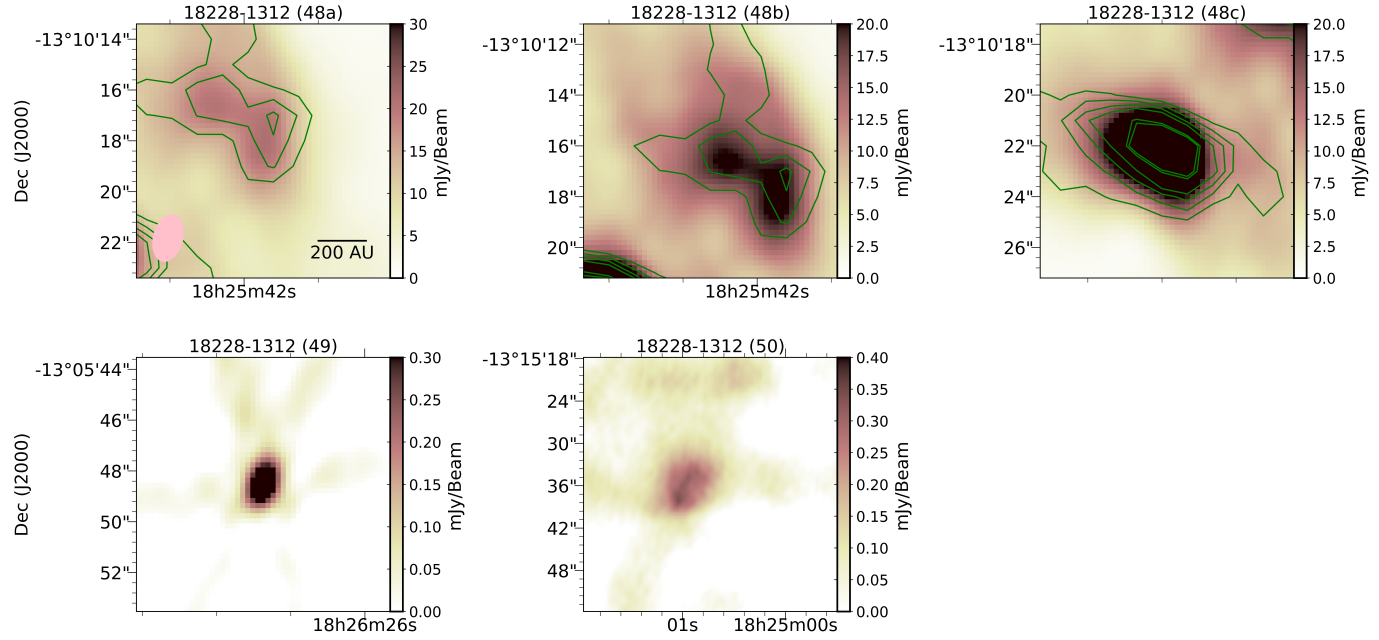

Fig. B.6. Close-up views of the *C*- (color-scale image) and *K*-band (contours) continuum images for the sources listed in Table B.1. Maps for the sources detected in region IRAS 18228−1312.

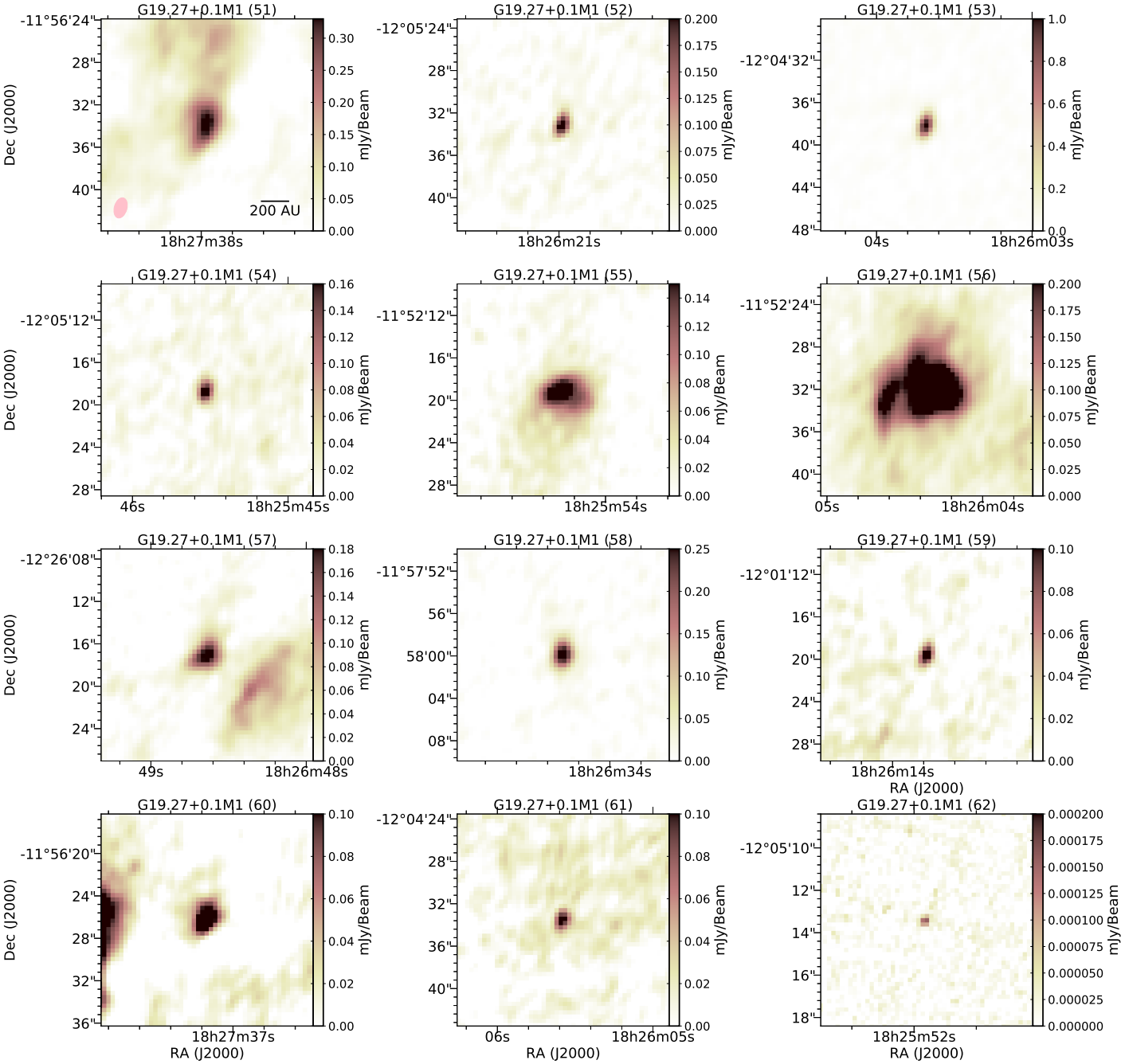

Fig. B.7. Close-up views of the *C*- (color-scale image) and *K*-band (contours) continuum images for the sources listed in Table B.1. Maps for the sources detected in region G19.27+0.1 M1.

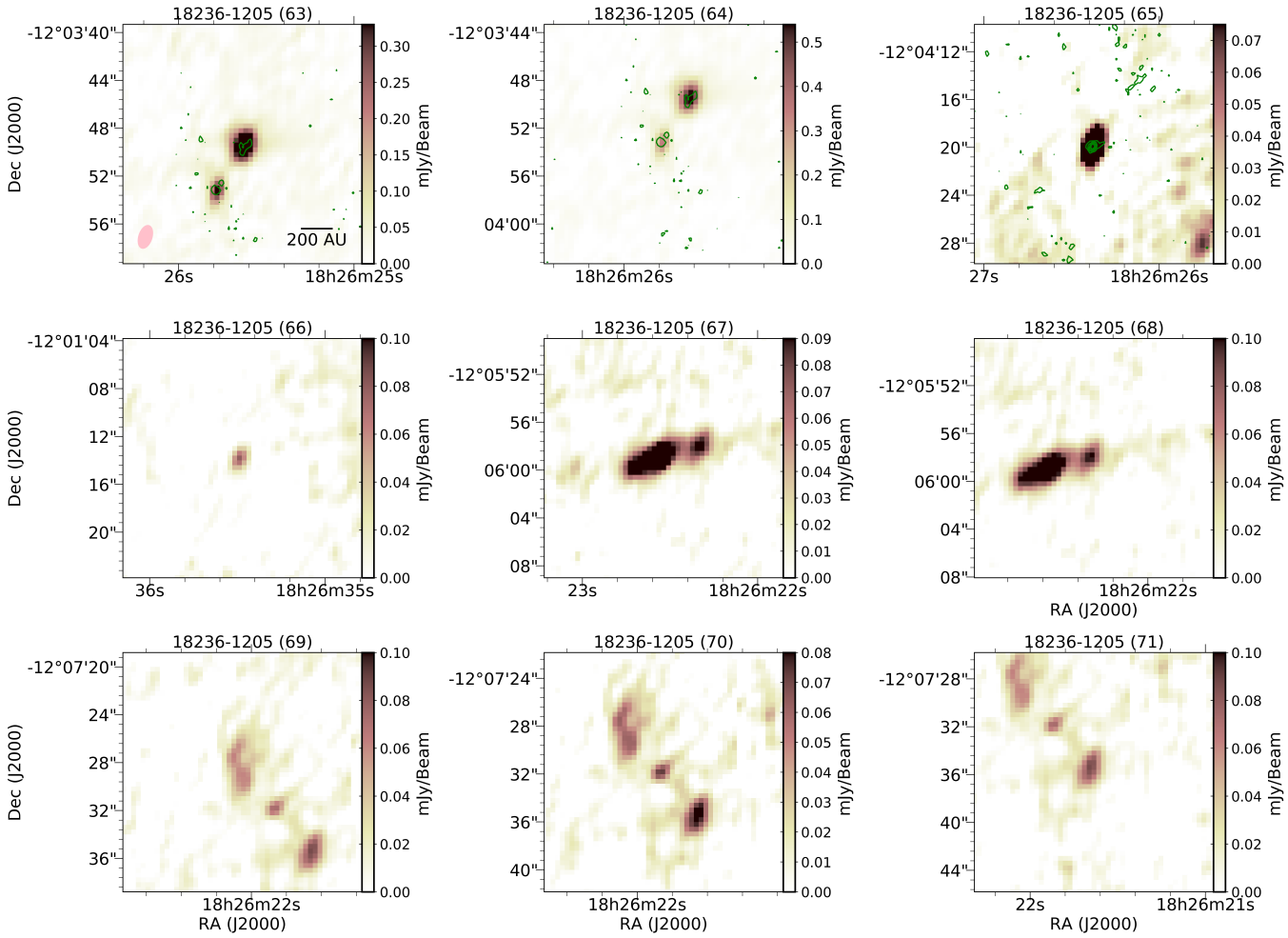

Fig. B.8. Close-up views of the *C*- (color-scale image) and *K*-band (contours) continuum images for the sources listed in Table B.1. Maps for the sources detected in region IRAS 18236−1205.

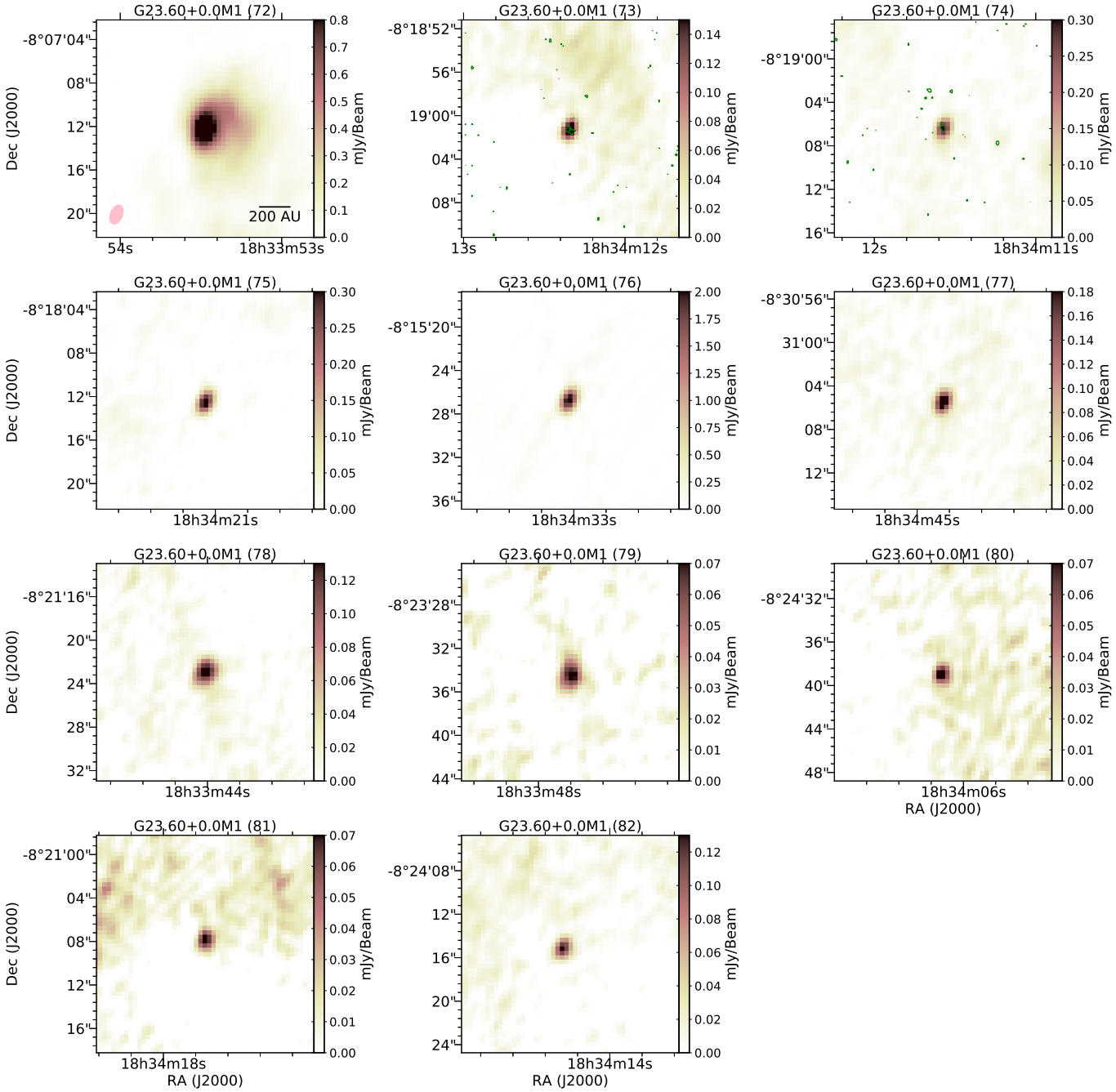

Fig. B.9. Close-up views of the *C*- (color-scale image) and *K*-band (contours) continuum images for the sources listed in Table B.1. Maps for the sources detected in region G23.60+0.0 M1.

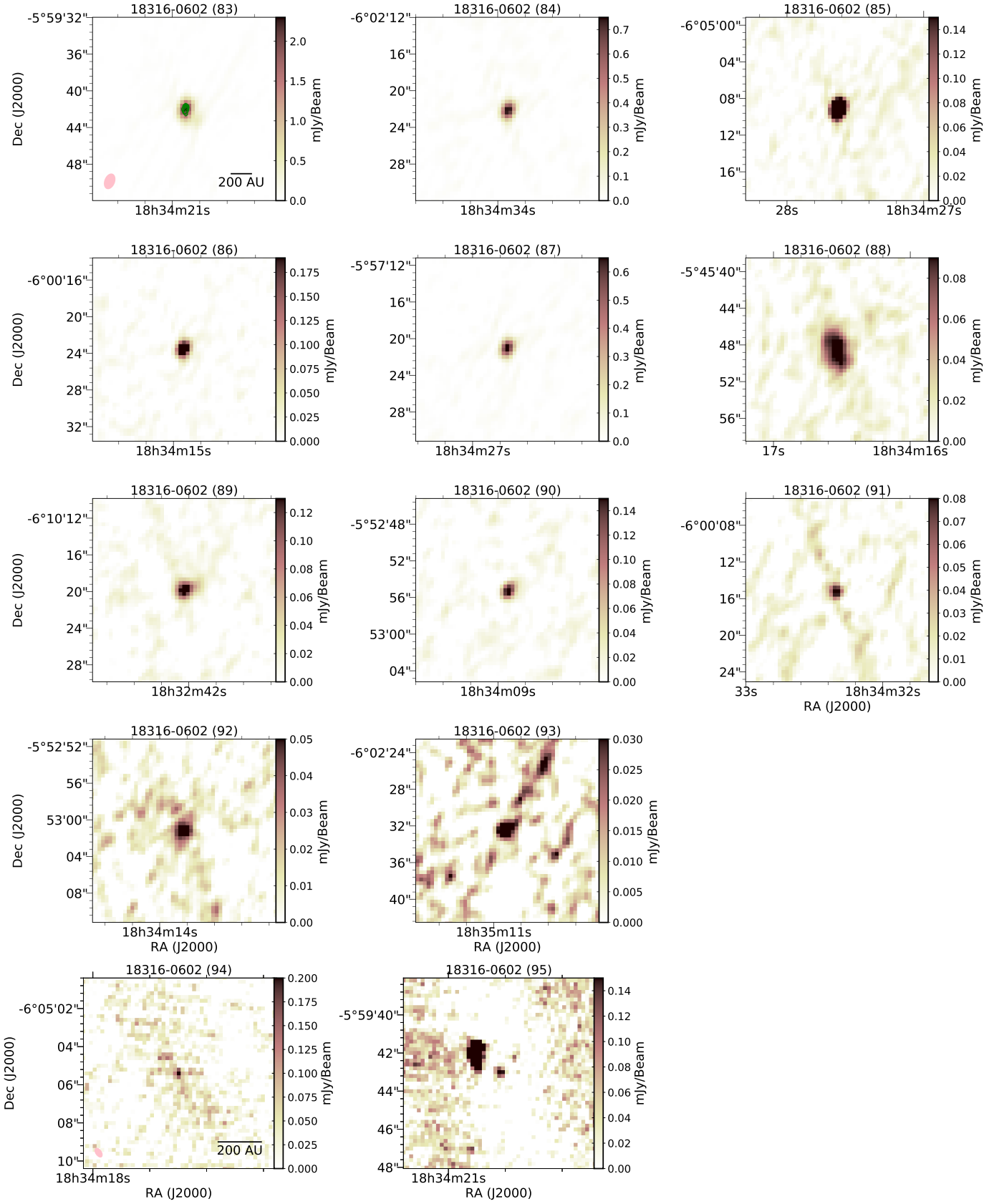

Fig. B.10. Close-up views of the *C*- (color-scale image) and *K*-band (contours) continuum images for the sources listed in Table B.1. The images of sources 94 and 95 correspond to the *K*-band maps. Maps for the sources detected in region IRAS 18316−0602.

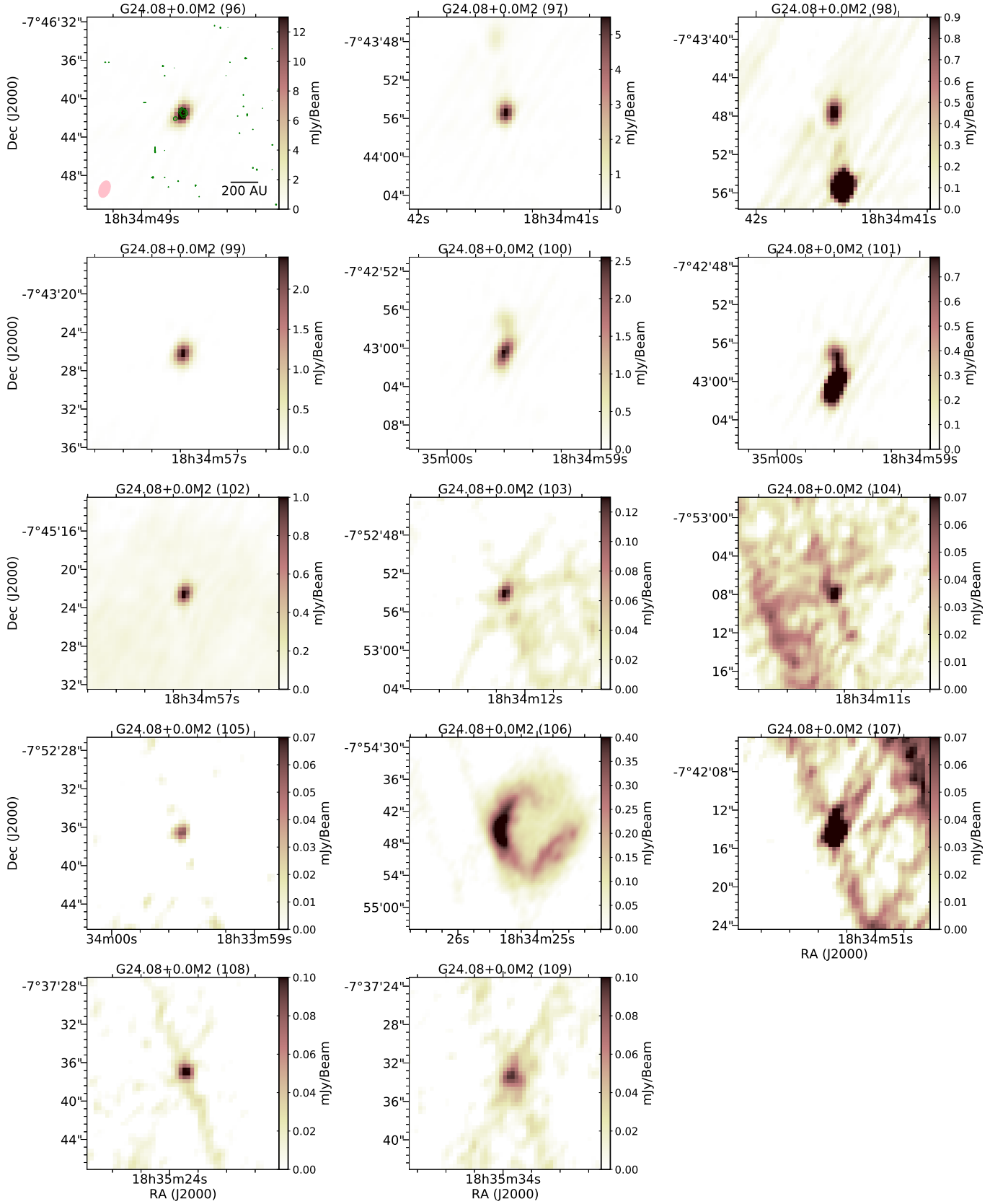

Fig. B.11. Close-up views of the *C*- (color-scale image) and *K*-band (contours) continuum images for the sources listed in Table B.1. Maps for the sources detected in region G24.08+0.0 M2.

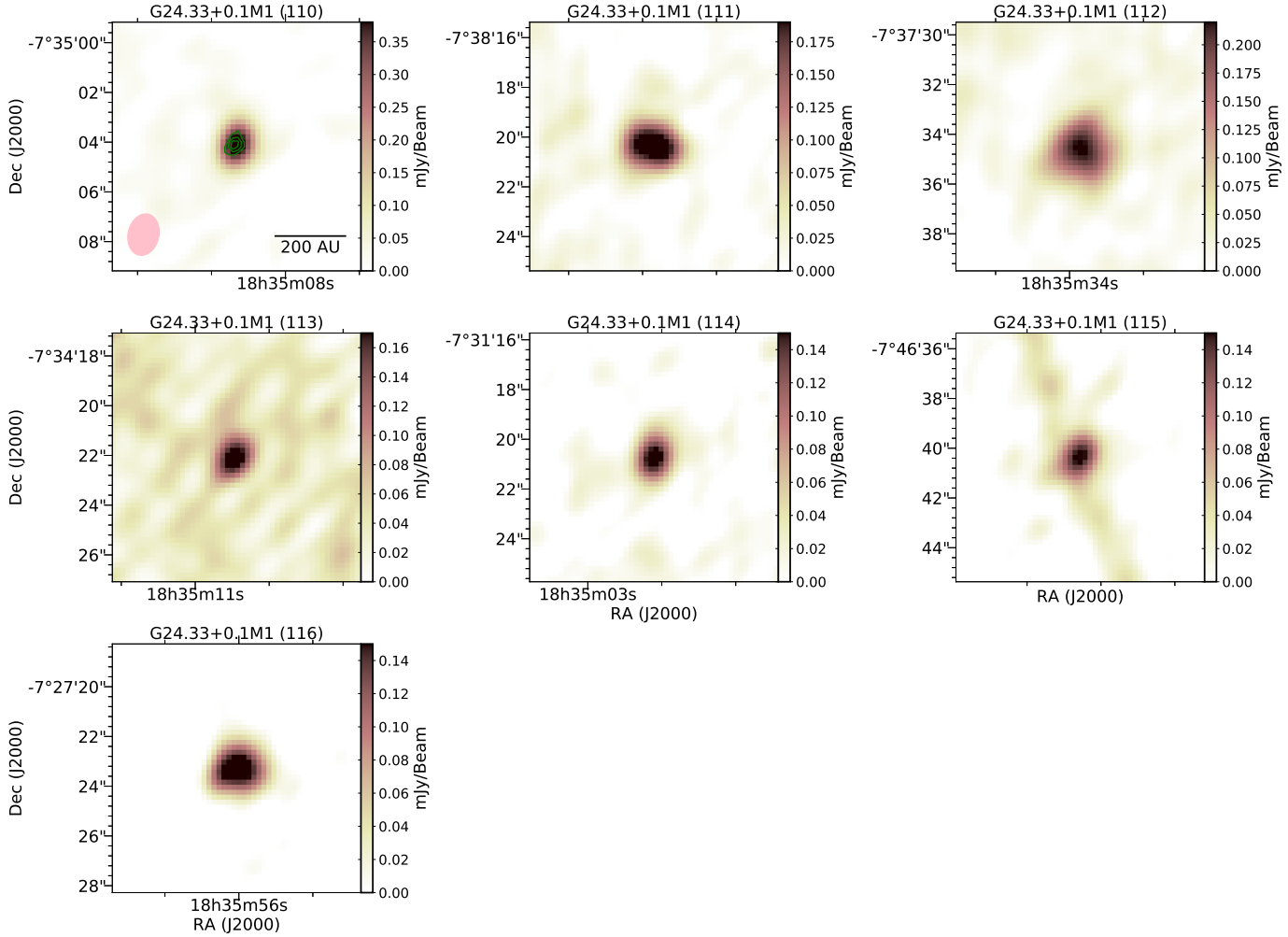

Fig. B.12. Close-up views of the *C*- (color-scale image) and *K*-band (contours) continuum images for the sources listed in Table B.1. Maps for the sources detected in region G24.33+0.1 M1.

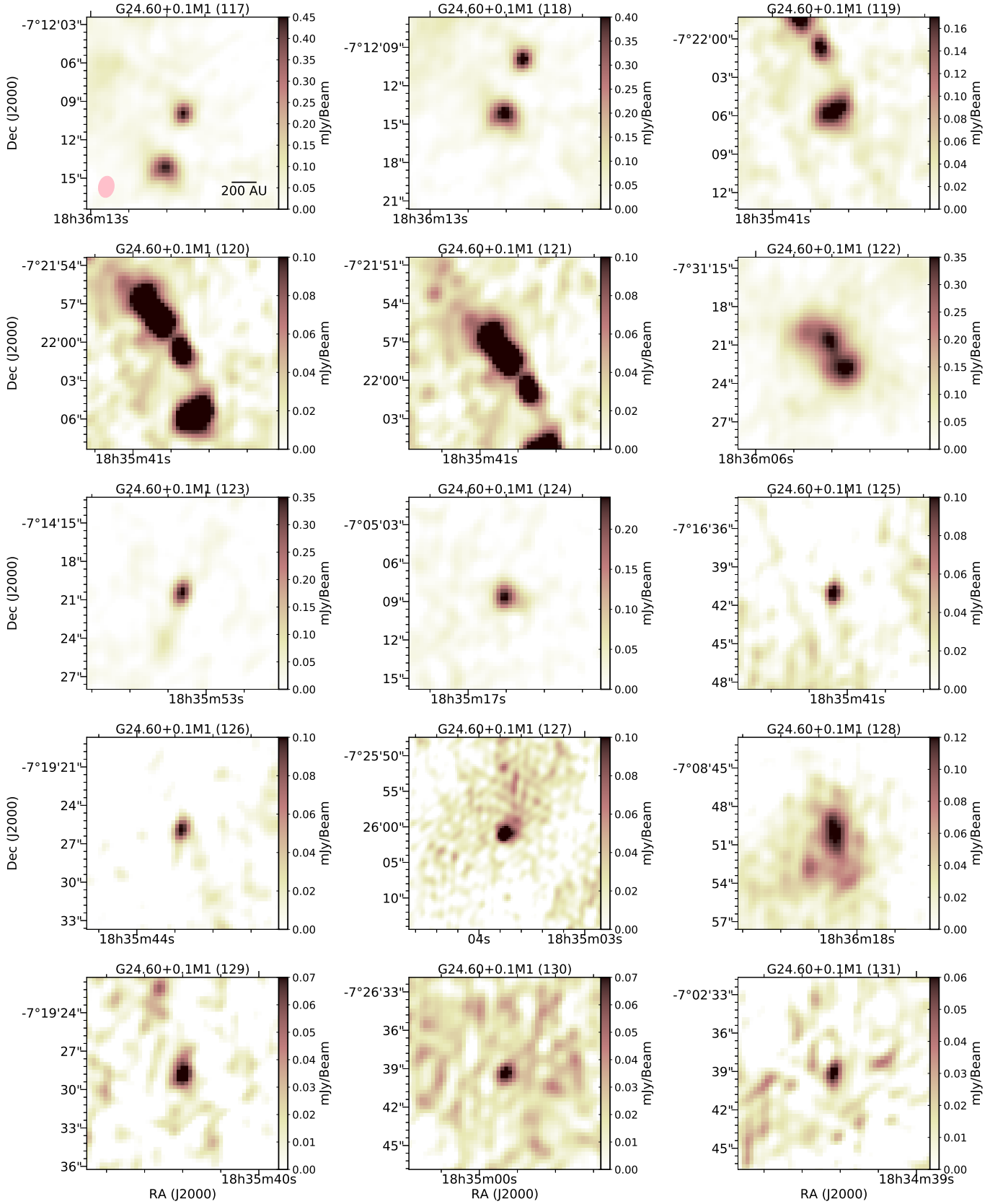

Fig. B.13. Close-up views of the *C*- (color-scale image) and *K*-band (contours) continuum images for the sources listed in Table B.1. Maps for the sources detected in region G24.60+0.1 M1.

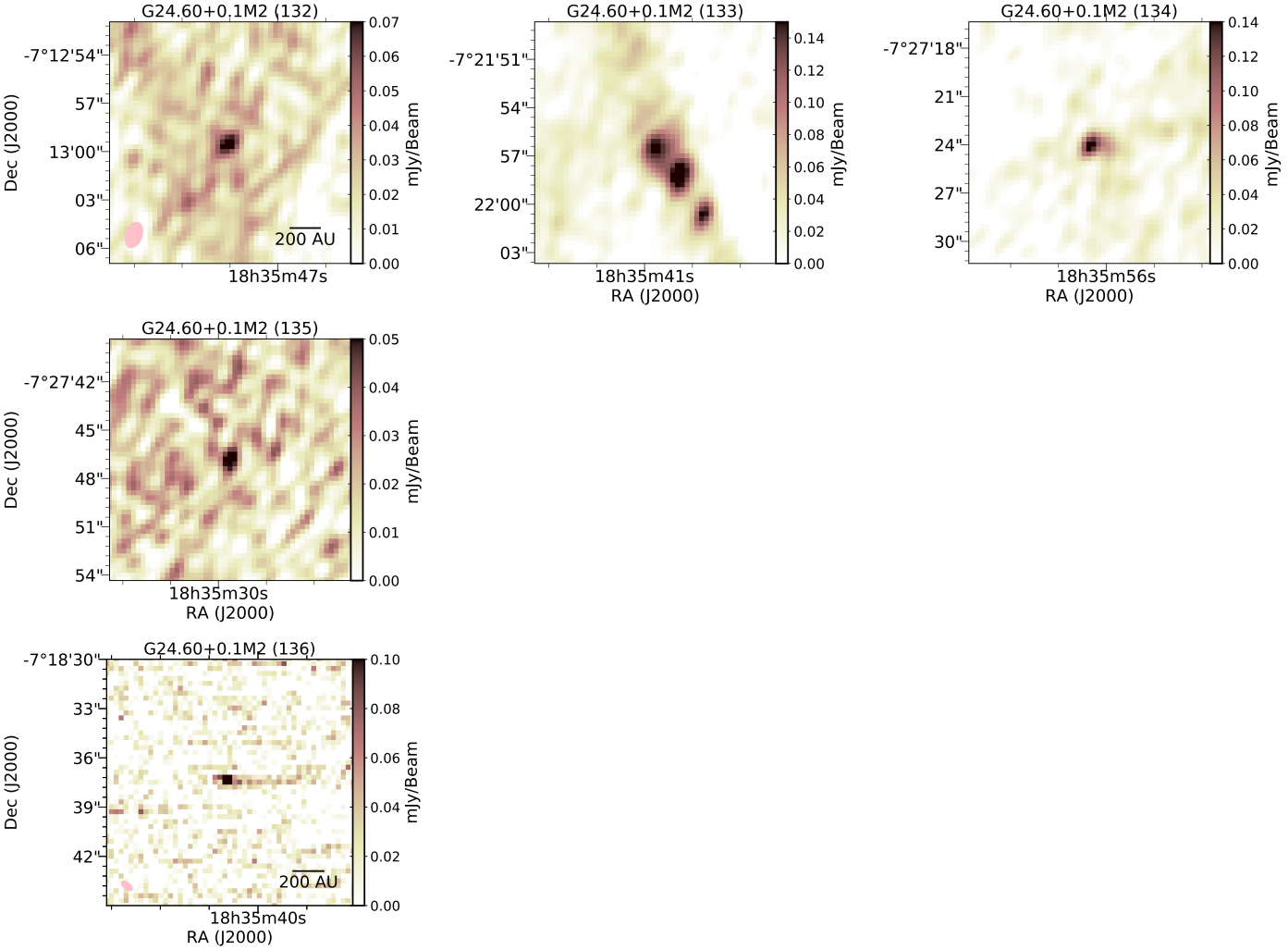

Fig. B.14. Close-up views of the *C*- (color-scale image) and *K*-band (contours) continuum images for the sources listed in Table B.1. The image of source 136 corresponds to the *K*-band map. Maps for the sources detected in region G24.60+0.1 M2.

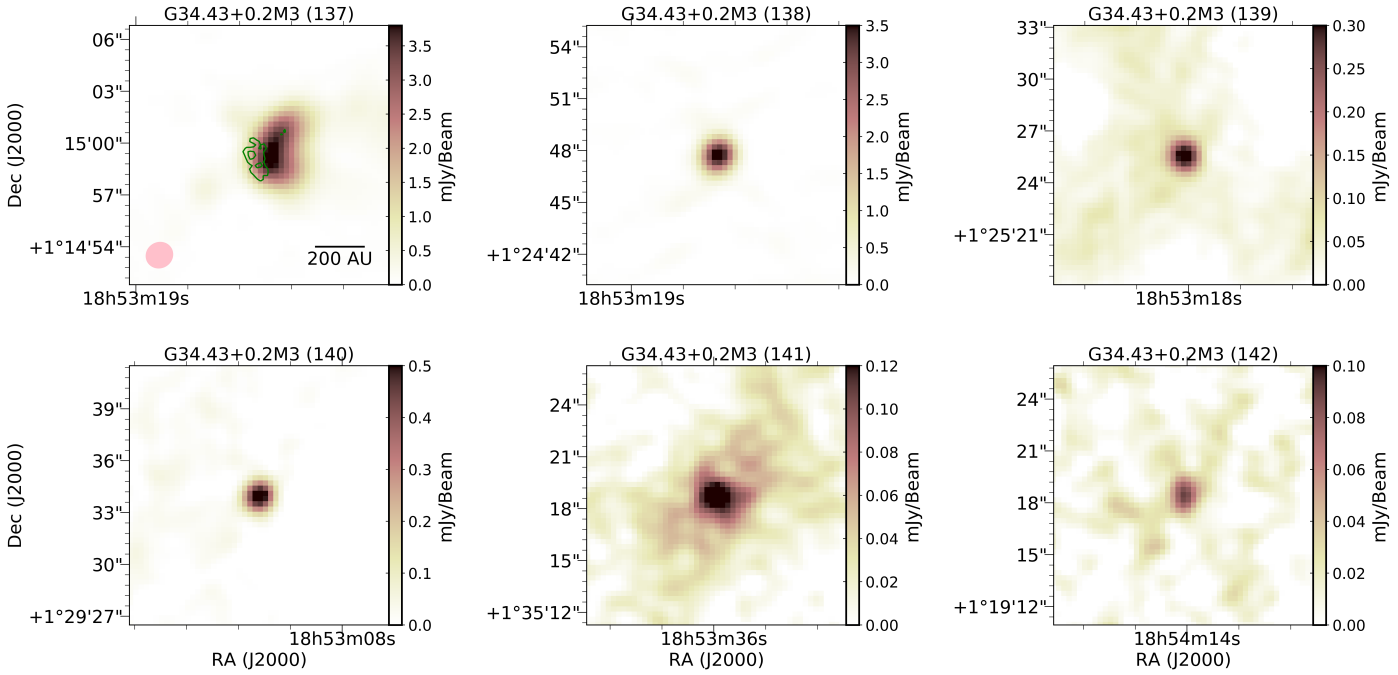

Fig. B.15. Close-up views of the *C*- (color-scale image) and *K*-band (contours) continuum images for the sources listed in Table B.1. Maps for the sources detected in region G34.43+0.2 M3.

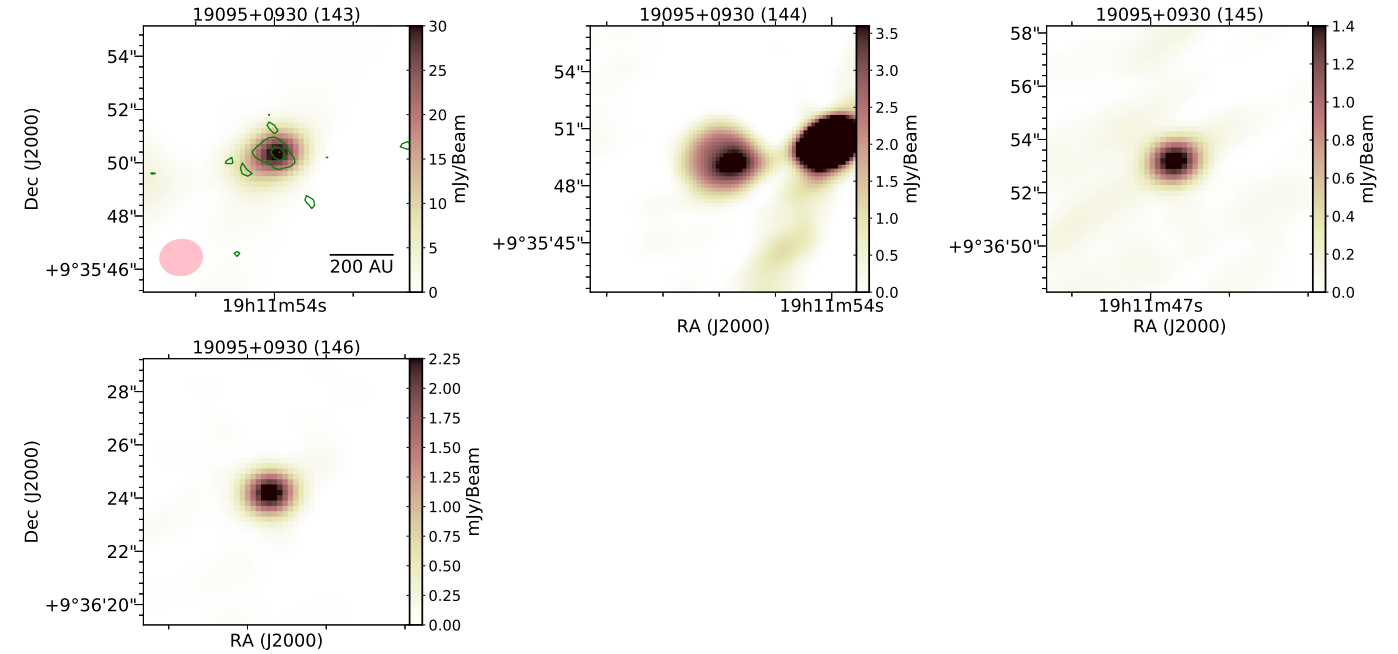

Fig. B.16. Close-up views of the *C*- (color-scale image) and *K*-band (contours) continuum images for the sources listed in Table B.1. Maps for the sources detected in region IRAS 19095+0930.